Frustrated magnetism in the extended kagome lattice

Zhiming Darren TAN



Wolfson College
University of Oxford

A thesis submitted for the degree of
Doctor of Philosophy in Theoretical Physics

Trinity Term 2014

Abstract

The extended kagome lattice, composed of alternating kagome and triangular layers, provides a novel geometry for frustrated magnetism. In this thesis, we study the properties of Heisenberg spins with nearest-neighbour antiferromagnetic interactions on this lattice. In common with many other models of frustrated magnets, this system has highly degenerate classical ground states. It is set apart from other examples, however, by the strong interlayer correlations between triangular layer spins. We study the implications of such correlations in both the statics and dynamics.

We characterise classical ground states using a flux picture for a single layer of kagome spins, a theoretical description that sets geometrical bounds on correlations. We quantify the divergent but sub-extensive ground state degeneracy by a Maxwellian counting argument, and verify this calculation by analysing the energy eigenvalues of numerical ground states. We explore the ground state connectedness but do not reach firm conclusions on this issue. We use the self-consistent Gaussian approximation (SCGA) to calculate static spin correlations at finite temperature. The results of these calculations agree well with elastic neutron scattering experiments. We derive an expression for the effective interlayer interaction between kagome spins by integrating out the triangular lattice spins.

We use linear spinwave theory to compute the spin excitation spectrum numerically. This shows encouraging similarity with inelastic neutron scattering data on a single-crystal $YBaCo_4O_7$ sample, for a wide range of wavevector and frequency. This agreement shows that our spin model is a reasonable description of the physics, and suggests that this numerical technique might be useful for other geometrically frustrated magnets.

We study the dynamics analytically using the stochastic SCGA recently developed for the pyrochlore lattice. For technical reasons, we apply this technique on a related model, the stacked kagome lattice, rather than on the extended kagome lattice itself. From this we find slow relaxation at low temperature, with a rate $\Gamma \sim T^2$, compared to the faster $\Gamma \sim T$ scaling for the pyrochlore. Strikingly, in simulations of the dynamics on the extended kagome lattice by numerical integration of the semiclassical equations of motion, we find two different relaxation rates. Kagome layer spins relax more quickly than the triangular layer spins, having $\Gamma \sim T$.

to ann-marie,
and all collaborators for a beautiful world

Acknowledgements

It brings me great joy to thank the scientists who have nurtured and challenged me over the three years spent working on this thesis. Foremost amongst them is my advisor John Chalker, whose genius as a mentor and guide is matched only by his brilliance as a physicist (though he is likely to gently suggest that brilliance and genius are incomparable). The prospect of leaving Oxford is made bearable by the thought that graduation does not mark the end of my journey with him.

I am grateful also to Toby Perring and Robert Bewley, whose experimental efforts and close collaboration have made a big part of this work possible. It was a grand privilege for me to be taken by Toby on a tour of the ISIS facility.

I am lucky to have taken graduate courses at Oxford, given by John Cardy, Ramin Golestanian, Ard Louis, Mike Teper and Julia Yeomans — all of whom have enriched my perspective of physics and enlarged my sense of wonder. Summers were excellent learning opportunities as well, thanks to the organisers and lecturers at the intensive summer courses I attended in les Houches and Trieste. George Batrouni, Federico Becca, Matthew Fisher, Thierry Giamarchi, Mike Hermele, Frédéric Mila, Gregoire Misguich, Roderich Moessner, Pierre Pujol and Nicolas Regnault have all made an impact.

It has always been a pleasure discussing physics with Rachel Bennett, Fiona Burnell, Simon Davenport, Eliot Kapit, Adam Nahum, Zohar Ringel, Rahul Roy and Stephanie Thiem, though we usually choose simpler topics at mealtimes. I single out for special mention Bruno Bertini, Gábor Halász, Fenner Harper,[†] Curt von Keyserlingk, Neil Robinson and Thomas Scaffidi, as we have shared offices and more intense discussions at some point in time. Except that with Gábor, the office-sharing part is honorary and we've more than made up for it in terms of discourse intensity.

I wish to also thank Amalia Coldea for making me feel welcome with her tireless efforts to bring experimentalists and theorists together with quantum materials and morning coffee (and biscuits!).

Finally, I want to thank Claudio Castelnovo and Fabian Essler for taking on the task of being my thesis examiners. Their critical examination of the work has strengthened my understanding, and I appreciate the important and challenging questions they raised at the viva.

I acknowledge funding support from the Singapore Ministry of Education for making this work possible. It goes without saying that the support and encouragement from my wife has been essential in all that I do.

[†]I'm proud to say that Fenner and I have always been in the same office the whole time.

Contents

Abstract i

Acknowledgements iii

List of Figures vii

1 Introduction 1
- 1.1 Statistical physics . . . 2
  - 1.1.1 Condensed matter systems . . . 3
  - 1.1.2 Correlations . . . 4
  - 1.1.3 Topological defects . . . 4
- 1.2 Magnetism . . . 6
  - 1.2.1 Magnetic models . . . 6
  - 1.2.2 Susceptibility and mean field theory . . . 7
- 1.3 Geometrically frustrated magnetism . . . 10
  - 1.3.1 Experimental signatures of frustration . . . 11
  - 1.3.2 Order by disorder . . . 12
  - 1.3.3 The kagome and pyrochlore lattices . . . 13
- 1.4 Outline for the thesis . . . 15

2 The extended kagome lattice 17
- 2.1 Materials and experiments . . . 17
  - 2.1.1 Class of compounds . . . 17
  - 2.1.2 Geometry of magnetic sublattice . . . 20
  - 2.1.3 Magnetic susceptibility and phase transitions . . . 21
  - 2.1.4 Charge ordering . . . 23
- 2.2 Theoretical model of Heisenberg spins . . . 24
  - 2.2.1 Single-ion anisotropy . . . 25
  - 2.2.2 Ground state contraints for classical spins . . . 26
  - 2.2.3 Experimental and numerical evidence . . . 29

3 Ground states and order by disorder 33
- 3.1 Classical ground states . . . 34
  - 3.1.1 Flux picture for a kagome layer . . . 34
  - 3.1.2 Ground state dimension . . . 36
  - 3.1.3 Simulations of small spin clusters . . . 39
  - 3.1.4 Stable defects . . . 45
  - 3.1.5 Correlations in numerical ground states . . . 46
- 3.2 Order by disorder . . . 49

4 Statistical mechanics of the classical spin model 51
- 4.1 Self-consistent Gaussian approximation (SCGA) . . . 51
  - 4.1.1 Lattice Fourier transform . . . 53
  - 4.1.2 Band structure . . . 56
  - 4.1.3 Self-consistency conditions . . . 58
  - 4.1.4 Ordering transition . . . 61
  - 4.1.5 Static structure factor . . . 62
- 4.2 Effective interactions between kagome layers . . . 65

5 Spinwave dynamics 67
- 5.1 Linear spinwave theory . . . 68

5.1.1 Bosonic Hamiltonian . . . 68
5.1.2 Classical ground states . . . 69
5.1.3 Equations of motion and normal modes . . . 70
5.1.4 Ground state moments . . . 73
5.1.5 Dynamic structure factor . . . 73
5.1.6 Spin autocorrelation function . . . 75
5.2 Spinwave simulations . . . 77
5.2.1 Simulation details . . . 77
5.2.2 Stability of ground states . . . 78
5.2.3 Distribution of frequency modes . . . 80
5.2.4 Plots of dynamic structure factor . . . 80
5.3 Comparison with experiments . . . 85
5.3.1 Varying σ with $\alpha\sigma$ constant . . . 85
5.3.2 Data from inelastic magnetic neutron scattering . . . 85

6 Stochastic dynamics **93**
6.1 SCGA for stacked kagome layers . . . 93
6.1.1 Lattice description . . . 94
6.1.2 Band structure . . . 96
6.1.3 Self-consistency conditions . . . 97
6.1.4 Low-temperature analytic behaviour . . . 97
6.2 Stochastic SCGA . . . 98
6.2.1 Spin diffusion . . . 99
6.2.2 General solution . . . 101
6.2.3 Noise correlators . . . 101
6.3 Spin autocorrelation function . . . 102

7 Molecular dynamics **105**
7.1 MD simulations . . . 106
7.1.1 Simulation details . . . 106
7.1.2 Precession about the total magnetisation . . . 107
7.1.3 System size effects . . . 108
7.2 Results for spin autocorrelation . . . 111
7.2.1 Comparison with linear spinwave theory . . . 111
7.2.2 Dynamics on long timescales . . . 112

8 Concluding remarks **117**
8.1 Summary of main findings . . . 117
8.2 Directions for future work . . . 119

Bibliography **121**

List of Figures

1.1 Cartoon of point defect combination 5
1.2 Illustration of some experimental signatures of frustration 11
1.3 Mechanism of order by disorder 13
1.4 Kagome and pyrochlore lattices 14

2.1 Magnetic geometry of '114' cobaltites 18
2.2 Magnetic geometry of '114' ferrites 19
2.3 Extended kagome geometry 20
2.4 Reciprocal susceptibility for $YBaCo_4O_{7.0}$ powder sample 22
2.5 Neutron diffraction peak intensities for single-crystal $YBaCo_4O_{7.0}$ 22
2.6 Magnetisation measurements for single-crystal $YBaCo_4O_{7.0}$ 26
2.7 A single bipyramid 27
2.8 Ground states for a bipyramid 28
2.9 Magnetic structure factor from elastic neutron scattering and Monte Carlo . 30
2.10 Static spin correlations from Monte Carlo 30
2.11 Diffuse magnetic neutron scattering from $YBaCo_3FeO_7$ powder sample compared with Monte Carlo 31

3.1 Kagome and honeycomb lattices 35
3.2 The full 8-site unit cell for the extended kagome lattice 40
3.3 Minimum spin cluster energy for $N_C = 2$ 41
3.4 Minimum spin cluster energy for $N_C = 3$ 42
3.5 Perspective drawing of the "buckled rhombus" for $N_C = 4$ 43
3.6 Minimum spin cluster energy for $N_C = 4$ 44
3.7 Triangular lattice of apical spins 45
3.8 Interlayer kagome spin correlations 47
3.9 Scalar chirality for kagome layer spins 48
3.10 Scalar chirality for triangular layer spins 49
3.11 Local soft modes for coplanar spin states in the extended kagome lattice . . 49
3.12 Phase diagram for extended kagome lattice 50

4.1 Plan view of original and simplified unit cells 54
4.2 4-site unit cell for SCGA 55
4.3 Band structure for interaction matrix of the 4-site unit cell 58
4.4 Self-consistent solutions for Lagrange multipliers (λ, Λ) 60
4.5 Transition points in the SCGA 61
4.6 SCGA structure factors 64

5.1 Eigenvalues of energy matrix 79
5.2 Zero temperature quantum fluctuations 80
5.3 Distribution of spin wave mode frequencies 82
5.4 Spin wave structure factors in $(h0l)$ plane with different α 83

5.5 Spin wave structure factors in $(hk\bar{2})$ plane with different α 84
5.6 Spin wave structure factors in $(h0l)$ plane with different σ 86
5.7 Spin wave structure factors in $(hk\bar{2})$ plane with different σ 87
5.8 Structure factor along $(\frac{1}{2},0,l)$, $(\frac{3}{2},0,l)$ and $(h,0,\bar{2})$ with different σ 88
5.9 Structure factor in $(h0l)$ plane from experiments 90
5.10 Structure factor in $(hk\bar{2})$ plane from experiments 91
5.11 Structure factor along $(\frac{1}{2},0,l)$, $(\frac{3}{2},0,l)$ and $(h,0,\bar{2})$ from experiments 92

6.1 3-site unit cell for SCGA on stacked kagome layers 94
6.2 Band structure for kagome adjacency matrix 97

7.1 Spin autocorrelation without total magnetisation suppressed 109
7.2 Spin autocorrelation with total magnetisation suppressed 109
7.3 Spin autocorrelation with $K = 1$ in Eq. (7.4) 110
7.4 Spin autocorrelation for different system sizes 111
7.5 Spin autocorrelation using spinwaves and molecular dynamics 113
7.6 Spin autocorrelation on long timescales 114
7.7 Rescaled spin autocorrelation for kagome layer sites 114
7.8 Spin autocorrelation for the pyrochlore lattice 115
7.9 Integrated density of states 116

CHAPTER 1

Introduction

> A poet once said, "The whole universe is in a glass of wine." We will probably never know in what sense he meant that, for poets do not write to be understood. But it is true that if we look at a glass of wine closely enough we see the entire universe. There are the things of physics: the twisting liquid which evaporates depending on the wind and weather, the reflections in the glass, and our imagination adds the atoms...
>
> — *Richard P. Feynman*

Physics and mathematics have been spectacularly successful approaches to understanding the natural world, even from the time of Archimedes and the theories of classical mechanics in the time of Galileo. Thermodynamics had a huge role in powering the industrial revolution, and in the development of the concept of entropy. Advances in the last century have been no less astounding, revolutionising our ideas about space and time, light and matter. Much of this work is driven by intellectual curiosity. And while the practical uses of new discoveries are not always immediately obvious, they are undeniable — the explosion of the digital age is just one example of transformative technologies made possible by fundamental research.

The enterprise of physics is grounded on very solid foundations, and there is a healthy culture of rigorous discussion and debate on an international scale. Generations of physicists have contributed to the deep pool of evidence and insights gathered in support of our current understanding of the natural world. This situation is well described by Newton's use of a metaphor due to Bernard of Chartes, on seeing further "by standing on the shoulders of giants". The roles of theory and experiment are equally important in building confidence in our accumulated knowledge, and I am proud to play a small part in this great tradition. We have been able to carefully build up an ever-expanding conception of our universe because of the discipline in physics of establishing error bars around possibilities and predictions.

In this introductory chapter, I will first describe the broad framework of statistical

physics that we use to discuss condensed matter systems. We then focus on magnetic systems in particular before zooming in on geometrically frustrated magnets, discussing motivations for studying them and providing relevant background material. To conclude this chapter, the structure for the rest of this thesis is outlined in Section 1.4.

1.1 Statistical physics

Complexity is a matter of perspective. There are more than 10^{23} molecules jostling around in a glass of water, which we can quite rightly describe as doing nothing interesting. Statistical physics is the perspective that reconciles these seemingly divergent descriptions of nature, by deriving the collective behaviour of a system from the mechanical laws that govern the constituent particles. Rather than carefully keeping track of the motion of any given particle, taking the statistical average over space and time allows the essence of the system to emerge. The concept of probability is central to such an approach, in much the same way that the outcome of a single throw of a dice, influenced by every last detail of the collisions and rotations, is unpredictable — yet if the dice is fair, the outcome of a large number of dice throws is well approximated by the uniform distribution.

In statistical physics, we imagine a physical system to be in some state X_i at any given moment of time, where the collection of all possible states (called the ensemble) is weighted by a probability distribution $\{P(X_i)\}$. The system can be characterised by expectation values, which are statistical measures such as the mean

$$\langle \mathcal{O} \rangle = \sum_i \mathcal{O}(X_i) P(X_i) \tag{1.1}$$

of properties $\mathcal{O}$ that are defined for each state. An important idealisation is of a closed system in thermal equilibrium with a heat bath. For this case, we consider the so-called *canonical ensemble*, where the probability for the system to be in a particular state is proportional to the *Boltzmann weight*, i.e.,

$$P(X_i) = \frac{1}{\mathcal{Z}} \exp(-\beta E_i) \, .$$

Here E_i is the energy of the state X_i, and $\beta = 1/k_B T$ is the inverse temperature. The

partition function is the normalisation factor

$$\mathcal{Z} = \sum_i \exp(-\beta E_i) \; . \tag{1.2}$$

Monte Carlo simulation is a very general and powerful numerical technique to work out statistical expectation values in the spirit of Eq. (1.1). The basic idea is to approximate difficult integrals (sums) by doing random sampling, and to get an accurate enough answer with a reasonable number of samples. The philosophy and algorithms involved are well explained in books such as the one by Krauth (see Ref. [1]). We will make extensive use of Monte Carlo simulations in this thesis, for the purpose of generating random system configurations drawn from a thermal distribution.

1.1.1 Condensed matter systems

Condensed matter physics refers to the study of physical systems such as liquids and solids, where the constituent particles are in a condensed state. Statistical physics is an important framework for such systems, in addition to knowing the laws of electrodynamics and quantum physics that govern the interactions between the particles. The close packing of particles in the condensed state usually means that in order to obtain a qualitatively correct picture, the interactions between particles must be taken into account. The diversity of systems falling under this description presents important and interesting challenges to physicists. Condensed matter systems can usually be subjected to an array of experimental probes in the laboratory, as samples of relevant size are of reasonable scale. There is thus fertile opportunity for progress in this field as experimental data inspire theoretical ideas and predictions from theory, including numerical simulations, can be tested by experiments.

Emergence is a buzzword that quite accurately captures the excitement of studying condensed matter systems. The collective modes of a system can behave very differently from the degrees of freedom that describe its constituent particles. Fractionalisation is a dramatic "magic trick" that nature has been known to play, where quasiparticle excitations from exotic states of matter divide the supposedly indivisible: examples being quasi-electrons with fractional charge in the fractional quantum Hall effect [2] and deconfined magnetic monopoles in 'spin ice' compounds. [3]

1.1.2 Correlations

We can characterise a physical system by calculating expectation values Eq. (1.1). The simplest properties we might be interested in are those that only involve individual particles, such as the mass or speed of particles in a liquid. The next level of complexity involves pair correlations, where the observables are defined for pairs of particles. For the case of a liquid again, an example might involve the probability of finding another particle at a given radius from a particle at the origin.

Correlation functions like the scalar product of the velocity vectors of liquid particles can even be defined across both space and time. Such correlation functions involve a more detailed understanding of a system, and are also experimentally relevant, as the scattering cross-section (of x-rays, electrons, or neutrons) effectively gives the Fourier transform of particle correlations. The experimental technique of magnetic neutron scattering is particularly important for us because of our interest in spin correlations. Neutrons are useful for such studies as they have neutral charge and thus interact relatively weakly with matter, penetrating the bulk to probe the microscopic magnetic fields in a sample.

1.1.3 Topological defects

At high temperatures, systems of particles are generally uncorrelated and disordered. This high temperature state has the full translational and rotational symmetry of the vacuum. As temperature is lowered, some of this symmetry may be broken, leading to a new phase of matter. For example, below the Curie temperature, a simple ferromagnet gains a magnetic moment that picks out a particular direction in space.[†]

The broken symmetry phase is specified by what is known as an *order parameter*. For the ferromagnet, the order parameter space is the surface of a sphere, as the magnetic moment can point in any direction. While a uniform system is characterised by a global order parameter, for a broken continuous symmetry, the order parameter can also vary locally, with the variation being continuous outside of isolated defect regions.

We can use the language of topology to characterise the stable defects in systems with broken continuous symmetry. The general framework is described pedagogically and

[†]The analogous critical temperature for an antiferromagnet is known as the Néel temperature.

illustrated with many examples in a review by Mermin (see Ref. [4]). Loosely speaking, the defect regions are topologically stable if they cannot be "smoothed away" by continuous local deformations around the defects. Such defects consist of a core region where the order is destroyed (generally with a high energy cost), but these defects remain stable at low temperature because drastic changes in the order parameter are required to destroy the defect.

For a 2D system, point defects can be enclosed by a loop. As we are assuming that the order parameter varies continuously along such a loop, the value of the order parameter around the loop defines a mapping f from the loop to a closed curve in the order parameter space. Since topological defects must be stable against continuous local deformations, a defect corresponds to the family of mappings that are related to f by such deformations. Mathematically, these deformations are known as homotopies and topological defects correspond to the *homotopy classes* of the order parameter space. The combination of defects takes on the group structure of the homotopy classes. In particular, for a 2D system, the so-called *fundamental group* of the order parameter space gives the rules for combining point defects. The basic idea of this is illustrated schematically in Fig. 1.1.

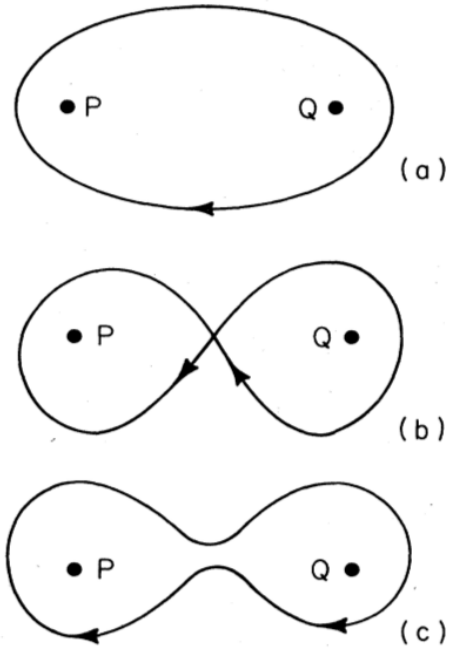


Figure 1.1: Cartoon of point defect combination in a 2D system. P and Q represent point defects, and the contour in (a) maps to the homotopy class of the combined defect. Through deformations of the contour such as shown in (c), the homotopy class of the combined defect is the same as the group product of the homotopy classes determined by P and Q separately in the two contours in (b). Taken from Ref. [4].

1.2 Magnetism

Magnetism in atoms and ions gives rise to a rich diversity of magnetic systems. As we shall see in Section 1.3, one particularly intriguing possibility is geometrically frustrated magnetism, which we study in this thesis under the framework of statistical physics.

1.2.1 Magnetic models

We will use the Heisenberg model as a theoretical description of magnetic interactions in this thesis. The basic motivation for this model is that the energy splitting between singlet and triplet states for a pair of spin $S = \frac{1}{2}$ electrons can be expressed as the scalar product of the spin operators. This coupling between spins is termed an *exchange interaction*, as it is a consequence of wavefunction anti-symmetrisation for identical (fermionic) electrons. More generally, in an insulating solid with many ions, we consider the spin Hamiltonian

$$\hat{\mathcal{H}} = \tfrac{1}{2} \sum_{i,j} J_{ij} \hat{\boldsymbol{S}}_i \cdot \hat{\boldsymbol{S}}_j \tag{1.3}$$

known as the Heisenberg Hamiltonian. This model assumes isotropic interactions between localised spin degrees of freedom, and the exchange interaction J_{ij} between spins $\hat{\boldsymbol{S}}_i$ and $\hat{\boldsymbol{S}}_j$ is ferromagnetic if $J_{ij} < 0$, and antiferromagnetic if $J_{ij} > 0$.

In quantum mechanics, the time-evolution of an operator is given by the commutator with the Hamiltonian, i.e.,

$$i\hbar \frac{d}{dt} \hat{\boldsymbol{S}}_i = [\hat{\boldsymbol{S}}_i, \hat{\mathcal{H}}] \, . \tag{1.4}$$

We put Eq. (1.3) into Eq. (1.4) to derive the spin dynamics of the Heisenberg model. Using the spin commutation relations for the Cartesian components of a single spin, i.e.,

$$[\hat{S}_i^x, \hat{S}_i^y] = i\hat{S}_i^z \, , \quad \text{etc.}$$

we find that the equations of motion describe the precession of each spin about its local field,

$$\frac{d\hat{\boldsymbol{S}}_i}{dt} = \hat{\boldsymbol{S}}_i \times \hat{\boldsymbol{H}}_i \, , \text{ where the local field } \hat{\boldsymbol{H}}_i \equiv -\sum_j \frac{J_{ij}}{\hbar} \hat{\boldsymbol{S}}_j \, . \tag{1.5}$$

We obtain a classical version[†] of the Heisenberg model when the spin S is large. In this classical Heisenberg model, we treat each spin as an ordinary vector of length S, and replace the commutators with Poisson brackets. The classical counterparts to Eq. (1.3) and Eq. (1.5) are

$$\begin{cases} \mathcal{H} = \frac{1}{2}\sum_{i,j} J_{ij}\boldsymbol{S}_i \cdot \boldsymbol{S}_j \\ \dfrac{d\boldsymbol{S}_i}{dt} = \boldsymbol{S}_i \times \boldsymbol{H}_i \ , \ \text{with} \ \ \boldsymbol{H}_i \equiv -\sum_j \dfrac{J_{ij}}{\hbar}\boldsymbol{S}_j \ . \end{cases} \tag{1.6}$$

For large S, a strongly correlated classical regime opens up, where $JS \ll T$ so that quantum effects can be neglected, and $T \ll JS^2$ so that thermal disorder is negligible relative to the scale of the classical interactions.

The classical Heisenberg model is also the $n = 3$ member of a family of $O(n)$ vector spin models. In this family of spin models, a spin is represented by a classical unit vector on the $(n-1)$-sphere. The spin models corresponding to $n = 1$ and $n = 2$ are known as the Ising and XY models respectively. The $n \to \infty$ limit is known as the spherical model.[5]

1.2.2 Susceptibility and mean field theory

The magnetic susceptibility χ characterises the linear response of a system to an applied magnetic field. In this subsection, we first consider a paramagnet of identical free ions and show that its susceptibility follows a $\chi \sim 1/T$ law at high temperature. We consider the leading correction from Heisenberg interactions, which modifies this high-temperature law to $\chi \sim 1/(T-\theta)$, where θ is the *Curie-Weiss constant*. We outline a simple mean-field argument that predicts an ordering transition at $T_c = \theta$ for ferromagnets. Our derivation follows the classic textbook by Ashcroft and Mermin (see Ref. [6]).

To avoid possible confusion between the Heisenberg exchange J and the symbol commonly used for the total angular momentum of an ion, we use S for the latter in the context of spin models. A small applied field $H \parallel z$ splits the degenerate ground states into states of definite S^z, so for a single ion the partition function Eq. (1.2) is

$$\mathcal{Z} = \sum_{S^z=-S}^{+S} \exp\left(-g\mu_B S^z H/k_B T\right) \ , \tag{1.7}$$

[†]We should say *semiclassical* because the origin of spin is inherently quantum mechanical, but we choose not to for the sake of brevity.

where g is the Landé g-factor and μ_B is the Bohr magneton. The magnetic Helmholtz free energy is $F = -k_B T \log \mathcal{Z}$ and the magnetisation density for N free ions in a volume V is

$$M = -\frac{N}{V}\frac{\partial F}{\partial H} \,. \tag{1.8}$$

Taking the geometric sum in Eq. (1.7) and putting it into Eq. (1.8) gives

$$M = \frac{N}{V} g\mu_B S \cdot B_S\left(\frac{g\mu_B S H}{k_B T}\right) \,, \tag{1.9}$$

where $B_S(x)$ is the *Brillouin function*

$$B_S(x) = \frac{2S+1}{2S}\coth\left(\frac{2S+1}{2S}x\right) - \frac{1}{2S}\coth\left(\frac{1}{2S}x\right) \,. \tag{1.10}$$

The magnetic susceptibility $\chi = \partial M/\partial H$ simplifies at high temperatures $k_B T \gg g\mu_B S H$, where we can make the small x expansion for $B_S(x)$ to get the leading term

$$\chi = \frac{N}{V}(g\mu_B)^2 \frac{S(S+1)}{3k_B T} \,. \tag{1.11}$$

This T^{-1} dependence of the paramagnetic susceptibility at high temperatures is known as the *Curie law*.

We now consider the Heisenberg model with the Hamiltonian Eq. (1.3). Since

$$\chi = \frac{g\mu_B}{V}\frac{\partial}{\partial H}\Big\langle \sum_i \hat{S}_i^z \Big\rangle\Big|_{H=0} = \frac{1}{V}(g\mu_B)^2 \frac{1}{k_B T}\Big\langle \big(\sum_i \hat{S}_i^z\big)^2 \Big\rangle \,, \tag{1.12}$$

we see that the susceptibility is proportional to the spin correlation function (calculated in zero applied field). In the limit of infinite temperature, spins at different sites are completely uncorrelated, so

$$\langle \hat{S}_i^z \hat{S}_j^z \rangle_{T\to\infty} = \delta_{ij}\frac{S(S+1)}{3} \,. \tag{1.13}$$

We recover the Curie law Eq. (1.11) by putting Eq. (1.13) into Eq. (1.12). To calculate the leading correction at high temperature, we approximate the statistical weight

$$e^{-\beta\hat{\mathcal{H}}} \approx 1 - \beta\hat{\mathcal{H}} \tag{1.14}$$

so the spin correlations are given by

$$\langle \hat{S}_i^z \hat{S}_j^z \rangle \approx \frac{\frac{1}{3}S(S+1)\delta_{ij} - \beta\langle \hat{S}_i^z \hat{S}_j^z \hat{\mathcal{H}}\rangle_{T\to\infty}}{1 - \beta\langle\hat{\mathcal{H}}\rangle_{T\to\infty}} \,. \tag{1.15}$$

The trick is to again calculate the expectation values on the right-hand side of Eq. (1.15) in the infinite temperature limit with uncorrelated spins, which gives

$$\left\langle \hat{S}_i^z \hat{S}_j^z \right\rangle \approx \delta_{ij} \frac{S(S+1)}{3} - \beta J_{ij} \left(\frac{S(S+1)}{3} \right)^2 . \tag{1.16}$$

Putting Eq. (1.16) back into Eq. (1.12) gives the *Curie-Weiss law*

$$\chi \approx \frac{N}{V} (g\mu_B)^2 \frac{S(S+1)}{3k_B T} \left(1 + \frac{\theta}{T} \right) , \tag{1.17}$$

where the *Curie-Weiss constant* is

$$\theta = -J_0 \frac{S(S+1)}{3k_B} \qquad \text{with} \quad J_0 \equiv \frac{1}{N} \sum_{i,j} J_{ij} . \tag{1.18}$$

For a simple Heisenberg ferromagnet ($J_0 < 0$), a mean-field approximation predicts an ordering transition below $T_c = \theta$. The magnetisation density is related to the average spin by

$$\boldsymbol{M} = \frac{N}{V} g\mu_B \langle \boldsymbol{S} \rangle . \tag{1.19}$$

If we assume that all spins take on the same value, then on a Bravais lattice, each spin experiences the same effective field

$$\boldsymbol{H}_{eff} = \boldsymbol{H} - \frac{J_0}{g\mu_B} \langle \boldsymbol{S} \rangle = \boldsymbol{H} - \frac{V}{N} \frac{J_0}{(g\mu_B)^2} \boldsymbol{M} . \tag{1.20}$$

This allows us to use Eq. (1.9) for the magnetisation density of free ions with H_{eff} instead of H, which leads to a self-consistent condition for M. We can interpret this self-consistent condition for M graphically in the limit $H \to 0$, by expressing it as the simultaneous equations

$$\begin{cases} M = \dfrac{T}{\lambda} x , \quad \text{with} \quad \lambda = -J_0 \dfrac{V}{N} \dfrac{S}{g\mu_B k_B} \\ M = \dfrac{N}{V} g\mu_B S \cdot B_S(x) \end{cases} \tag{1.21}$$

and looking for intersections when M is plotted against x. There is always a valid solution at $x = 0$ with $M = 0$. The system has a *spontaneous magnetisation* if there is also a solution for $M > 0$. As the Brillouin function is convex, intersections at $M > 0$ occur for $T < T_c$, where the mean-field transition temperature T_c is obtained when the graphs in

Eq. (1.21) are *tangent* at $x = 0$. Since

$$\left.\frac{\mathrm{d}B_S}{\mathrm{d}x}\right|_{x=0} = \frac{S+1}{3S} ,$$

we find that

$$T_c = \lambda \frac{N}{V} g\mu_B S \frac{S+1}{3S} = \theta . \tag{1.22}$$

For simple unfrustrated antiferromagnets, the mean-field argument can be adapted to give a similar conclusion. In this case, we have $\theta < 0$ and a spontaneous *staggered magnetisation* is predicted for $T < T_N$, where the Néel temperature $T_N = |\theta|$ under this approximation.

1.3 Geometrically frustrated magnetism

Magnetic systems on a regular lattice allow us to engineer situations in which the competing interactions cannot be simultaneously satisfied and "frustrate" the onset of order. The geometric origin of such frustration distinguishes these frustrated magnets from other disordered systems with quenched disorder, for example in metallic spin glasses, where the varying sign and strength of the interactions between impurity magnetic ions results in a complex energy landscape.

By avoiding conventional periodic order, geometrically frustrated magnets allow us to access potentially novel collective behaviour and exotic emergent excitations. As discussed in a review by Balents (see Ref. [7]), frustrated magnets typically exist in a strongly fluctuating *spin liquid* state, which can be classical or quantum. While the positional correlations in a fluid are short-ranged, a classical spin liquid can have subtle long-range spin correlations, such as the Coulomb phase correlations in spin ice.[8] Quantum spin liquids can form a state entangling spins far apart, such as a resonanting valence bond (RVB) state proposed by Anderson as an underlying mechanism for high-T_c superconductivity.[9]

While we are always free to dream up theories of exotic states, an advantage of studying exotic states in geometrically frustrated magnets is the possibility of strong contact with experiment. Advances in crystal synthesis and sample characterisation have opened up a great variety of frustrated magnets to experimental study, at once constraining theoretical

speculation with experimental evidence and inspiring theoretical ideas with surprising data.

1.3.1 Experimental signatures of frustration

Well-established experimental techniques provide evidence of the avoidance of order characteristic of frustrated magnets. Schematically, experimental signatures of frustration in the susceptibility and in magnetic neutron scattering data are indicated in Fig. 1.2. We will discuss each of these in turn.

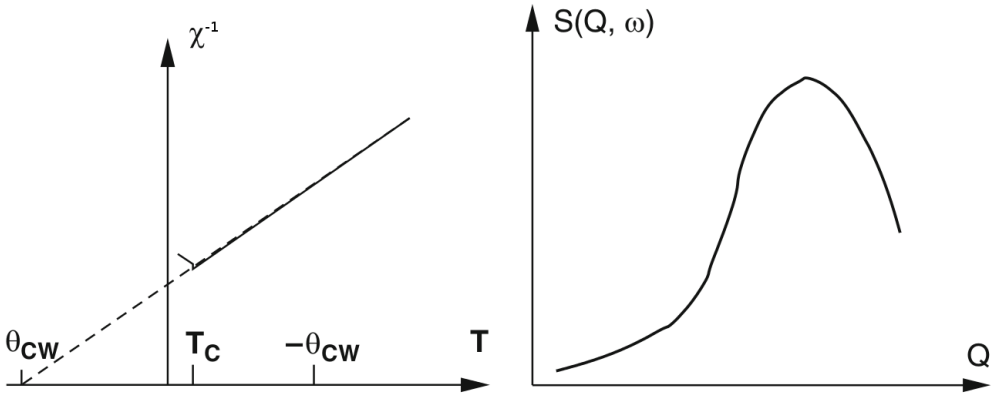


Figure 1.2: *(Left):* Expected behaviour of the inverse susceptibility as a function of temperature for a frustrated magnet. *(Right):* Expected behaviour of the dynamic structure factor from magnetic neutron scattering, as a function of wavevector. Both figures taken from Ref. [10].

The temperature dependence of the susceptibility Eq. (1.17) for Heisenberg spins can be expressed as

$$\chi^{-1}(T) \propto T\left(1+\frac{\theta}{T}\right)^{-1} = T - \theta + O\left(\frac{\theta^2}{T}\right) \ . \tag{1.23}$$

Experimentally, we can obtain an estimate θ_{CW} for the Curie-Weiss constant by measuring the high-temperature susceptibility and performing a linear fit to $\chi^{-1}(T)$. The exchange interaction can then be estimated using Eq. (1.18). In simple unfrustrated antiferromagnets, we expect that $\chi^{-1}(T)$ does not follow a linear trend near or below the Néel ordering temperature $T_N \sim |\theta_{CW}|$. As frustrated magnets avoid ordering, the linear fit to $\chi^{-1}(T)$ continues to hold even for $T_c < T < |\theta_{CW}|$. In real materials, there is usually a transition temperature T_c as the frustration is relieved due to perturbations (e.g., due to lattice distortions or further neighbour exchange interactions) eventually becoming important at low temperatures. Ramirez thus proposed that a useful diagnostic for identifying highly

frustrated magnets is[11]

$$f \equiv \frac{|\theta_{CW}|}{T_c} \gg 1 \, . \tag{1.24}$$

Since frustrated magnets usually have short-ranged antiferromagnetic spin correlations, we expect a broad peak at a finite wavevector Q from magnetic neutron scattering. Unlike unfrustrated antiferromagnets, there are no sharp magnetic Bragg peaks indicative of long-range Néel order. Also, unlike short-ranged ferromagnetic correlations, the peak intensity is shifted away from $Q = 0$.

1.3.2 Order by disorder

In classical geometrically frustrated magnets, the degeneracy of ground states suggests that if quantum effects are neglected, the system avoids order at $T = 0$. Nonetheless, an entropic mechanism can paradoxically lead to order at finite low temperatures, in what is known as order by disorder.[12]

The set of ground states generally forms a manifold within high-dimensional phase space. Locally, we let the coordinates parallel and perpendicular to this manifold be $\boldsymbol{x}$ and $\boldsymbol{y}$ respectively. At low temperatures, we just consider the leading quadratic term in the energy cost of moving away from the ground state manifold. Following Moessner and Chalker,[13,14] we have the Hamiltonian

$$\mathcal{H} \approx \mathcal{H}_2 = \sum_l \epsilon_l(\boldsymbol{x}) y_l^2 \, , \tag{1.25}$$

where we have chosen coordinates $\{y_l\}$ that diagonalise the quadratic form. The contribution to the partition function of the states near the ground state manifold is

$$\mathcal{Z}(\boldsymbol{x}) = \int \prod_l \mathrm{d}y_l \, \exp(-\mathcal{H}_2/k_B T) \propto \prod_l \left[\frac{k_B T}{\epsilon_l(\boldsymbol{x})}\right]^{1/2} \, . \tag{1.26}$$

If there are certain ground states $\boldsymbol{x}_0$ where some of the ϵ_l vanish (i.e., those y_l are *soft modes*), then $\mathcal{Z}(\boldsymbol{x})$ diverges near such points. If these divergences are non-integrable, we need to fix this by keeping the higher-order terms in the Hamiltonian Eq. (1.25). Such higher-order terms concentrate $\mathcal{Z}(\boldsymbol{x})$ on those ground states $\boldsymbol{x}_0$. For example, while quadratic modes contribute factors of $T^{1/2}$ to the partition function, quartic modes contribute factors of $T^{1/4}$ that dominate at low T. This selection of ground states due to thermal fluctuations

is depicted schematically in Fig. 1.3.

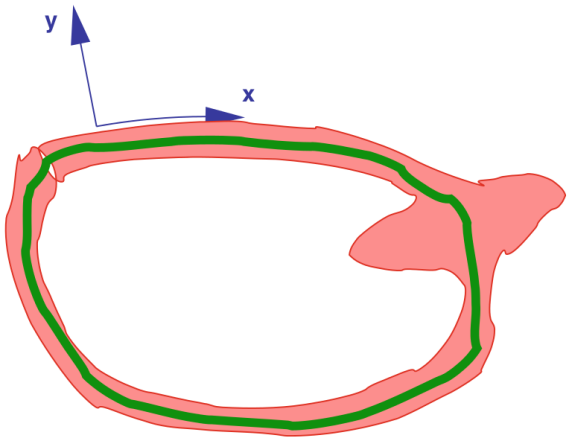


Figure 1.3: Schematic of the order by disorder mechanism. The ground state manifold is indicated as a green line in high-dimensional phase space, and the coordinates $\boldsymbol{x}$ and $\boldsymbol{y}$ are parallel and perpendicular to this manifold respectively. The shaded region indicates the states accessible to the system at low temperature, and the bulging region (on the right side of the figure) indicates that certain ground states have a lot of nearby states that are accessible at low energy. If the area of this bulging region dominates the rest of the area around the ground state manifold, then those special ground states are selected through order by disorder. Taken from Ref. [10].

1.3.3 The kagome and pyrochlore lattices

The triangle is the simplest polygon with an odd number of edges, and thus forms a basic motif in geometrically frustrated magnetism. Frustrated structures in two spatial dimensions (2D) are built up from regular arrangements of triangles, such as in the triangular (edge-sharing) and kagome (corner-sharing) lattices. The simplest way of extending the triangle into three spatial dimensions is to add a vertex above to form a tetrahedron with four triangular faces. In 3D, repeating tetrahedral units in space can give the face-centred-cubic (edge-sharing) and pyrochlore (corner-sharing) lattices. Note that corner-sharing lattices potentially have a higher ground state degeneracy than edge-sharing ones, because only a single spin is shared between neighbouring units. The corner-sharing kagome and pyrochlore lattices are shown in Fig. 1.4.

We highlight some theoretical background on the kagome and pyrochlore lattices, as these are well-studied frustrated lattices that serve as reference points for discussing the extended kagome lattice that we study in this thesis. For these two corner-sharing systems, consider Heisenberg spins with antiferromagnetic nearest-neighbour interactions, and the same coupling $J > 0$ on all nearest-neighbour bonds. The classical Hamiltonian is

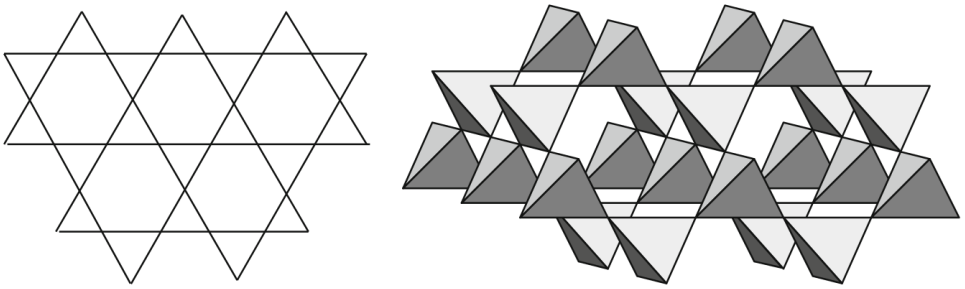


Figure 1.4: The frustrated 2D kagome (left) and 3D pyrochlore (right) lattices. Taken from Ref. [10].

$\mathcal{H} = J \sum_{\langle ij \rangle} \boldsymbol{S}_i \cdot \boldsymbol{S}_j$, where we use the notation $\langle ij \rangle$ to index all nearest-neighbour sites i and j. Each spin belongs to two corner-sharing *units* (triangular units for the kagome, tetrahedral units for the pyrochlore), and we can index these units by α. By defining

$$\boldsymbol{L}_\alpha = \sum_{i \in \alpha} \boldsymbol{S}_i \ ,$$

we can rewrite the classical Hamiltonian as

$$\mathcal{H} = \frac{J}{2} \sum_\alpha |\boldsymbol{L}_\alpha|^2 + \text{constant.} \tag{1.27}$$

This shows us that the classical ground states must all satisfy a *sum rule* for each unit, i.e., $\boldsymbol{L}_\alpha = 0$ for each α. These rules impose some structure on the spins in ground states. For the kagome system, the spin configuration of a triangular unit is *rigid* and has no internal degrees of freedom apart from a common rotation of all three spins. For the pyrochlore system, the spin configuration of a unit of four spins has two continuous internal degrees of freedom, and the condition that the spins sum to zero for each unit is relatively *soft* and can be satisfied in many ways.

The classical ground state manifold is known to be connected for both systems, meaning that it is possible to continuously deform any ground state spin configuration into any other ground state spin configuration, without leaving the space of ground states.[13,14] The number of ground state degrees of freedom is also extensive for both lattices (i.e., proportional to the number of spins in the system). For the kagome lattice, the ground states where all spins are *coplanar* are of special importance, as all other ground states can be generated from them by the introduction of local zero modes.[15,16] Chalker et al. showed that these coplanar states are selected due to the order by disorder mechanism.[15] For the

pyrochlore lattice, the order by disorder mechanism does not apply, and the system is not trapped near any particular ground state at low temperatures.[14]

1.4 Outline for the thesis

The rest of this thesis focuses on geometric frustration in the extended kagome lattice, also known as the swedenborgite lattice due to the structural similarity with the mineral. The extended kagome lattice possesses a novel magnetic geometry that was experimentally realised and reported in the literature 12 years ago.[17] We present the results of our theoretical efforts to understand the static and dynamic properties of the Heisenberg model on this lattice.

In Chapter 2, we review the experimental literature on this system, and introduce the spin model that we base our work on. The next two chapters are on the static properties of the model. We discuss classical ground states in Chapter 3, and present results for spin correlations at finite temperature using the self-consistent Gaussian approximation (SCGA) in Chapter 4. The subsequent three chapters focus on various approaches to the spin dynamics. Chapter 5 describes excitations in the language of linear spinwave theory. We show how this approach can be used to calculate the dynamic structure factor numerically. The results of such calculations are compared against experimental data obtained from inelastic magnetic neutron scattering. In Chapter 6, we derive a prediction about the slow dynamics at low temperatures using the stochastic SCGA approach developed recently for the pyrochlore lattice. This prediction is tested in Chapter 7 using molecular dynamics simulations, where we find a surprisingly fast relaxation of the spins in the kagome sublattice. We summarise our main results and discuss directions for future work in Chapter 8.

CHAPTER 2

The extended kagome lattice

> There is a great difference between knowing and understanding: you can know a lot about something and not really understand it.
>
> — *Charles F. Kettering*

We turn now to a review of the extended kagome lattice, which is the geometrically frustrated system we study in this thesis. The plan for this chapter is to first survey the experimental literature on relevant materials, and describe their magnetic properties. We then explain why we choose an isotropic Heisenberg model for our theoretical description of the system.

2.1 Materials and experiments

We begin this section with the identification of various compounds with the extended kagome structure. We subsequently delve into the magnetism in these compounds, focusing on details that help guide our theoretical focus.

2.1.1 Class of compounds

In 2002, Valldor and Andersson reported on a new magnetic compound $YBaCo_4O_7$.[17] This compound has a hexagonal structure, and is isostructural with the mineral swedenborgite, $NaBe_4SbO_7$, whose structure was characterised in the 1930's.[18] The magnetic sublattice of cobalt (Co) spins forms a so-called *extended kagome lattice*, due to the way the cobalt ions form alternating kagome and triangular layers.[19,20]

We are interested in compounds with magnetic ions on an extended kagome lattice, and we will identify a list of them in this subsection. We are particularly interested in the specific properties of $YBaCo_4O_7$, as we are actively collaborating with R. I. Bewley and T. G. Perring from ISIS on this compound. Our collaborators have obtained data from high-resolution inelastic magnetic neutron scattering at very low temperatures, on a

single-crystal sample prepared by J. F. Mitchell at Argonne. The experiments were done on an oxygen-rich sample, as the excess oxygen suppresses the structural phase transition and long-range magnetic order found in stoichiometric $YBaCo_4O_7$.[21]

Our list of interesting compounds includes the family of '114' cobaltites, $R\mathrm{BaCo_4O_7}$, where R is one of the rare earth elements, such as yttrium (Y) or one of the lanthanides. In these compounds, the oxidation state of the R cation is +3, and the average cobalt oxidation of +2.25 indicates a ratio of 3 Co^{2+}:1 Co^{3+}. The cobalt ions are tetrahedrally coordinated by oxygen, and there are inequivalent Co1 and Co2 sites in a 1:3 ratio (see Fig. 2.1). We shall refer to the Co1 and Co2 sites as the *triangular* and *kagome* sites respectively. Many of these cobaltites were characterised by Valldor,[22] and their magnetic properties have since been studied in detail by many others as well.[19,20,23–33]

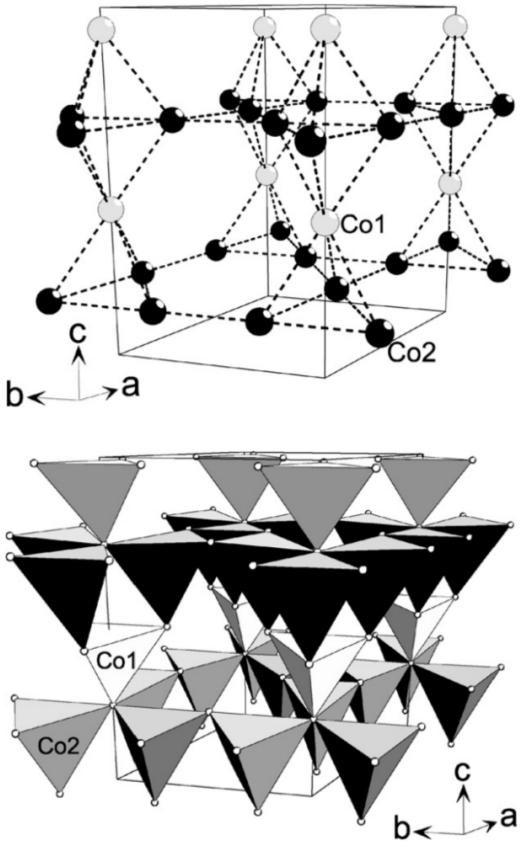


Figure 2.1: (top) The magnetic framework of cobalt ions in $R\mathrm{BaCo_4O_7}$, with inequivalent sites Co1 and Co2. (bottom) The Co-O substructure showing the CoO_4 tetrahedra. Taken from Ref. [34]
.

The '114' ferrites, $R\mathrm{BaFe_4O_7}$, are closely related magnetic compounds. Of these, we are interested in those with a hexagonal structure, such as $TbBaFe_4O_7$ and $GdBaFe_4O_7$,

and not in those involving the smaller lanthanides, which have a cubic structure.[35,36] The iron (Fe) ions in the hexagonal structures form an extended kagome lattice, while the iron in the cubic structures form a pyrochlore lattice (see Fig. 2.2).

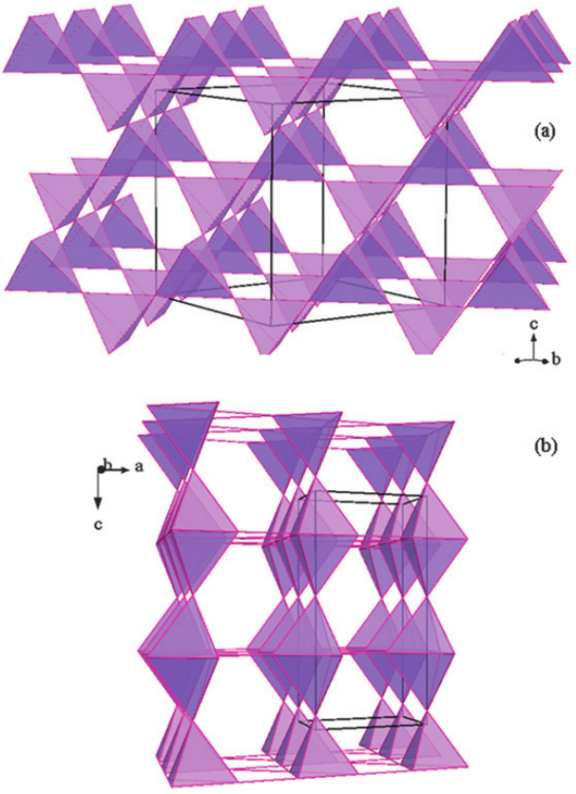


Figure 2.2: The magnetic framework of iron ions in (a) cubic $R\mathrm{BaFe_4O_7}$, and (b) hexagonal $R\mathrm{BaFe_4O_7}$. Taken from Ref. [35].

Another interesting compound with the same extended kagome structure is $\mathrm{YBaCo_3FeO_7}$, which avoids magnetic long-range order down to 1 K.[37,38] From x-ray absorption spectroscopy, cobalt and iron were only found in the pure Co^{2+} and Fe^{3+} states,[39] and iron preferentially occupies the Co1 triangular sites to 82(2)% and the Co2 kagome sites only to 6(1)%, as determined by Mössbauer spectroscopy.[38] Khalyavin et al. argue that the weak ferromagnetic component observed along the c axis could be explained by long-range chiral ordering.[40]

While the R cation in the '114' cobaltites and ferrites can also be replaced by calcium (Ca), quite a significant structural distortion is introduced due to the smaller Ca^{2+} cation. The average oxidation state of cobalt and iron in $\mathrm{CaBaCo_4O_7}$ and $\mathrm{CaBaFe_4O_7}$ respectively is also higher, as a result of the lower oxidation state of calcium relative to the rare

earths. We are interested in the ferrite as it turns out that $CaBaFe_4O_7$ has a hexagonal structure,[41,42] but are less interested in the cobaltite, which has a large orthorhombic distortion and strong buckling of the kagome layers.[43,44]

2.1.2 Geometry of magnetic sublattice

The extended kagome lattice is a 3D structure composed of two types of corner-sharing units, namely uncapped and bicapped triangles (see Fig. 2.3). We shall often refer to the uncapped triangles simply as *triangles*, and to the bicapped triangles as *bipyramids*. The triangles and bipyramids alternate within a layer to form a kagome structure. We will refer to the spins in the kagome layers as *kagome (lattice) spins*, and to the apical spins in the bipyramids as *triangular (lattice) spins*, since the latter form triangular lattice layers. We can thus describe the extended kagome lattice as having alternating kagome and triangular layers.

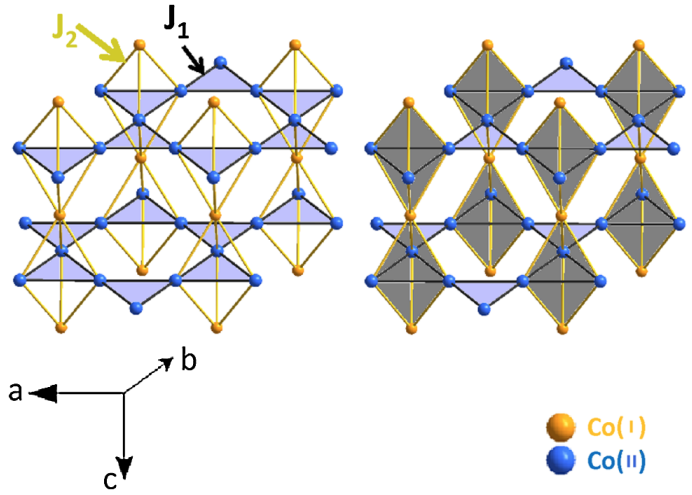


Figure 2.3: Illustration of the extended kagome structure of $YBaCo_4O_7$. There are two types of cobalt sites, represented by orange and blue balls. The Co(II) sites form kagome planes interwoven with triangular layers of Co(I) sites. The black and orange sticks represent the exchange interactions J_1 (within the kagome plane) and J_2 (between planes). The corner-sharing triangles in the kagome plane are coloured in blue, and in the right panel, the corner-sharing bipyramids are coloured in dark gray to aid visualisation. Taken from Ref. [20].

We denote the antiferromagnetic exchange interactions in-plane and out-of-plane by J_1 and J_2 respectively in our Heisenberg Hamiltonian Eq. (2.2). Khalyavin et al. performed a spin-dimer analysis following an approach by Whangbo et al.[45,46] to argue that with the hexagonal structure, a single exchange parameter was expected, i.e., $J_1 = J_2 \equiv J$.[47] Detailed structural studies of $YbBaCo_4O_7$[24] and $TmBaCo_4O_7$[26] have revealed however that the real

symmetry for oxygen stoichiometric samples is trigonal rather than hexagonal. This lower symmetry could lift the frustration, even though it still preserves the threefold symmetry of the bipyramids and triangles. Nonetheless, the spin-dimer analysis by Khalyavin et al. shows that the main effect of trigonal distortions is a change to the out-of-plane interactions, which justifies considering an idealised case with two parameters J_1 and J_2.[47]

2.1.3 Magnetic susceptibility and phase transitions

The '114' cobaltites and ferrites tend to be good oxygen absorbers, with $YBaCo_4O_{7+\delta}$ being a prominent candidate as an oxygen storage material.[48] The structural and magnetic properties of $YBaCo_4O_{7+\delta}$ are sensitively dependent on the oxygen stoichiometry.[21] As such, we shall review results for the stoichiometric $YBaCo_4O_{7.0}$ compound before discussing recent reports on oxygen-rich samples.

For stoichiometric $YBaCo_4O_7$, Chapon et al.[19] measured the magnetic susceptibility (see Fig. 2.4) and found that the Curie-Weiss constant $\theta_{CW} = -508$ K, indicating antiferromagnetic interactions. Fitting the high-temperature susceptibility data to Eq. (1.17) gives an effective magnetic moment per formula unit of $8.9\,\mu_B$. This agrees quite well with the calculated $8.3\,\mu_B$ per formula unit, for a mixed oxidation state of 3 Co^{2+}:1 Co^{3+} (assuming no orbital angular momentum, with $S = \frac{3}{2}$ for Co^{2+} and $S = 2$ for Co^{3+}). Hollmann et al.[39] found from x-ray absorption spectroscopy that both Co^{2+} and Co^{3+} are indeed in the high-spin state (i.e., $S = \frac{3}{2}$ and $S = 2$ respectively), for an average $S = 1.625$.

The stoichiometric compound undergoes various phase transitions. The kink in the inverse susceptibility at $T_S = 313$ K is the result of a first-order structural transition to orthorhombic symmetry.[19] The structural transition relieves the magnetic frustration and there is long-range magnetic order at low temperatures for stoichiometric $YBaCo_4O_7$. Magnetic neutron scattering data by Khalyavin et al.[27] (see Fig. 2.5) show that there is a transition at $T_1 \sim 100$ K to long-range order with ordering wavevector $\boldsymbol{q} = 0$, and the symmetry is further broken from orthorhombic to monoclinic. A spin reorientation transition at $T_2 \sim 60$ K does not involve additional symmetry breaking, and diffuse magnetic scattering persists even down to 2 K.

In contrast, oxygen-rich samples avoid a structural transition. Single-phase samples of $YBaCo_4O_{7+\delta}$ with $\delta > 0.08$ have a trigonal structure down to 6 K.[21] Yuan et al. report

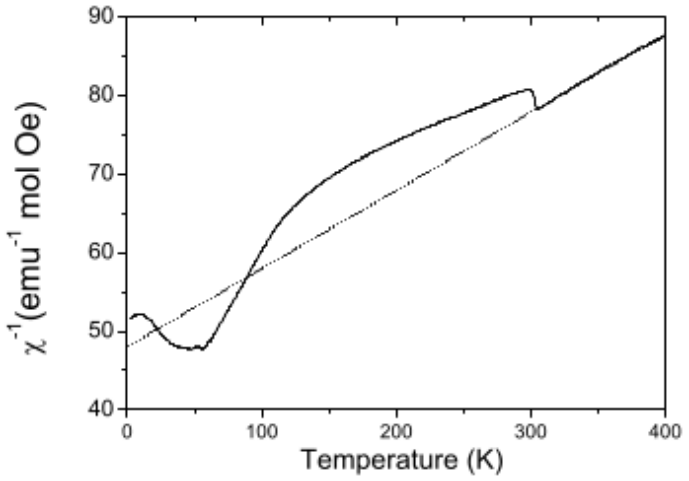


Figure 2.4: Reciprocal susceptibility for a stoichiometric $YBaCo_4O_{7.0}$ powder sample at 1000 Oe. The dotted line fit to a Curie-Weiss law gives $\theta_{CW} = -508$ K and an effective magnetic moment per formula unit of $8.9\,\mu_B$. Taken from Ref. [19].

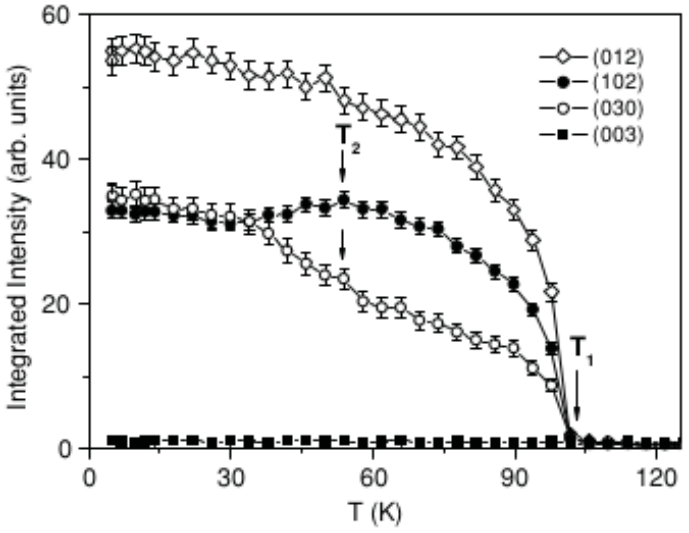


Figure 2.5: Integrated intensities of selected peaks from single-crystal neutron diffraction on stoichiometric $YBaCo_4O_{7.0}$, showing magnetic phase transitions. The indexation is relative to the orthorhombic ($Pbn2_1$) unit cell. Taken from Ref. [27].

based on susceptibility measurements and zero applied field nuclear magnetic resonance (NMR) experiments that $YBaCo_4O_{7.1}$ undergoes some form of spin ordering at $T^* = 80$ K. They argue that the spins undergo sequential freezing-out: first in the triangular layers then at lower temperatures in the kagome layers.[49]

2.1.4 Charge ordering

For stoichiometric $YBaCo_4O_7$, the Co^{2+} and Co^{3+} ions are in a 3:1 ratio, which is the same ratio of kagome to triangular sites. The question naturally arises as to whether these different ions are ordered in a certain way in the crystal.

Valldor and Andersson argue that the absence of symmetry-breaking suggests that Co^{2+} and Co^{3+} are randomly distributed on the kagome lattice sites, with the triangular lattice sites containing Co^{2+} and Co^{3+} in any ratio.[17] There is some structural evidence, based on the shorter average Co-O bond lengths,[†] for a higher mean valence and thus higher ratio of Co^{3+} on triangular lattice sites as compared to kagome lattice sites.[17,22] This argument weakly favours partial charge ordering.

However, a study on isostructural $YbBaCo_4O_7$ by Huq et al. casts doubt on the (already weak) charge ordering hypothesis proposed. For $YbBaCo_4O_7$, the average Co-O bond lengths for triangular and kagome sites are respectively 1.959(3) Å and 1.918(3) Å, i.e., longer instead for the triangular sites.[24] The Co-O bond length is expected to be much shorter, about 1.79 Å, if the triangular sites are all Co^{3+}. A bond valence analysis gives 89.9% Co^{2+}, 10.1% Co^{3+} for the triangular lattice sites, while kagome lattice sites have 70.0% Co^{2+}, 30.0% Co^{3+}, which gives a higher valence on the *kagome* sites instead.[24]

To further complicate matters, there is a structural phase transition for $YbBaCo_4O_7$ at 175 K, which is related to a structural instability evidenced by the long Ba-O distances (averaging 3.13 Å) that indicate that Ba^{2+} is severely underbonded.[24] Below the transition temperature at 150 K, a similar bond valence analysis shows that Co^{2+}/Co^{3+} are essentially randomly distributed over all the cobalt sites. The kagome CoO_4 tetrahedra are buckled and Co-Co contacts are of unequal length.[24]

This question of charge ordering is a tricky one, which might be further complicated

[†]The average Co-O bond lengths for triangular and kagome sites are 1.898(6) Å and 1.921(7) Å respectively.[17]

for oxygen-rich samples. We introduce an additional parameter in our model by assuming that all kagome layer spins have (effective) spin S_k, and that all triangular layer spins have (effective) spin S_t. We define the parameter

$$\sigma \equiv \frac{S_t}{S_k} \tag{2.1}$$

to use in the classical Heisenberg Hamiltonian Eq. (2.3).

2.2 Theoretical model of Heisenberg spins

We adopt the isotropic Heisenberg model to describe magnetism in the extended kagome compounds identified in Section 2.1.1. We assume full spin rotation symmetry for the system, as we expect any magnetic anisotropy to be small. We discuss this point in greater detail in Section 2.2.1. We follow previous authors [20,38,47,50] in using such a description.

Defining the parameter $\alpha \equiv J_2/J_1$ as the ratio of the out-of-plane to the in-plane exchange coupling, the Hamiltonian Eq. (1.3) we use for Heisenberg spins on the extended kagome lattice is

$$\hat{\mathcal{H}} = J_1 \left(\sum_{\langle ij \rangle} \hat{\boldsymbol{S}}_i \cdot \hat{\boldsymbol{S}}_j + \alpha \sum_{[ij]} \hat{\boldsymbol{S}}_i \cdot \hat{\boldsymbol{S}}_j \right) , \tag{2.2}$$

where $\langle ij \rangle$ denotes pairs of nearest-neighbour kagome layer spins (in the same triangle/bipyramid) and $[ij]$ denotes pairs of nearest-neighbour spins, of which one is a kagome layer spin and the other is a triangular layer spin (in the same bipyramid). As discussed in Section 2.1.3, the magnetic ions in the extended kagome compounds such as $YBaCo_4O_7$ are generally in the high-spin state. In the classical approximation, we write $\boldsymbol{S}_i = S_i \boldsymbol{n}_i$, where the spin $S_i \gg 1$ and $\boldsymbol{n}_i$ is an $O(3)$ unit vector. Using the parameter σ defined in Eq. (2.1) as the ratio of the spin on triangular and kagome sites, the classical Hamiltonian is

$$\mathcal{H} = J_1 S_k^2 \left(\sum_{\langle ij \rangle} \boldsymbol{n}_i \cdot \boldsymbol{n}_j + \alpha\sigma \sum_{[ij]} \boldsymbol{n}_i \cdot \boldsymbol{n}_j \right) . \tag{2.3}$$

We shall find it convenient at times to use a matrix representation of the Hamiltonian, writing Eq. (2.2) as

$$\hat{\mathcal{H}} = \tfrac{1}{2} J_1 \sum_{i,j} A_{ij}(\alpha)\, \hat{\boldsymbol{S}}_i \cdot \hat{\boldsymbol{S}}_j . \tag{2.4}$$

The *interaction matrix* for the lattice sites is defined as

$$A_{ij}(\alpha) \equiv A_{ij}^{(1)} + \alpha A_{ij}^{(2)} \ , \tag{2.5}$$

where the *adjacency matrices* are

$$A_{ij}^{(1)} = \begin{cases} 1 & \text{for } ij \in \langle ij \rangle \text{ (within layers)} \\ 0 & \text{otherwise,} \end{cases}$$

and

$$A_{ij}^{(2)} = \begin{cases} 1 & \text{for } ij \in [ij] \text{ (between layers)} \\ 0 & \text{otherwise.} \end{cases}$$

The classical Hamiltonian Eq. (2.3) can similarly be written as

$$\mathcal{H} = \tfrac{1}{2} J_1 S_k^2 \sum_{i,j} A_{ij}(\alpha\sigma)\, \boldsymbol{n}_i \cdot \boldsymbol{n}_j \ . \tag{2.6}$$

2.2.1 Single-ion anisotropy

Magnetic anisotropy that introduces a term of the form

$$\mathcal{H}_{\text{single-ion}} \propto \sum_i (S_i^z)^2 \tag{2.7}$$

in the Hamiltonian would break the spin rotation symmetry of the Heisenberg model. Such terms could arise in $YBaCo_4O_7$ from a spatial anisotropy of the electrostatic potential around the cobalt ions, affecting the orbital magnetic moment or the spin magnetic moment through spin-orbit coupling.

The evidence points towards small anisotropy values. An experimental and theoretical x-ray absorption spectroscopy study of $YBaCo_4O_7$ by Hollmann et al. calculated a small value of $0.5\,\mu_B$ for the orbital angular momentum of the Co^{2+} ions.[39] They argue that as the CoO_4 tetrahedra are almost regular, spin-orbit effects will not lead to a large magnetic anisotropy for the Co^{2+} ions.[39] Spin-orbit interactions in the tetrahedral crystal field of the Co^{3+} ions are expected to cause rather small energy splitting.[39]

We can also make a more qualitative argument for why the magnetic anisotropy is small. The point-group symmetry of a regular tetrahedron does not pick out a unique axis in space. As the immediate environment of the Co sites is an oxygen tetrahedron, the selection of the

interlayer direction as the z-direction in Eq. (2.7) can only come from distortions or further neighbour electrostatic interactions, both of which are likely to make any anisotropy small. Khalyavin et al. measured the magnetisation for a $YBaCo_4O_7$ single crystal (see Fig. 2.6), and the agreement of the curves for applied fields in different directions provides further experimental evidence that the magnetic anisotropy is small.

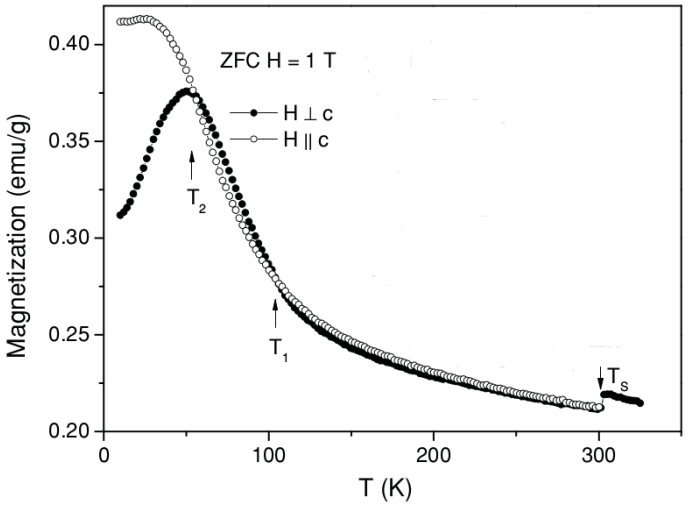


Figure 2.6: Magnetisation measurements for single-crystal stoichiometric $YBaCo_4O_{7.0}$, with applied field parallel and perpendicular to the $\boldsymbol{c}$-axis. The two curves agree very well above T_2. Taken from Ref. [27].

2.2.2 Ground state contraints for classical spins

We can work out the ground states of the classical Heisenberg model Eq. (2.3) by building up the lattice from bipyramids and triangles.[20,47] We will follow the treatment in Khalyavin et al.[47] but discuss the steps in a more leisurely way.

The idea is to first find the ground states for an isolated bipyramid. Then, we assemble a kagome layer using bipyramids in their ground state and also minimising the energy of the bonds on the uncapped triangles that connect the bipyramids. We then stack kagome layers together by joining them at the apices of the bipyramids, to get the full lattice. In this way, we can account for all bonds exactly once (each bond either belongs to a single bipyramid or to a single uncapped triangle in a kagome plane).

We consider a single bipyramid, numbering the kagome lattice spins 1 through 3 and

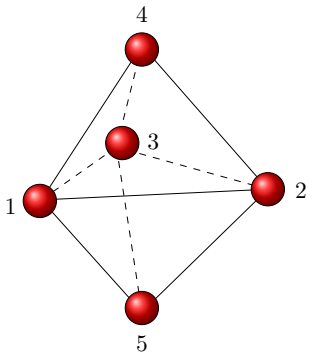


Figure 2.7: Numbering convention for the spins in a bipyramid.

the apical spins 4 and 5 (see Fig. 2.7). The classical spin energy is

$$E = J_1 S_k^2 \Big((\boldsymbol{n}_1 \cdot \boldsymbol{n}_2 + \boldsymbol{n}_2 \cdot \boldsymbol{n}_3 + \boldsymbol{n}_1 \cdot \boldsymbol{n}_3) + \alpha\sigma \big[\boldsymbol{n}_4 \cdot (\boldsymbol{n}_1 + \boldsymbol{n}_2 + \boldsymbol{n}_3) + \boldsymbol{n}_5 \cdot (\boldsymbol{n}_1 + \boldsymbol{n}_2 + \boldsymbol{n}_3) \big] \Big) ,$$

which can be written as

$$\frac{E}{J_1 S_k^2} = \tfrac{1}{2}(\boldsymbol{n}_1 + \boldsymbol{n}_2 + \boldsymbol{n}_3)^2 - \tfrac{1}{2}(\boldsymbol{n}_1^2 + \boldsymbol{n}_2^2 + \boldsymbol{n}_3^2) + \alpha\sigma(\boldsymbol{n}_4 + \boldsymbol{n}_5) \cdot (\boldsymbol{n}_1 + \boldsymbol{n}_2 + \boldsymbol{n}_3) .$$

It is natural to define

$$\begin{cases} \boldsymbol{u} \equiv \boldsymbol{n}_1 + \boldsymbol{n}_2 + \boldsymbol{n}_3 \\ \boldsymbol{v} \equiv \alpha\sigma(\boldsymbol{n}_4 + \boldsymbol{n}_5) \end{cases} \tag{2.8}$$

for the kagome and apical spins respectively. Completing the square,

$$\frac{E}{J_1 S_k^2} = \tfrac{1}{2} \left((\boldsymbol{u} + \boldsymbol{v})^2 - \boldsymbol{v}^2 \right) + C , \tag{2.9}$$

where C is a constant.

A ground state of the bipyramid is obtained by minimising the function

$$\epsilon \equiv (\boldsymbol{u} + \boldsymbol{v})^2 - \boldsymbol{v}^2 , \tag{2.10}$$

subject to the constraints on the length of the vectors

$$\begin{cases} 0 \leq u \equiv |\boldsymbol{u}| \leq 3 \\ 0 \leq v \equiv |\boldsymbol{v}| \leq 2\alpha\sigma . \end{cases}$$

To minimise the $(\boldsymbol{u}+\boldsymbol{v})^2$ term in Eq. (2.10), $\boldsymbol{u}$ and $\boldsymbol{v}$ should be anti-parallel. In this case, the function ϵ depends only on the magnitudes u and v, and we write

$$\epsilon = (u-v)^2 - v^2 \, .$$

Setting $\partial\epsilon/\partial v = 0$ gives $u = 0$, which means that ϵ is extremised when $u = 0$, or when v is at a limiting value. As $\epsilon = 0$ when $u = 0$, and $\epsilon = u^2 \geq 0$ when $v = 0$, we conclude that the minimum of ϵ occurs at the other limiting value of v, when $v = 2\alpha\sigma$ (i.e., when the apical spins are parallel), since we can always find a value of $0 < u \leq 3$ such that

$$\epsilon = (u - 2\alpha\sigma)^2 - (2\alpha\sigma)^2 < 0 \, . \tag{2.11}$$

This means that the antiferromagnetic interactions between spins in a bipyramid result in ground states with an *effective ferromagnetic correlation* between the two apical spins.

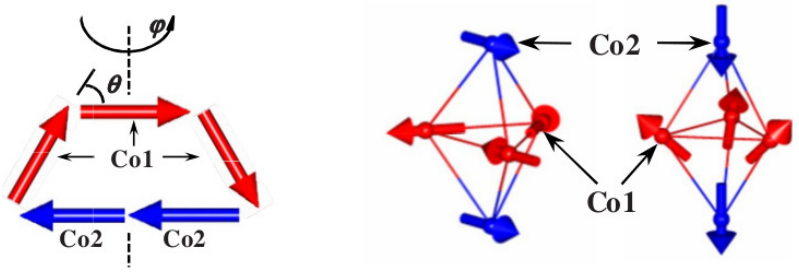


Figure 2.8: Ground state spin configurations for a bipyramid, with $\alpha\sigma = 1$. The kagome (apical) spins are coloured red (blue). The internal degrees of freedom parameterising the ground states are the angles θ and φ; the first defines angles between spins in the planar geometry, the second takes the apical spins out of the planar configuration. The right panel shows some possible ground states. Taken from Ref. [47].

From Eq. (2.11) it is clear that u should be as close as possible to $2\alpha\sigma$ in order to minimise the $(u-2\alpha\sigma)^2$ term. For $\alpha\sigma < \frac{3}{2}$, we can always arrange the kagome lattice spins so that $u = 2\alpha\sigma$. For $\alpha\sigma \geq \frac{3}{2}$, the three kagome spins will be aligned so that u takes the maximum value of 3. In terms of the classical spin vectors, the ground state constraints for a bipyramid are

$$\begin{cases} \boldsymbol{n}_4 = \boldsymbol{n}_5 \equiv \boldsymbol{n}^{(a)} \\ \boldsymbol{n}_1 + \boldsymbol{n}_2 + \boldsymbol{n}_3 + 2\mathcal{A}\boldsymbol{n}^{(a)} = 0 \, . \end{cases} \tag{2.12}$$

The second condition in Eq. (2.12) is a *sum rule*, with the apical spins each scaled by $\mathcal{A} = \min\{\alpha\sigma, \frac{3}{2}\}$. These constraints leave two continuous internal degrees of freedom for

the kagome lattice spins when $\alpha\sigma < \frac{3}{2}$, which can be parameterised by the angles θ, φ as shown in Fig. 2.8. The spins in a bipyramid are collinear in the ground states for $\alpha\sigma \geq \frac{3}{2}$.

The next step is to find ground states of a kagome layer by also minimising the energy of the uncapped triangles. For three spins around a triangle, mutually interconnected with identical exchange couplings, the interaction energy is proportional to the square of the sum of the spins, up to a constant term. The minimum energy is thus obtained when the spins around the triangle sum to zero, meaning that the three spins are coplanar and mutually at an angle of 120°. A ground state spin configuration for the system satisfies these conditions for the bipyramids and triangles in each layer. As the bipyramids form columns of apical spins, the first condition in Eq. (2.12) imposes *ferromagnetic correlations* along each column.

2.2.3 Experimental and numerical evidence

We have seen how the ground state constraints for the classical Hamiltonian Eq. (2.3) introduce *quasi-one-dimensional order* for the triangular lattice spins in the interlayer direction. At the same time, we expect spin correlations within the layers to be *disordered* for $\alpha\sigma < \frac{3}{2}$.

These conclusions are supported by elastic magnetic neutron scattering data and the results of direct Monte Carlo simulations.[20,47] The experiments reported by Manuel et al. were performed on single-crystal stoichiometric $YBaCo_4O_7$ at $T = 130$ K, which is in the frustrated regime above the transition temperature $T_c \sim 100$ K and below the Curie-Weiss temperature $|\theta_{CW}| \sim 500$ K.[20] The calculated structure factor from Monte Carlo simulations of classical Heisenberg spins, with $\alpha = 1$ and $\sigma = 1$, produces excellent agreement with the patterns obtained from experiments (see Fig. 2.9). In the $(0kl)$-plane, the isolated diffuse spots of high intensity have sharper features in the $\boldsymbol{c}^*$ direction than along $\boldsymbol{b}^*$, indicating much longer correlations along the apical spin columns than within the kagome layers.

The static spin correlations in the low temperature Monte Carlo configurations illustrate the marked difference between the apical spin columns and the kagome planes (see Fig. 2.10). While there are 98% correlations at the ninth neighbour for the apical sites along a bipyramidal column, the in-plane spin correlations for the kagome sites are reminiscent

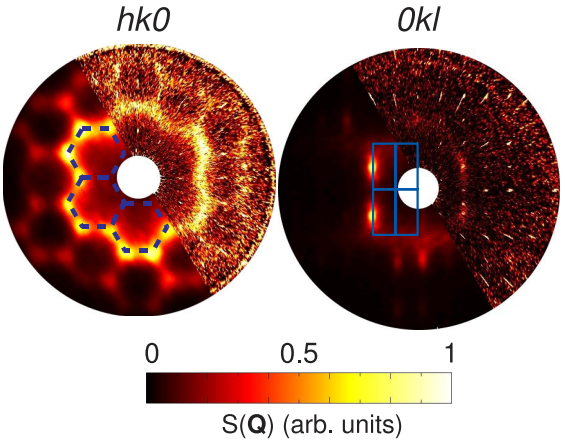


Figure 2.9: Magnetic diffuse scattering patterns in reciprocal space for stoichiometric $YBaCo_4O_7$ single-crystal, with planes indexed using a hexagonal lattice system. For the $(0kl)$-plane shown on the right, the k-direction is vertical and the l-direction is horizontal. The intensity of the scattering cross-section in each plane is obtained from Monte Carlo simulations (lower left half) and from experimental neutron scattering (upper right half). Taken from Ref. [20].

of a 120° configuration with a periodicity of 3 sites, and a decay to 25% at the ninth neighbour.[20]

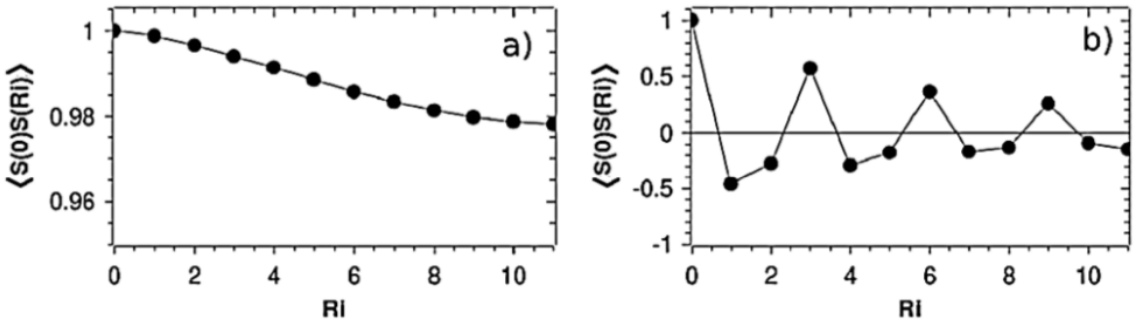


Figure 2.10: Static spin correlations from low temperature Monte Carlo for (a) apical spin sites along a column, and (b) kagome spin sites within a plane. Taken from Ref. [20].

There are reports of other materials also being well-modelled by the classical Heisenberg Hamiltonian Eq. (2.3). Valldor et al.[38] found that the magnetic neutron scattering pattern from a $YBaCo_3FeO_7$ powder sample was reproduced by Monte Carlo simulations with $\alpha = \frac{1}{2}$ and $\sigma = 1$ (see Fig. 2.11).

More controversially, there were claims by Schweika et al.[25] that the partially-substituted compound $Y_{0.5}Ca_{0.5}BaCo_4O_7$ realised a classical 2D kagome system with $\alpha\sigma = 0$. Stewart et al.[28] contested this claim, explaining that Schweika et al. missed out an important part of the wide dynamic range of magnetic fluctuations because they had used cold neutrons. Stewart et al. argued instead that Ca-doping resulted in magnetic exchange disorder that

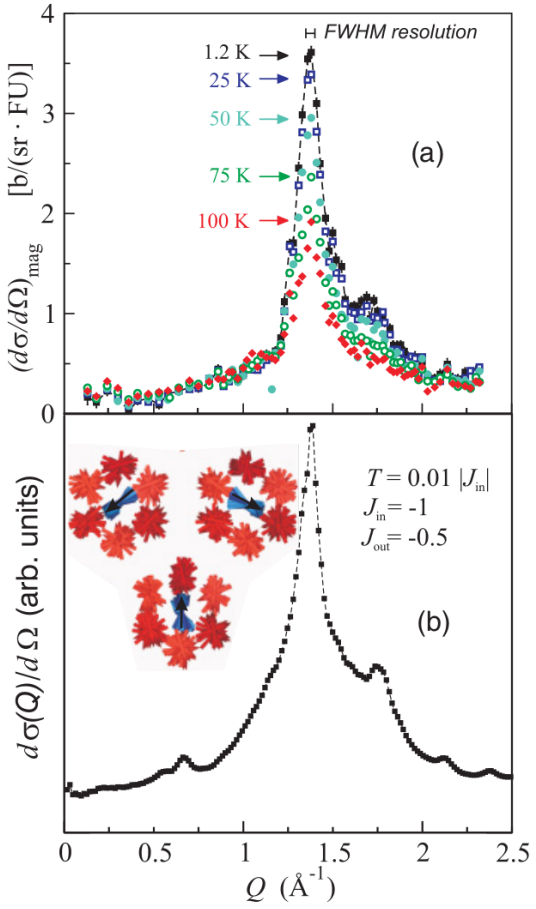


Figure 2.11: (a) Intensity of magnetic neutron scattering as a function of wave-vector Q and temperature T for a $YBaCo_3FeO_7$ powder sample. The finite widths of the peaks indicate short-range correlations rather than 3D ordering at low temperatures. (b) Monte Carlo simulations for a classical Heisenberg model with $\alpha = \frac{1}{2}$ and $\sigma = 1$. The scattering intensities were calculated using site occupancies determined from Mössbauer spectroscopy with $S = \frac{3}{2}$ for cobalt and $S = \frac{5}{2}$ for iron. The inset shows a projection of the spin arrangements along the $\boldsymbol{c}$-direction (perpendicular to the kagome planes). The triangular lattice spins (blue) show 1D ordering along $\boldsymbol{c}$ and local 120° angles in-plane. The kagome lattice spins (red) are less ordered along $\boldsymbol{c}$ and their projection does not show a clear pattern. Taken from Ref. [38].

was responsible for the lack of long-range order.[28]

CHAPTER 3

Ground states and order by disorder

> The world is full of magic things, patiently waiting for our senses to grow sharper.
>
> — *William B. Yeats*

To set the stage for the rest of the thesis, it is worth reviewing the reasons for our interest in the extended kagome lattice, and the kinds of questions we might want to answer. In connection with experiment, when I started work on my thesis in 2011, $YBaCo_4O_7$ was the only geometrically frustrated magnet for which single-crystal inelastic neutron scattering results were available. Since then, results on herbertsmithite[†] and $MgCr_2O_4$[‡] have been published.[51,52] From a theoretical viewpoint, the extended kagome lattice is unusual because of both the long correlation length for the apical spin columns and the apparently short correlation length within the planes. The long-range one-dimensional correlations could have interesting implications for the spin dynamics, which we expect to be very slow at low temperatures.

In this chapter, we will address several questions related to ground states of the Heisenberg antiferromagnet on the extended kagome lattice. We describe the classical ground states in Section 3.1.1 using the flux picture for a single layer of spins, and derive a perimeter bound for the sum of triangular lattice spins in a given area. In Section 3.1.2, we quantify the classical ground state degeneracy using a Maxwell counting argument for the number of continuous degrees of freedom. We attempt to answer the question of whether the classical ground state manifold is connected. Simulations of small spin clusters in Section 3.1.3 give us some ideas, but are not conclusive. We discuss topological defects in Section 3.1.4, also motivated by this question of connectedness, but are again inconclusive on this point because the ground state manifold may only contain one of the topological sectors. We explore spin correlations by studying numerical ground states in Section 3.1.5.

[†]Chemical formula $ZnCu_3(OD)_6Cl_2$, which realises a kagome lattice Heisenberg antiferromagnet of Cu^{2+} spins ($S = \frac{1}{2}$) with lattice planes separated by non-magnetic Zn^{2+} ions.

[‡]The Cr^{3+} spins ($S = \frac{3}{2}$) form a pyrochlore lattice Heisenberg antiferromagnet.

Finally, we are interested to know if the system undergoes order by disorder. We review the answer provided by Buhrandt and Fritz[50] in Section 3.2.

3.1 Classical ground states

For subsequent reference, we calculate the theoretical ground state energy per spin for the classical Hamiltonian Eq. (2.3). Following the argument in Section 2.2.2 about energy minimisation, the ground state energy E_B for the bonds in a single bipyramid is

$$\frac{E_B}{J_1 S_k^2} = \begin{cases} -\frac{3}{2} - 2(\alpha\sigma)^2 & \text{for } \alpha\sigma < \frac{3}{2} \\ 3 - 6\alpha\sigma & \text{for } \alpha\sigma \geq \frac{3}{2} \end{cases},$$

and the ground state energy E_T for the bonds in a single uncapped triangle is

$$\frac{E_T}{J_1 S_k^2} = -\frac{3}{2}\,.$$

As there is one bipyramid for every four spins, and one uncapped triangle for each bipyramid, the ground state energy per spin E_0 is

$$\frac{E_0}{J_1 S_k^2} = \tfrac{1}{4}(E_B + E_T)/J_1 S_k^2 = \begin{cases} -\frac{3}{4} - \frac{1}{2}(\alpha\sigma)^2 & \text{for } \alpha\sigma < \frac{3}{2} \\ \frac{3}{8} - \frac{3}{2}\alpha\sigma & \text{for } \alpha\sigma \geq \frac{3}{2} \end{cases}. \tag{3.1}$$

3.1.1 Flux picture for a kagome layer

We saw in Section 2.2.2 that in classical ground states, the triangular lattice spins are perfectly correlated between layers. As a result, the kagome spins in each layer "experience" the same neighbouring triangular lattice spin configuration. To describe the classical ground states, we thus consider just a single kagome layer with unit spins, sandwiched on both sides by some triangular lattice spin configuration. We derive a *flux picture*, in which the triangular lattice spins inject a flux into the bipyramids.

In Fig. 3.1, we show a single kagome lattice layer, where the shaded triangles represent bipyramids with apical spins above and below the triangle centres. Depicted in red is the honeycomb lattice, which is the simplex lattice to the kagome. The spins at the vertices of the kagome lattice lie on the *bonds* of the honeycomb lattice. The vertices of the bipartite honeycomb lattice correspond to the shaded and unshaded triangles in the kagome plane,

which represent bipyramids (B) and uncapped triangles (T) respectively. We shall therefore term the two types of vertices for the honeycomb lattice as B-sites (shaded) and T-sites (unshaded) respectively.

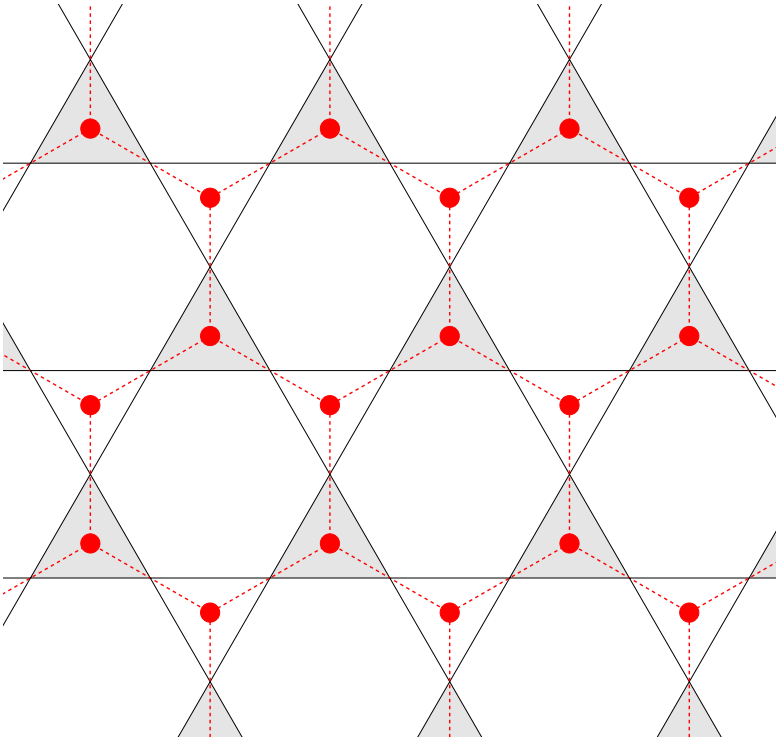


Figure 3.1: Kagome and honeycomb lattices. The honeycomb lattice (in red) is the simplex lattice. The two inequivalent sites of the bipartite honeycomb lattice correspond to the shaded (B) and unshaded (T) kagome triangles, representing bipyramids and uncapped triangles respectively. Kagome spins lie on the bonds of the honeycomb lattice.

The ground state constraints discussed in Section 2.2.2 lead to two different sum rules for the spins on the vertices of the shaded and unshaded triangles. For the shaded triangles (bipyramids), we know from Eq. (2.12) that the spins must sum to $-2\mathcal{A}\boldsymbol{n}^{(a)}$, where $\mathcal{A} = \min\{\alpha\sigma, \frac{3}{2}\}$ and $\boldsymbol{n}^{(a)}$ is the apical spin vector. For the unshaded triangles (uncapped triangles), the spins must sum to zero. These rules are readily translated into a flux description. As the honeycomb lattice is bipartite, we can consider *directed bonds* from the T to B sublattice. Any spin configuration on the kagome lattice can unambiguously define a mapping to a configuration of fluxes on the directed bonds of the honeycomb lattice. We can achieve this by setting the flux on each bond to be equal to the spin vector that sits on that bond, i.e.,

$$\boldsymbol{F}_{\langle\tau\beta\rangle} \equiv \boldsymbol{n}_{\tau\beta} \ , \tag{3.2}$$

where $\boldsymbol{F}_{\langle\tau\beta\rangle}$ is the flux variable for the directed bond between nearest neighbour honeycomb sites $\tau \in \{T\}$ and $\beta \in \{B\}$, and $\boldsymbol{n}_{\tau\beta}$ is the unit vector for the kagome spin that is shared by the unshaded and shaded triangles represented by τ and β respectively. We see that the ground state constraints translate to a net flux of $-2\mathcal{A}\boldsymbol{n}^{(a)}$ entering a B-site and a net flux of zero at T-sites, i.e.,

$$\begin{cases} \boldsymbol{F}_\beta \equiv \sum\limits_{\tau\in\{T\}} \boldsymbol{F}_{\langle\tau\beta\rangle} = -2\mathcal{A}\boldsymbol{n}_\beta^{(a)} \\ \boldsymbol{F}_\tau \equiv \sum\limits_{\beta\in\{B\}} \boldsymbol{F}_{\langle\tau\beta\rangle} = 0 \,, \end{cases} \tag{3.3}$$

where $\boldsymbol{n}_\beta^{(a)}$ refers to the apical spin vector for the shaded triangle $\beta \in \{B\}$.

For classical ground states, we see that the total moment of the apical spins within a given area is *bounded by its perimeter*, since the net flux in an area must enter or leave via the kagome spins on the perimeter. If we consider (theoretical) systems with periodic boundary conditions, these have zero net magnetisation in ground states because the apical spins must sum to zero. In this case, taking the sum over all sites gives

$$\sum_{\beta\in\{B\}} \boldsymbol{F}_\beta = \sum_{\tau\in\{T\}} \boldsymbol{F}_\tau = 0 \tag{3.4}$$

since the total flux entering the B-sites is the total flux leaving the T-sites. The total moment of the kagome and apical spins separately sum to zero.

3.1.2 Ground state dimension

The ground state constraints Eq. (2.12) allow the spins in a bipyramid to retain some internal degrees of freedom, provided the interlayer coupling is not too strong, i.e., $\alpha\sigma < \frac{3}{2}$. In this subsection, we will show that the dimension of the ground state manifold[†] is divergent but sub-extensive.

We use a Maxwellian counting argument[53,54] to estimate the ground state dimension

$$D = F - K \tag{3.5}$$

by subtracting the number of ground state constraints K from the total number of degrees

[†]The ground state dimension is defined as the number of *continuous* degrees of freedom within the manifold of ground states.

of freedom F in the system. We note that while Maxwellian counting correctly yields an extensive D for classical Heisenberg spins on the pyrochlore lattice, the calculation incorrectly gives $D = 0$ on the kagome lattice.[13,14] In general, the counting argument can go wrong in two ways. First, if the ground states are not properly characterised, the ground state constraints identified might be incompatible. Second, as happens for the kagome lattice, the counting argument underestimates D if the ground state constraints are not linearly independent. The correct result for the kagome lattice is obtained by explicit construction of sets of coplanar spin states, for which D is extensive.[15,16]

The process of working through the counting argument is similar to how we build up ground states in Section 2.2.2. We will assemble the full lattice by first considering bipyramids and triangles in a layer. For $O(n)$ classical spins, each spin has $n-1$ degrees of freedom, so

$$F_{unit} = q(n-1) \tag{3.6}$$

for a set of q spins. For a single bipyramidal unit of classical Heisenberg spins, $n = 3$ and $q = 5$, so we have $F_{unit} = 10$. For $\alpha\sigma < \frac{3}{2}$, we have $K_{unit} = 5$ and thus $D_{unit} = 5$. Two of the constraints come from aligning the apical spins, and the other three from the sum rule in Eq. (2.12). Since these ground state spin configurations are not collinear, three of the five continuous degrees of freedom correspond to global spin rotation, with two internal degrees of freedom left over. As $\alpha\sigma$ increases, the allowed ranges for the internal degrees of freedom are reduced. For $\alpha\sigma \geq \frac{3}{2}$, all five spins are collinear in ground states, and we have $K_{unit} = 8$ and $D_{unit} = 2$. Both these degrees of freedom correspond to global spin rotation of the collinear spins.[†]

We now account for the arrangement of bipyramids and uncapped triangles in each layer. Let N_C be the number of bipyramids in a single layer, which is the number of apical spin columns in the full lattice. These bipyramids are connected with an equal number of uncapped triangles in each layer. We argued in Section 2.2.2 that the spins on each kagome triangle should sum to zero in ground states, which for 3-component spins results

[†]There are only two (and not three) degrees of freedom for global spin rotation in this case as the spins all share a common axis.

in $3N_C$ additional constraints for each layer. For a single layer, we thus have

$$D_{layer} = \begin{cases} 2N_C & \text{for } \alpha\sigma < \frac{3}{2} \\ -N_C & \text{for } \alpha\sigma \geq \frac{3}{2} \end{cases} . \tag{3.7}$$

As there are N_C aligned apical spin pairs in each layer, Eq. (3.7) for $\alpha\sigma < \frac{3}{2}$ suggests that the apical spin pairs in the bipyramids can be *oriented independently* while staying in the ground state manifold. The extent of this freedom to independently reorient spins is expected to be larger for smaller $\alpha\sigma$. Note that for $\alpha\sigma \geq \frac{3}{2}$, the calculation that $D_{layer} < 0$ indicates that the ground state constraints imposed are not linearly independent. We can see this explicitly as the ground state for this case is a coplanar ground state, with the collinear spins in each bipyramid satisfying the 120° rule on each uncapped triangle. This coplanar state is *unique up to global spin rotation* and the correct result is $D_{layer} = 0$ for $\alpha\sigma \geq \frac{3}{2}$.

In the full lattice, apical spins in each column are all aligned and there are no added degrees of freedom from additional layers. The final result is simply

$$D = \begin{cases} 2N_C & \text{for } \alpha\sigma < \frac{3}{2} \\ 0 & \text{for } \alpha\sigma \geq \frac{3}{2} \end{cases} . \tag{3.8}$$

The number of ground state degrees of freedom is divergent, proportional to the *area of the layers*, but sub-extensive. We have to make a correction to Eq. (3.8) for finite-size systems with periodic boundary conditions imposed. Consider such a system with N_C bipyramidal columns with N_L kagome layers (and thus N_L triangular lattice layers). We can choose the orientations of the N_C columns of apical spins freely, except for 3 additional constraints because we require the apical spins to sum to zero in accordance with Eq. (3.4) from the flux picture. This gives $2N_C - 3$ degrees of freedom so far. Now consider the spins in a kagome layer. There are $3N_C$ spins and thus $F = 6N_C$ degrees of freedom for them, while the sum rule for each of the N_C bipyramids and N_C uncapped triangles imposes a total of $K = 6N_C$ constraints. However, this overcounts the constraints by 3, since if we impose the sum rule for all but one triangle, we know from the flux picture that the flux at the last honeycomb lattice site is fixed and the sum rule on that last triangle is automatically

satisfied. Each kagome layer thus adds 3 degrees of freedom, and for $\alpha\sigma < \frac{3}{2}$ we have

$$D_{pbc} = 2N_C - 3 + 3N_L \ . \tag{3.9}$$

3.1.3 Simulations of small spin clusters

It would be interesting to know if the classical ground state manifold is connected. We saw from Eq. (3.8) that the ground state dimension is consistent with allowing the apical spin columns to be independently oriented. If the ground state manifold is connected, these reorientations can always be done continuously without leaving the ground state manifold.

The idea of this subsection is to numerically investigate the constraints on the apical spins in ground states.† In our simulations, we fix the configuration of apical spins and allow the kagome spins to relax to an energy minimum, repeating this for various apical spin configurations to look for patterns in the energy minima. We realise from the outset that the results from this study will at best be tentative, since we can only study small systems carefully because the degrees of freedom for the apical spins scale as the area of the sample. As such, generalising any patterns that emerge to the thermodynamic limit will not be reliable.

Concretely, the relaxation of kagome spins is achieved in two steps. First, we perform simulated annealing using Metropolis Monte Carlo on the classical Hamiltonian Eq. (2.3), such as described in Ref. [1], sweeping through the kagome spins only, to reach a low temperature of

$$\frac{T}{J_1} = 10^{-3} \ .$$

After that, the kagome spins were repeatedly aligned with their local field, following the algorithm used by Walker and Walstedt for metallic spin glasses.[55,56] This algorithm is guaranteed to reduce the system energy at every iteration, by an amount

$$\Delta E_i = -(1 - \cos\theta_i)|\boldsymbol{H}_i| \ , \tag{3.10}$$

where $\boldsymbol{H}_i$ is the local field of spin $\boldsymbol{S}_i$ that is at an angle θ_i from the spin before alignment.

We consider clusters of 8-site unit cells with periodic boundary conditions. In Fig. 3.2,

†As we study systems with periodic boundary conditions, one constraint we expect from the flux picture is that the apical spins sum to zero.

we show the plan-view of the unit cell and the in-plane hexagonal lattice vectors $\underline{a}$ and $\underline{b}$. The third lattice vector $\underline{c}$ points out of the plane. The sites numbered 1–3 are in one kagome plane with fractional coordinate 0 in the $\underline{c}$ direction. The sites numbered 5–7 are in another kagome plane with fractional coordinate $\frac{1}{2}$, while the sites 4 and 8 are apical spins with with fractional coordinate $\frac{1}{4}$ and $\frac{3}{4}$ respectively.

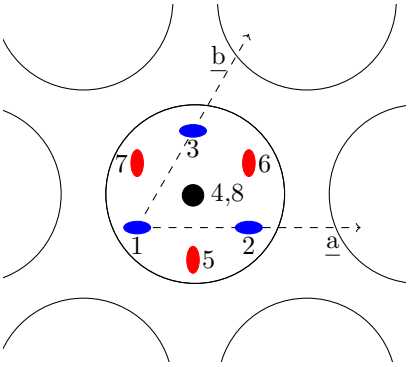


Figure 3.2: The full 8-site unit cell for the extended kagome lattice. Sites 1–3 have fractional coordinate 0 in the $\underline{c}$ direction, sites 5–7 have fractional coordinate $\frac{1}{2}$, and sites 4 and 8 have fractional coordinate $\frac{1}{4}$ and $\frac{3}{4}$ respectively.

We performed simulations for small clusters with the number of bipyramids in a layer $N_C \in \{2, 3, 4\}$, which we will discuss in turn. We set $\sigma = 1$ for the classical Heisenberg spins and just vary α. For each configuration of apical spins, we calculate the minimum energy per spin E_1 obtained from relaxing the kagome spins, and plot

$$E = E_1 - E_0 \ , \tag{3.11}$$

where E_0 is the theoretical ground state energy per spin in Eq. (3.1). These simulations also provide an opportunity to numerically test the flux picture developed in Section 3.1.1. While looking for constraints on the apical spins in ground states, we will check the prediction Eq. (3.4) that the apical spins sum to zero in a system with periodic boundary conditions. Running these simulations with the full 8-site unit cell for the extended kagome lattice provides further assurance that the flux picture for a single kagome layer applies to systems with more than one layer.

We begin with the simplest case of $N_C = 2$, where we varied the relative angle between apical spins in the different bipyramids, through the range $\theta \in [0, \pi]$. For all values of α, $E(\theta)$ is minimum when the apical spins are anti-aligned, i.e., when $\theta = \pi$ (see Fig. 3.3).

Also, $\min[E(\theta)] = 0$ only for $\alpha \lesssim 1$, and not for larger values of α. This might be because the cluster is too small — the ordered ground state for $\alpha \geq \frac{3}{2}$ requires a larger repeating unit for 120° order between the spins in different bipyramids. The numerics for $N_C = 2$ show that the condition from the flux picture that the apical spins sum to zero is *necessary* (but insufficient) to produce a ground state.

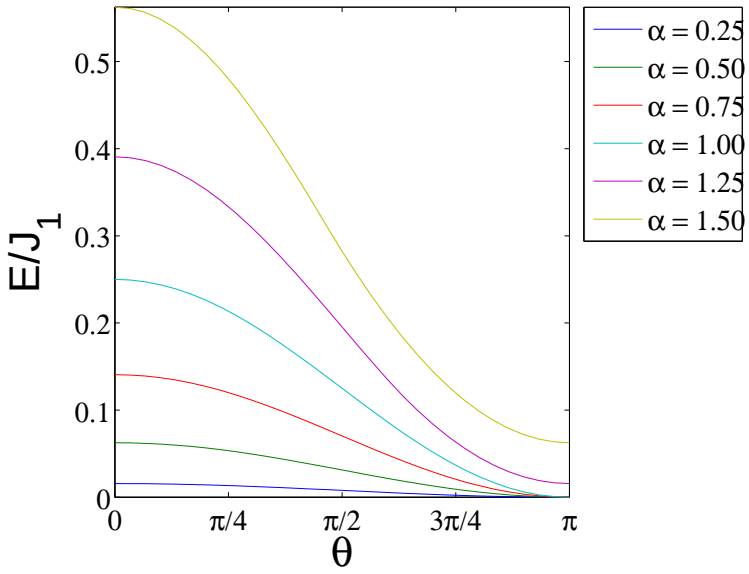


Figure 3.3: Minimum spin cluster energy (per spin) E for $N_C = 2$, as a function of the relative angle θ between the rigidly fixed apical spins. Energy (per spin) is measured relative to the theoretical ground state energy.

For $N_C = 3$, we approached the problem in two stages, using colour plots to visualise E each time (see Fig. 3.4). In the first stage, we kept the three apical spins coplanar, and independently varied the angles θ_1 and θ_2 of the other two spins relative to the first one. These simulations showed clear minima for $E(\theta_1, \theta_2)$ when the apical spins were mutually at 120° angles, as we expect from the flux picture. In the second stage, we kept the first two spins at an 120° angle and rotated the third spin around the surface of a sphere, plotting $E(\theta, \phi)$ as a function of spherical angles.[†] These simulations again confirm Eq. (3.4) from the flux picture. Note that the lowest energy as indicated by the colourbar scales in Fig. 3.4 does not reach zero for $\alpha > 1$, as the periodic boundary conditions used in the simulation do not allow the 120° ordered ground state for $\alpha \geq \frac{3}{2}$.

We now consider the simulations for $N_C = 4$, using the flux picture to justify exploring

[†] In our conventions for the spherical angles, $\theta = 0$ corresponds to the third spin pointing in the z-direction with the other two spins in the xy-plane, and $\phi = 0$ corresponds to the angle where the projection of the third spin onto the xy-plane is at 120° to the other two spins.

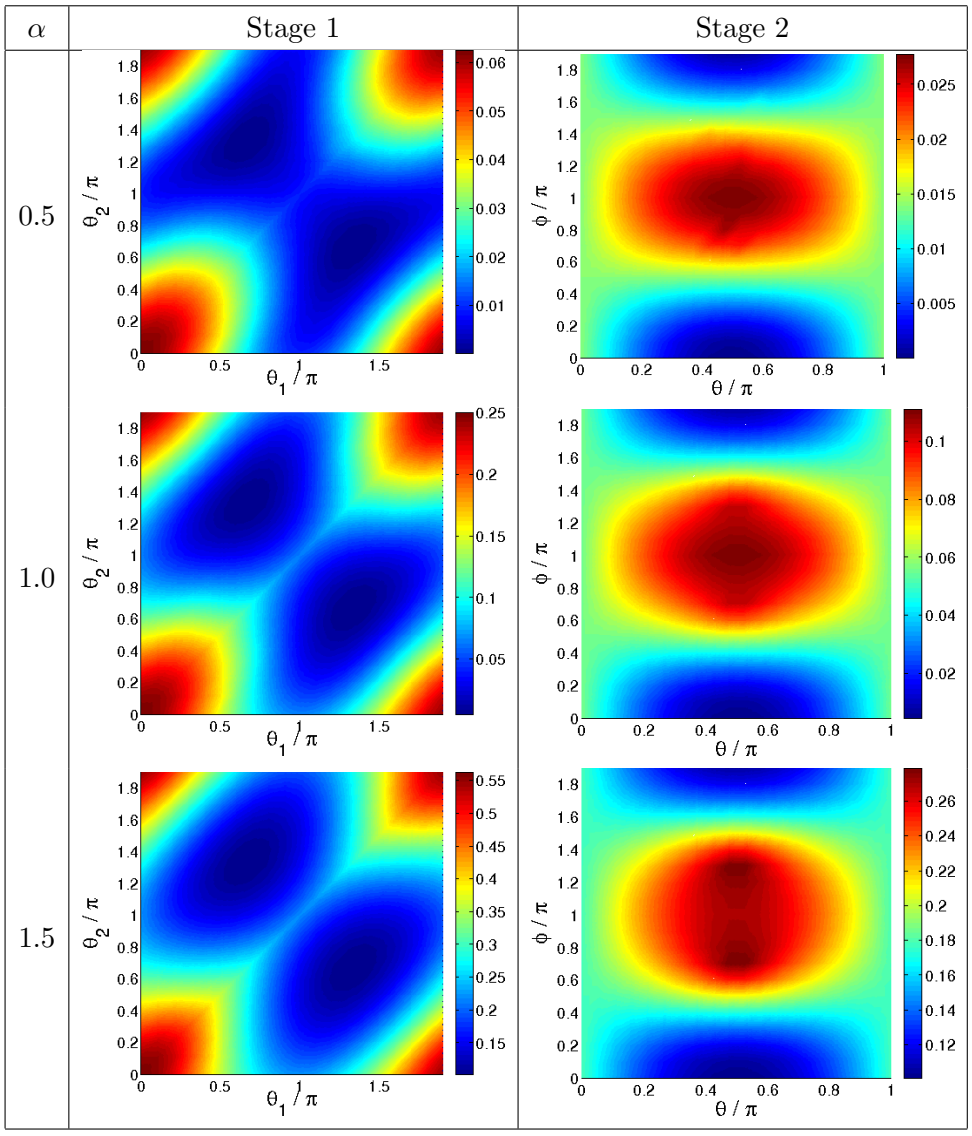


Figure 3.4: Minimum spin cluster energy (per spin) E for $N_C = 3$, measured (in units of J_1) relative to the theoretical ground state energy. For Stage 1, the first apical spin is kept fixed, and (θ_1, θ_2) are the angles of the other two apical spins relative to the first. For Stage 2, two apical spins are fixed at an 120° angle while the other apical spin was swept through all spherical angles (θ, ϕ). In the convention used, $\theta = 0$ corresponds to the third spin pointing in the z-direction with the other two spins in the xy-plane, and $\phi = 0$ corresponds to the angle where the projection of the third spin is at 120° to the other two spins.

only states where the apical spins sum to zero. The vector diagram for the four apical spins to sum to zero is generally a "buckled rhombus" (see Fig. 3.5), and the internal degrees of freedom can be parameterised by a "jaw" angle $\theta \in [0, \pi]$ and a "flapping" angle $\phi \in [0, 2\pi]$. The plots of $E(\theta, \phi)$ are interesting and surprising (see Fig. 3.6). For $\alpha \lesssim 1$, the colourplots are essentially structureless, indicating the lack of additional constraints on the apical spin directions. For $\alpha > 1$, however, configurations with all four apical spins

collinear have systematically higher energy. These correspond to

$$\begin{cases} \theta = \pi \\ \theta = 0 \text{ and } \phi = 0, \pi \ . \end{cases}$$

Additionally, we see as we go down the right column of Fig. 3.6 that the region of parameter space where $E(\theta, \phi)$ is minimised *shrinks* with increasing α. This energy minimum appears to be centred on the symmetrical configurations with each apical spin mutually at the tetrahedral angle of approximately 109.5° to all others, corresponding to the two cases

$$\begin{cases} \theta = \cos^{-1}\left(\frac{1}{3}\right) \approx 0.39\,\pi, \quad \phi = \pi/2 \\ \theta = \cos^{-1}\left(\frac{1}{3}\right) \approx 0.39\,\pi, \quad \phi = 3\pi/2 \ . \end{cases}$$

These apical spin configurations are related by spin inversion.

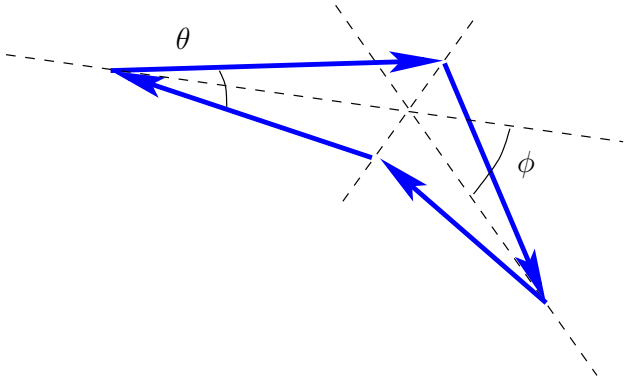


Figure 3.5: Perspective drawing of the "buckled rhombus" of apical spins for $N_C = 4$, depicting the "jaw" angle $\theta \in [0, \pi]$ and the "flapping" angle $\phi \in [0, 2\pi]$ that buckles the rhombus. For example, we get a square for $\theta = \pi/2$ and $\phi = 0$.

We find for $N_C = 4$ that the energetics favour a special subset of apical spin configurations. It is possible that these configurations are separated by energy barriers such that it is not possible to continuously vary (θ, ϕ) to get from one minimum to the other without leaving the ground state manifold. However, we must bear in mind that our numerics sample the continuous degrees of freedom at a finite mesh, and we cannot rule out the very real possibility of small "holes" that connect these ground states. Clearly, more work needs to be done to decide the connectedness of the ground state manifold. These small cluster simulations suggest two possible goals for such work. On the one hand, we might aim to prove that the ground state manifold is connected for $\alpha \ll 1$. On the other hand, we could also try to prove that the ground state manifold is disconnected for $0 < \frac{3}{2} - \alpha \ll 1$.

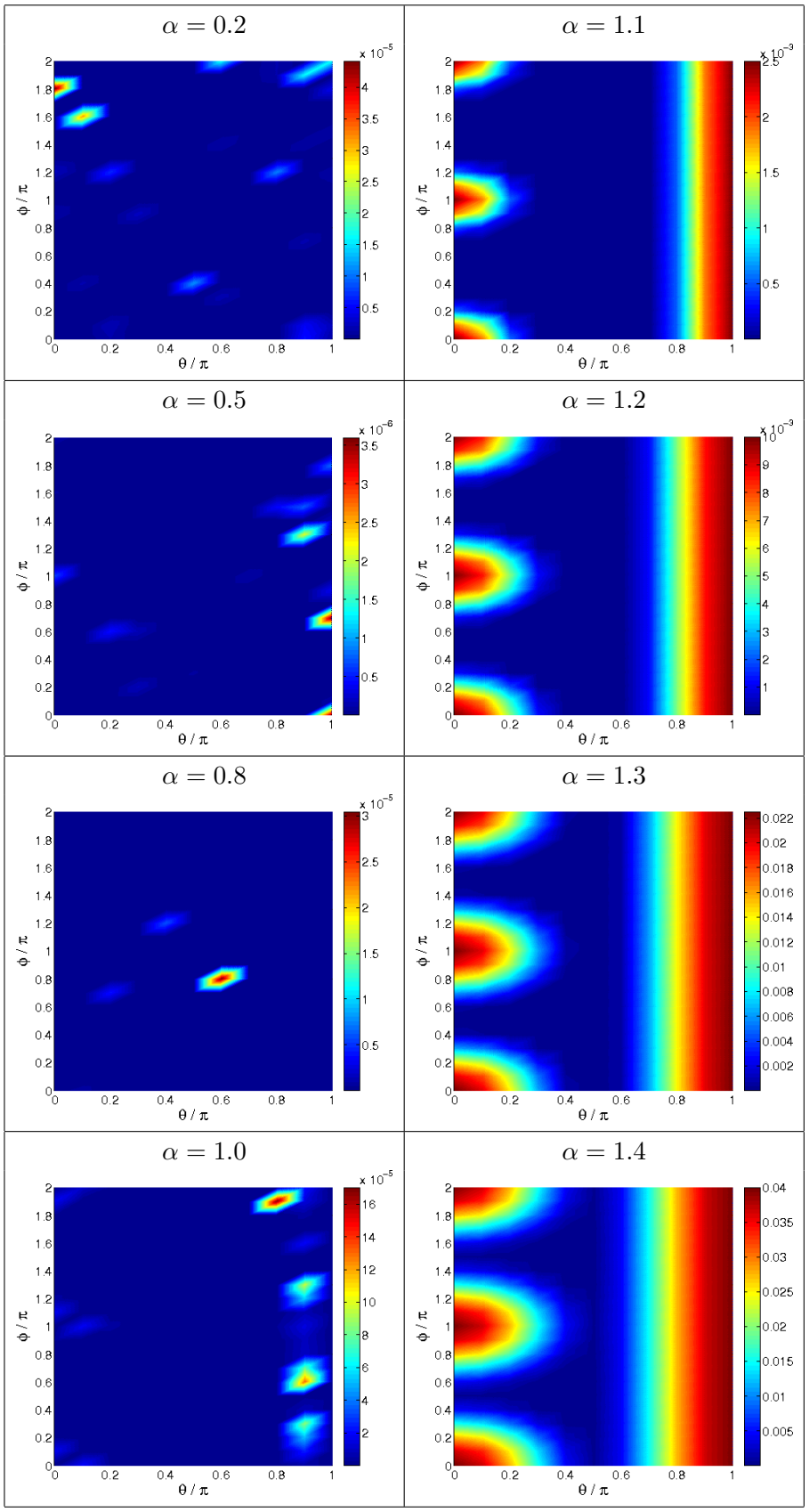


Figure 3.6: Minimum spin cluster energy (per spin) E for $N_C = 4$, measured (in units of J_1) relative to the theoretical ground state energy. The "jaw" angle θ and "flapping" angle ϕ that parameterise the internal degrees of freedom are illustrated in Fig. 3.5.

3.1.4 Stable defects

A possible route to proving the disconnectedness of the ground state manifold would be to show that the ground states can have topological defects, as the different topological sectors are disconnected. In this subsection, we discuss how this could work, though we remain inconclusive on this point because a finite core energy for defects might mean that only defect-free states are in the ground state manifold.

We first consider more carefully the ordered ground states for $\alpha \geq \frac{3}{2}$. As mentioned in Section 3.1.2, the kagome spins in each bipyramid meet at mutual 120° angles on the uncapped triangles. As all the kagome lattice spins are simply anti-aligned with their associated apical spins in the ordered ground state, we can always just focus on the apical spins, which lie on a triangular lattice in each layer (see Fig. 3.7).

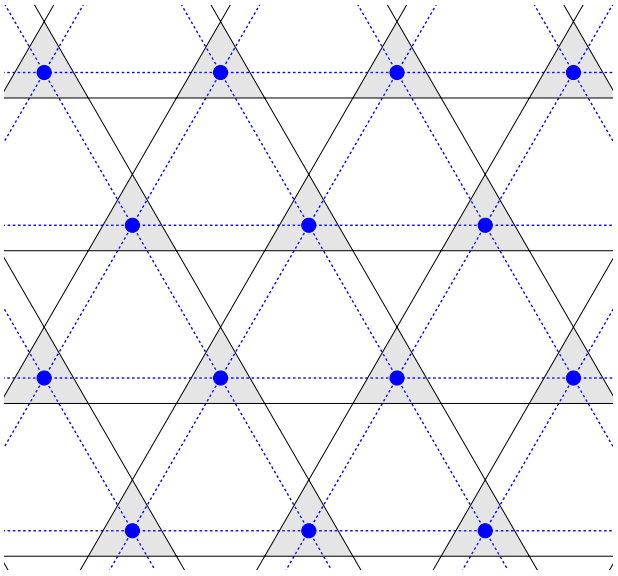


Figure 3.7: Triangular lattice of apical spins in a layer of the extended kagome lattice. Blue dots represent apical spin positions above and below the kagome layer for the shaded triangles (bipyramids).

As the apical spins are aligned in columns for the extended kagome lattice, these ordered ground states for $\alpha \geq \frac{3}{2}$ are in one-to-one correspondence with the ground states of the classical Heisenberg antiferromagnet on a triangular lattice. As the 120° spin structure is rigidly enforced throughout the lattice in ground states, choosing the orientations of three spins around a single triangle of the triangular lattice fixes the spin configuration of the whole lattice. Thus, the order parameter space for ground states is the full proper

three-dimensional rotation group $SO(3)$. As mentioned in Section 1.1.3, the fundamental group of the order parameter space of a 2D system governs the combination of topological point defects. The fundamental group for $SO(3)$ is Z_2, the group with two elements.[4] Kawamura and Miyashita have performed Monte Carlo simulations to show that there is a phase transition for the Heisenberg antiferromagnet on the triangular lattice due to the dissociation of these Z_2 point defects.[57,58]

In the papers by Kawamura and Miyashita, the discussion of stable defects is in the context of *low temperature states*, where the ground state constraints are approximately satisfied. Intuitively, this approach might also apply to stable defects within the manifold of *actual ground states* for $0 < \frac{3}{2} - \alpha \ll 1$. The idea is that the slight deviation from $\alpha = \frac{3}{2}$ relaxes the 120° correlations between apical spins, mimicking the effect of thermal fluctuations. So while we are still at zero temperature and the kagome spins have the strict 120° structure around the uncapped triangles, the kagome spins in the bipyramids are no longer exactly anti-aligned with the apical spins. If this idea is correct, we might have taken a step towards proving that the ground state manifold has at least two disconnected pieces, though we are far from a proof. The main difficulty lies with the question of the core energy for creating a defect. The ground state manifold can contain *both topological sectors* only if the core energy is zero. Otherwise, there will be no defects in ground states and the topological argument cannot be applied to prove the disconnectedness of the ground state manifold.

3.1.5 Correlations in numerical ground states

To test our ideas about the characteristics of ground states, it is useful to study numerical ground states. Such states were obtained as described in Section 5.2.1 in order to calculate spin dynamics using linear spinwave theory.

From the discussion in Section 2.2.2, we expect that the triangular lattice spins are highly correlated in the interlayer direction, which we also saw in Fig. 2.10 from the simulations reported by Manuel et al.[20] For our numerical ground states, we were able to verify that they are indeed identical to high precision from layer to layer. We might have expected from Eq. (3.8) based on Maxwell counting that a given configuration of triangular lattice spins determines a unique kagome ground state. If so, the kagome spins

should similarly be highly correlated from layer to layer because they "see" the same apical spins. However, we see from the correlations of kagome spins[†] in Fig. 3.8 that this is not the case, and that the kagome spins *quickly decorrelate* between layers. This contrasting behaviour for the interlayer correlations of the kagome and triangular lattice spins can be explained by the periodic boundary conditions that we imposed on our numerical ground states. As we saw from Eq. (3.9), the boundary conditions actually lead to additional degrees of freedom introduced by each kagome layer.

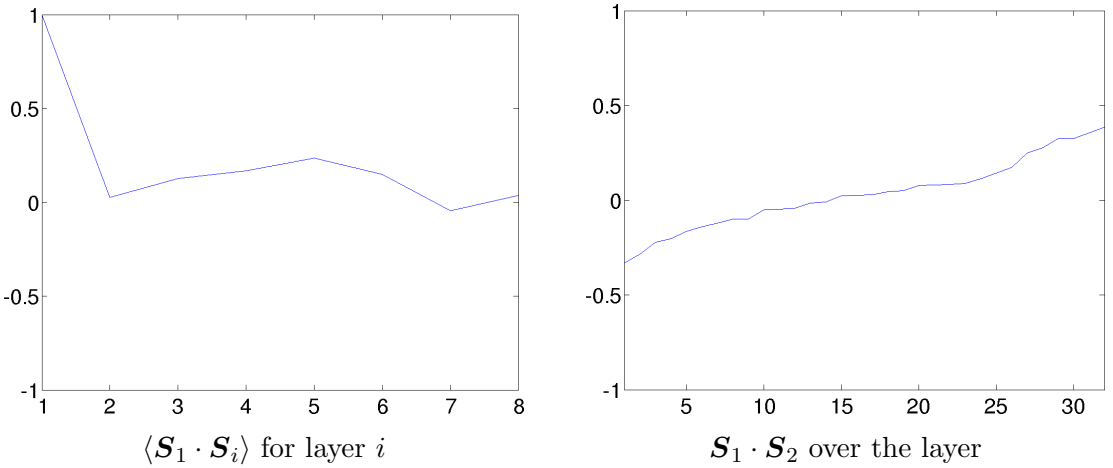


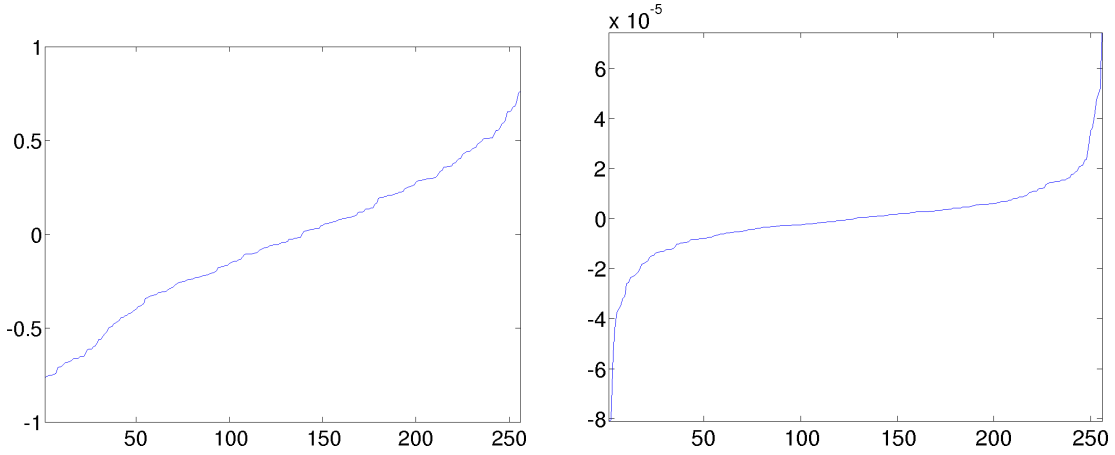
Figure 3.8: Kagome spin correlations in the interlayer direction. Results are shown for a numerical ground state of a system with 1,024 spins ($4 \times 4 \times 8$ unit cells). We set $\alpha = J_2/J_1 = \frac{1}{2}$. *(Left):* The scalar product is calculated for the kagome spins in the first layer and those in the same positions in different layers, then averaged over all positions in the layers. *(Right):* Distribution of the scalar product of kagome spins in the first layer and those in the same positions in the closest layers of the same plane type.

Another idea we tested on numerical ground states was whether the spins are coplanar. This is motivated by the results of Buhrandt and Fritz on order by disorder, which we review in Section 3.2. Briefly, they found that the order by disorder mechanism selects coplanar spin configurations in the classical Heisenberg spin model on the extended kagome lattice.[50] If the spins in our numerical ground states are indeed coplanar, the Maxwell counting argument will be quite misleading because the ground state constraints are not linearly independent. To test for coplanarity, we calculated the scalar chirality for each triangle of spins

$$K_s = \boldsymbol{S}_1 \cdot (\boldsymbol{S}_2 \times \boldsymbol{S}_3) \,, \tag{3.12}$$

[†]These spin correlations are calculated from $(\boldsymbol{S}_i \cdot \boldsymbol{S}_j)$ for kagome spins i, j in different layers but taking the same position within the layer. As the kagome layers stack in an alternating $...ABABA...$ fashion, we only compare spins from the same plane type.

which is zero if the three spins are coplanar. We calculated the average over the lattice of $(K_s)^2$ for the triangles in the kagome layers, and found that the kagome spins around the uncapped triangles are coplanar to a good approximation, but not the kagome spins in bipyramids. Both these findings are in accord with the description of the ground state constraints in Section 2.2.2. The distributions of K_s over the bicapped and uncapped triangles are shown in Fig. 3.9.



K_s for bicapped triangles

K_s for uncapped triangles

Figure 3.9: Distribution of the scalar chirality K_s for the kagome layer spins in bicapped and uncapped triangles of the extended kagome lattice. Results are shown for a numerical ground state of a system with 1,024 spins ($4 \times 4 \times 8$ unit cells), which has 256 bicapped and 256 uncapped triangles. We set $\alpha = J_2/J_1 = \frac{1}{2}$. Note the much smaller vertical scale for the uncapped triangles.

We can also calculate the scalar chirality for the triangular layer spins in the system. We also find that these spins are *not coplanar*. The distribution of K_s for the triangular lattice spins is shown in Fig. 3.10. Note that if there are N_C bipyramids in a layer, then the number of spin triangles in each triangular layer is $2N_C$, since each apical spin is part of six such triangles, and each triangle has three spins.

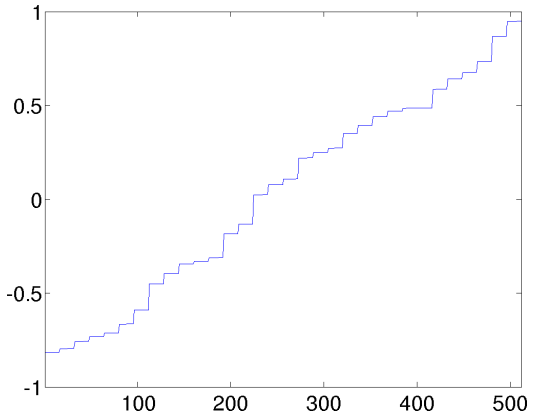


Figure 3.10: Distribution of the scalar chirality K_s for the triangular layer spins in the extended kagome lattice. Results are shown for a numerical ground state of a system with 1,024 spins ($4\times4\times8$ unit cells), which has 512 spin triangles in the triangular lattice layers. We set $\alpha = J_2/J_1 = \frac{1}{2}$.

3.2 Order by disorder

We now venture away from the ground state manifold, and into the low temperature regime. In this section, we briefly review recent theoretical results in the literature arguing that order by disorder occurs in the model we have been considering, i.e., the classical nearest-neighbour antiferromagnetic Heisenberg model on the extended kagome lattice.

Buhrandt and Fritz[50] performed a classical spin wave analysis around the ordered coplanar state for $\alpha\sigma = \frac{3}{2}$, and found two local soft modes, as depicted in Fig. 3.11. For $\alpha\sigma < \frac{3}{2}$, these soft modes are still present for coplanar ground states and absent in non-coplanar ground states. Thus the coplanar ground states are entropically selected in a first-order nematic transition. Using classical Monte Carlo simulations, and looking at the specific heat and a nematic order parameter, they established the phase boundaries numerically, as shown in Fig. 3.12.

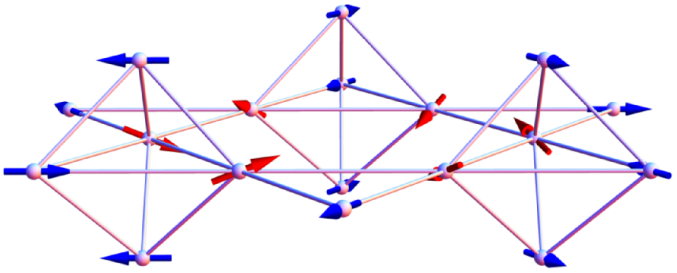


Figure 3.11: Local soft mode in coplanar ground state configurations for $\alpha\sigma = 3/2$: blue spins are idle while the red spins tilt out of the plane by $\pm\epsilon$ in an alternating fashion, leading to an energy cost $\omega \propto \epsilon^4$. Taken from Ref. [50].

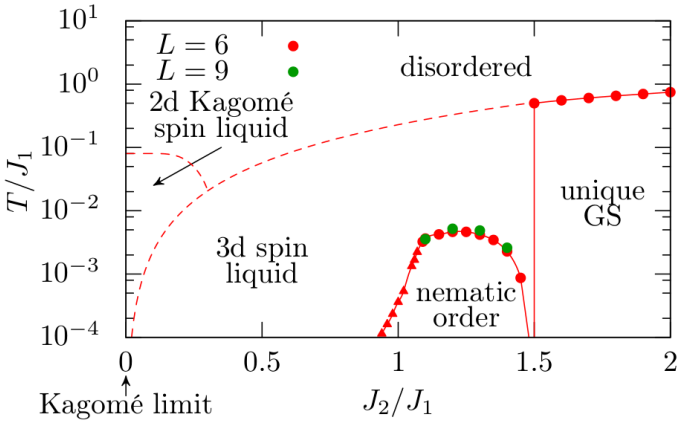


Figure 3.12: Phase diagram for the extended kagome lattice as a function of $\alpha\sigma = J_2/J_1$ and temperature T/J_1. At low T there is a first-order transition to a nematically ordered phase, driven entropically by the order by disorder mechanism. Taken from Ref. [50].

CHAPTER 4

Statistical mechanics of the classical spin model

> Our children are counting on us to provide two things: consistency and structure. Children need parents who say what they mean, mean what they say, and do what they say they are going to do.
>
> — *Barbara Coloroso*

Following our discussion of ground states in the previous chapter, we now study the finite temperature behaviour of the classical spin system. We discuss two complementary approaches to characterising the static spin correlations, which will be subsequently woven together into a stochastic model for the spin dynamics in Chapter 6. The first approach of Section 4.1 is known as the self-consistent Gaussian approximation (SCGA), which gives us an analytical approximation to the partition function that we can use to work out the equilibrium statistical mechanics. We shall see in Section 4.1.5 that the calculated structure factors from SCGA work reasonably well in reproducing the intensity patterns obtained from elastic magnetic neutron scattering on $YBaCo_4O_7$. The second approach of Section 4.2 involves obtaining the effective interaction between kagome spins by integrating out the triangular lattice spins. While this can be done exactly since the triangular lattice spins do not couple directly with one another, the effective interaction obtained is not of a standard form — we will have to make further approximations in order to derive the spin dynamics in Chapter 6.

4.1 Self-consistent Gaussian approximation (SCGA)

To study the statistical mechanics of interacting systems, it is usually necessary to make approximations. The approximation scheme we will use in this section relaxes the rigid spin-length constraints on classical spins. Spins are allowed to take on any real vector value, while imposing a self-consistency condition that the expectation value of the squared spin length is normalised. This soft spin approximation scheme is known as the SCGA,[59]

and is the same as the spherical model approximation for an $O(n)$ spin model,[60] which is exact in the limit $n \to \infty$.[5] We are optimistic about such an approach because it has proved very successful on the frustrated pyrochlore lattice.[8,61–63]

We start with the classical Heisenberg Hamiltonian Eq. (2.6), with $\sigma = 1$,

$$\mathcal{H}[\{\boldsymbol{n}_i\}] = \tfrac{1}{2} J_1 S^2 \sum_{i,j} A_{ij}(\alpha)\, \boldsymbol{n}_i \cdot \boldsymbol{n}_j \ ,$$

where A_{ij} is the *interaction matrix* in Eq. (2.5). The partition function is

$$\mathcal{Z} = \int_{|\boldsymbol{n}_i|=1} \left[\prod_i \mathrm{d}^3 \boldsymbol{n}_i\right] \exp\left(-\beta \mathcal{H}[\{\boldsymbol{n}_i\}]\right) \ ,$$

where the Boltzmann weights take a simple Gaussian form because the Hamiltonian is quadratic in the spin variables. However, the integration measure is complicated by the constraints on the $\{\boldsymbol{n}_i\}$. To deal with these constraints, we introduce dimensionless Lagrange multipliers $\{\lambda_i\}$, to approximate the partition function

$$\mathcal{Z} \approx \mathcal{Z}_0 = \int \left[\prod_i \mathrm{d}^3 \boldsymbol{s}_i \, \exp\left(-\tfrac{1}{2}\lambda_i |\boldsymbol{s}_i|^2\right)\right] \exp\left(-\beta \mathcal{H}[\{\boldsymbol{s}_i\}]\right) \ . \tag{4.1}$$

We have an unconstrained integration over $\mathbb{R}^3$ for each spin vector $\boldsymbol{s}_i$, but configurations with larger spin values have small weight because of the additional exponential factor introduced. We must choose the $\{\lambda_i\}$ in such a way that the thermal average $\langle |\boldsymbol{s}_i|^2 \rangle = 1$ for all spins, which imposes a self-consistency condition.

The approximate partition function in Eq. (4.1) is easily evaluated, as it takes the form of a Gaussian integral. In this approximation, each of the spin components is independent, as the partition function factorises into a product of contributions from each spin component. Explicitly, $\mathcal{Z}_0 = Z^x Z^y Z^z$, where

$$Z^{x,y,z} = Z = \int \prod_i \mathrm{d}s_i \, \exp\left(-\tfrac{1}{2} \sum_{i,j} s_i M_{ij} s_j\right) . \tag{4.2}$$

Here $s_i \in \mathbb{R}$ refers to a single component of $\boldsymbol{s}_i$, and the *SCGA matrix* is

$$M_{ij} = \lambda_i \delta_{ij} + \beta J_1 S^2 A_{ij} \ , \tag{4.3}$$

where δ_{ij} is the Kronecker delta. We add a source term in order to evaluate the multivariate Gaussian integral in Eq. (4.2), as explained in books (such as Ref. [64]). Consider the more

general integral

$$Z(M,\boldsymbol{a}) = \int \prod_i \mathrm{d}s_i \, \exp\Big(-\tfrac{1}{2}\sum_{i,j} s_i M_{ij} s_j + \sum_i a_i s_i \Big) \, . \tag{4.4}$$

We can complete the square in the exponent to find the minimum of the quadratic form, and change variables from s_i to $t_i = s_i - \sum_j (M^{-1})_{ij} a_j$, which is measured relative to that minimum. Then Eq. (4.4) becomes

$$Z(M,\boldsymbol{a}) = \exp\Big(\tfrac{1}{2}\sum_{i,j} a_i (M^{-1})_{ij} a_j\Big) \times \int \prod_i \mathrm{d}t_i \, \exp\Big(-\tfrac{1}{2}\sum_{i,j} t_i M_{ij} t_j \Big) \, . \tag{4.5}$$

The spin correlation functions are obtained from differentiating $Z(M,\boldsymbol{a})$ with respect to the a_i's and setting the source term to zero. From Eq. (4.4), we get

$$\langle s_{i_1} \cdots s_{i_n} \rangle = \frac{1}{Z(M,\mathbf{0})} \left[\frac{\partial^n Z(M,\boldsymbol{a})}{\partial a_{i_1} \cdots \partial a_{i_n}} \right] \Bigg|_{\boldsymbol{a}=0}$$

and using Eq. (4.5) gives

$$\langle s_{i_1} \cdots s_{i_n} \rangle = \left[\frac{\partial^n}{\partial a_{i_1} \cdots \partial a_{i_n}} \exp\Big(\tfrac{1}{2}\sum_{i,j} a_i (M^{-1})_{ij} a_j\Big) \right] \Bigg|_{\boldsymbol{a}=0} \, . \tag{4.6}$$

In particular, we are interested in the two-spin correlation function given by the inverse of the SCGA matrix,

$$\langle s_i s_j \rangle = (M^{-1})_{ij} \, , \tag{4.7}$$

which also lead us to the self-consistency conditions

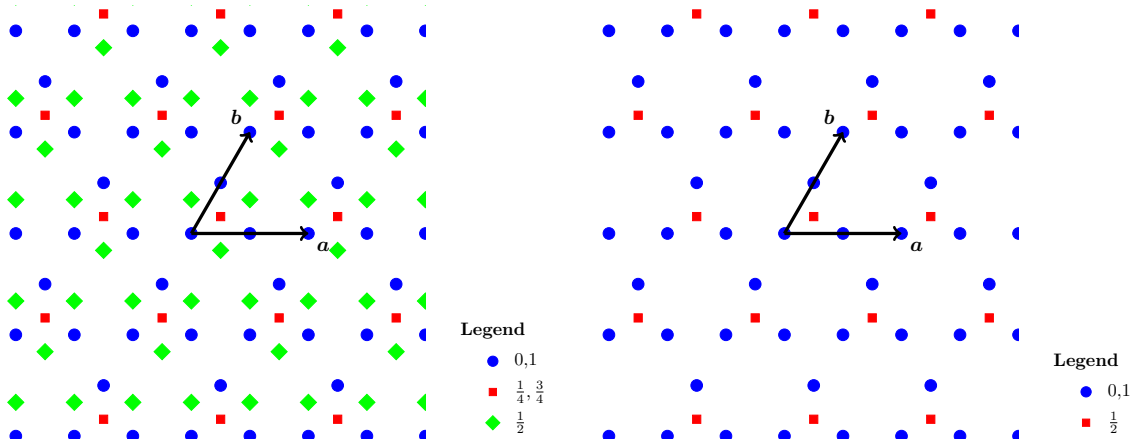
$$\frac{1}{3} = \langle s_i^2 \rangle = (M^{-1})_{ii} \, , \tag{4.8}$$

so that $\langle |\boldsymbol{s}_i|^2 \rangle = 1$. Conceptually, Eq. (4.7) and Eq. (4.8) summarise the essence of the SCGA approach.

4.1.1 Lattice Fourier transform

To exploit the translational symmetry of the crystal lattice, we will work in Fourier space. The unit cell for the extended kagome lattice has eight sites, as shown in Fig. 4.1a. For a first pass at the problem, we used a simpler geometry with the unit cell halved (see Fig. 4.1b). This simplified structure has the kagome planes identically stacked (...*AAA*... instead of ...*ABABA*...). We decided not to go on to treat the actual geometry thereafter because

we find an ordering transition that seems to be unphysical, as discussed in Section 4.1.4.



(a) Original unit cell with eight sites. **(b)** Simplified unit cell with four sites.

Figure 4.1: Plan view of original and simplified unit cells, with legends showing the fractional coordinates of sites in the $\boldsymbol{c}$ direction. The in-plane hexagonal lattice vectors are also shown.

With respect to the (right-handed) Cartesian coordinate system, we define the real-space lattice vectors for translation between unit cells on the triangular lattice,

$$\begin{cases} \boldsymbol{a} = \hat{x} \\ \boldsymbol{b} = \frac{1}{2}\hat{x} + \frac{\sqrt{3}}{2}\hat{y} \\ \boldsymbol{c} = \hat{z}\ . \end{cases} \tag{4.9}$$

We also introduce three mutually 120° vectors for translation between kagome sites,

$$\begin{cases} \boldsymbol{u} = \frac{1}{2}\boldsymbol{a} \\ \boldsymbol{v} = -\frac{1}{2}\boldsymbol{b} \\ \boldsymbol{w} = -\boldsymbol{u} - \boldsymbol{v}\ , \end{cases} \tag{4.10}$$

and another three mutually 120° vectors for translating from the kagome sites to the apical sites,

$$\begin{cases} \boldsymbol{\delta}_1 = \frac{1}{3}(\boldsymbol{u} - \boldsymbol{v}) \\ \boldsymbol{\delta}_2 = \frac{1}{3}(\boldsymbol{w} - \boldsymbol{u}) \\ \boldsymbol{\delta}_3 = \frac{1}{3}(\boldsymbol{v} - \boldsymbol{w})\ . \end{cases} \tag{4.11}$$

Each spin site is labelled by a pair (i, μ), where i is an index for the N unit cells, and μ indexes the four sites within each unit cell. The numbering convention and some of the

vectors introduced are shown in Fig. 4.2. Note that $\boldsymbol{\delta}_{1,2,3}$ goes from site $\{1,2,3\}$ to the projection of site 4 within the unit cell. The Fourier conventions are

$$\begin{cases} s_i^\mu = \dfrac{1}{\sqrt{N}} \displaystyle\sum_{\boldsymbol{q}} s_{\boldsymbol{q}}^\mu e^{i\boldsymbol{q}\cdot\boldsymbol{r}_i^\mu} \\ s_{\boldsymbol{q}}^\mu = \dfrac{1}{\sqrt{N}} \displaystyle\sum_{i} s_i^\mu e^{-i\boldsymbol{q}\cdot\boldsymbol{r}_i^\mu} \end{cases} , \tag{4.12}$$

where $\boldsymbol{r}_i^\mu$ is the position vector of the spin s_i^μ and the sum over wavevector $\boldsymbol{q}$ is understood to be taken over the N sites of the 3D Brillouin zone (BZ). Translational symmetry also means that the Lagrange multipliers we introduce should only depend on the label μ, so we write the SCGA matrix in Eq. (4.3) as

$$M_{ij}^{\mu\nu} = \lambda^\mu \delta_{ij} \delta^{\mu\nu} + \beta J_1 S^2 A_{ij}^{\mu\nu} . \tag{4.13}$$

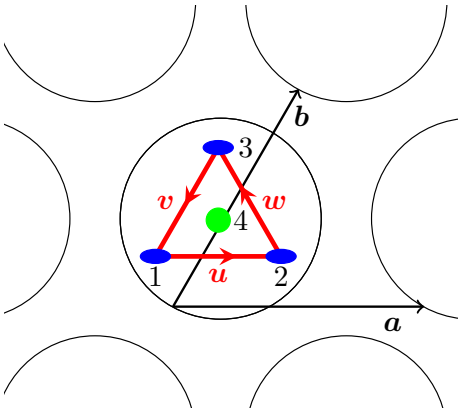


Figure 4.2: 4-site unit cell for SCGA. Sites 1–3 have fractional coordinate 0 in the $\boldsymbol{c}$ direction, and site 4 has fractional coordinate $\frac{1}{2}$. The vectors shown are defined in Eq. (4.9) and Eq. (4.10).

Since the transformation from real-space to reciprocal space is unitary, the Jacobian is 1, and so we have from Eq. (4.2) that

$$Z = \int \prod_{\boldsymbol{q},\mu} \mathrm{d}s_{\boldsymbol{q}}^\mu \, \exp\left(-\tfrac{1}{2} \sum_{\substack{\boldsymbol{q},\mu \\ \boldsymbol{k},\nu}} s_{\boldsymbol{q}}^\mu M_{\boldsymbol{q}\boldsymbol{k}}^{\mu\nu} s_{\boldsymbol{k}}^\nu\right) .$$

After the Fourier transform, the SCGA matrix is block-diagonal in the wavevector, i.e., $M_{\boldsymbol{q}\boldsymbol{k}}^{\mu\nu} = \delta_{\boldsymbol{q},-\boldsymbol{k}} \left[M(\boldsymbol{q})\right]^{\mu\nu}$. The matrix $M(\boldsymbol{q})$ acts within the space of the four sublattice sites for each $\boldsymbol{q}$. We have

$$Z = \int \prod_{\boldsymbol{q},\mu} \mathrm{d}s_{\boldsymbol{q}}^\mu \, \exp\left(-\tfrac{1}{2} \sum_{\boldsymbol{q},\mu,\nu} s_{\boldsymbol{q}}^\mu \left[M(\boldsymbol{q})\right]^{\mu\nu} s_{-\boldsymbol{q}}^\nu\right) , \tag{4.14}$$

and the two-spin correlation function in this basis is

$$\langle s^{\mu}_{\boldsymbol{q}} s^{\nu}_{-\boldsymbol{q}} \rangle = \left[M^{-1}(\boldsymbol{q}) \right]^{\mu\nu} . \tag{4.15}$$

We can diagonalise the Hermitian matrix $M(\boldsymbol{q})$ by a unitary transformation. Let $U(\boldsymbol{q})$ be the unitary matrix of normalised eigenvectors so that

$$M(\boldsymbol{q})\, U(\boldsymbol{q}) = U(\boldsymbol{q})\, D(\boldsymbol{q}) ,$$

where the matrix $D(\boldsymbol{q})$ is diagonal with elements $[D(\boldsymbol{q})]^{ab} = \delta^{ab} \xi^a(\boldsymbol{q})$. The bands $\{\xi^a(\boldsymbol{q})\}$, indexed by $a = 1, \ldots, 4$ are the eigenvalues of $M(\boldsymbol{q})$, and we always want $\xi^a(\boldsymbol{q}) > 0$ so that $D(\boldsymbol{q})$ is invertible. Then (suppressing the wavevector label) we have

$$\begin{cases} D^{-1} = U^{-1}\, M^{-1}\, U \\ M^{-1} = U\, D^{-1}\, U^{-1} , \end{cases}$$

and Eq. (4.15) can be written as

$$\langle s^{\mu}_{\boldsymbol{q}} s^{\nu}_{-\boldsymbol{q}} \rangle = \sum_a \frac{U^{\mu a} \left[U^{-1} \right]^{a\nu}}{\xi^a} = \sum_a \frac{U^{\mu a} \overline{U}^{\nu a}}{\xi^a} , \tag{4.16}$$

using the overbar to denote complex conjugation. The self-consistency conditions in Eq. (4.8) take the form

$$\begin{aligned} \frac{1}{3} &= \langle (s^{\mu}_i)^2 \rangle = \frac{1}{N} \sum_{\boldsymbol{q}} \langle s^{\mu}_{\boldsymbol{q}} s^{\mu}_{-\boldsymbol{q}} \rangle \\ \frac{1}{3} &= \frac{1}{N} \sum_{\boldsymbol{q},a} \frac{\left| [U(\boldsymbol{q})]^{\mu a} \right|^2}{\xi^a(\boldsymbol{q})} \\ &\underset{N\to\infty}{=} \frac{1}{\Omega_{\mathrm{BZ}}} \int \mathrm{d}^3\boldsymbol{q} \sum_a \frac{\left| [U(\boldsymbol{q})]^{\mu a} \right|^2}{\xi^a(\boldsymbol{q})} . \end{aligned} \tag{4.17}$$

In the last line, we pass, in the thermodynamic limit, from a sum to an integral over the BZ (of volume $\Omega_{\mathrm{BZ}} = 4\pi^3/\sqrt{3}$ in reciprocal lattice units).

4.1.2 Band structure

It is clear from Eq. (4.17) that the eigenvalues and eigenvector weights of the SCGA matrix are central to the SCGA approach. In the Fourier basis, we have

$$[M(\boldsymbol{q})]^{\mu\nu} = \lambda^{\mu} \delta^{\mu\nu} + \beta J_1 S^2 [A(\boldsymbol{q})]^{\mu\nu} . \tag{4.18}$$

We can write out the 4×4 interaction matrix $A(\boldsymbol{q})$ explicitly[†] as

$$A(\boldsymbol{q}) = \begin{pmatrix} 0 & u & v & cd_1 \\ u & 0 & w & cd_2 \\ v & w & 0 & cd_3 \\ c\overline{d_1} & c\overline{d_2} & c\overline{d_3} & 0 \end{pmatrix} , \tag{4.19}$$

where the $\boldsymbol{q}$ dependence is contained in the variables

$$\begin{cases} u = 2\cos(\boldsymbol{q}\cdot\boldsymbol{u}) \\ v = 2\cos(\boldsymbol{q}\cdot\boldsymbol{v}) \\ w = 2\cos(\boldsymbol{q}\cdot\boldsymbol{w}) \\ c = \alpha\left[2\cos\left(\frac{1}{2}\boldsymbol{q}\cdot\boldsymbol{c}\right)\right] = \alpha\left[2\cos\left(\frac{q_z}{2}\right)\right] \\ d_{1,2,3} = \exp(i\boldsymbol{q}\cdot\boldsymbol{\delta}_{1,2,3}) \, . \end{cases} \tag{4.20}$$

The dependence on q_z is entirely contained in the variable c, which shows us that having $q_z \neq 0$ can be thought of as reducing the effective value of α, to a vanishing value for $q_z = \pm\pi$ at the edges of the BZ.

The band structure of $A(\boldsymbol{q})$ as a function of (q_x, q_y) is shown in Fig. 4.3, for various values of α with $q_z = 0$. We notice that there is always a *flat band* at the eigenvalue -2, corresponding to the (unnormalised) eigenvector $\vec{U}_1(\boldsymbol{q})$ with *weight on kagome sites only*,

$$\vec{U}_1(\boldsymbol{q}) \propto \begin{pmatrix} \sin(\boldsymbol{q}\cdot\boldsymbol{w}) \\ \sin(\boldsymbol{q}\cdot\boldsymbol{v}) \\ \sin(\boldsymbol{q}\cdot\boldsymbol{u}) \\ 0 \end{pmatrix} . \tag{4.21}$$

For the case of $\alpha = 0$, the eigenvectors on the kagome and apical sites completely decouple, and the band for the apical site is also flat with the eigenvalue of zero. For $\alpha > 0$, the eigenvectors other than $\vec{U}_1(\boldsymbol{q})$ mix the kagome and apical sites together. For $\alpha = \frac{1}{\sqrt{2}} \approx 0.7$, the band corresponding to another eigenvector is *exactly degenerate* with the kagome flat band at -2. So while the kagome flat band is the lowest band for $\alpha < \frac{1}{\sqrt{2}}$, the lowest band

[†]Rows and columns are numbered according to the site conventions in Fig. 4.2.

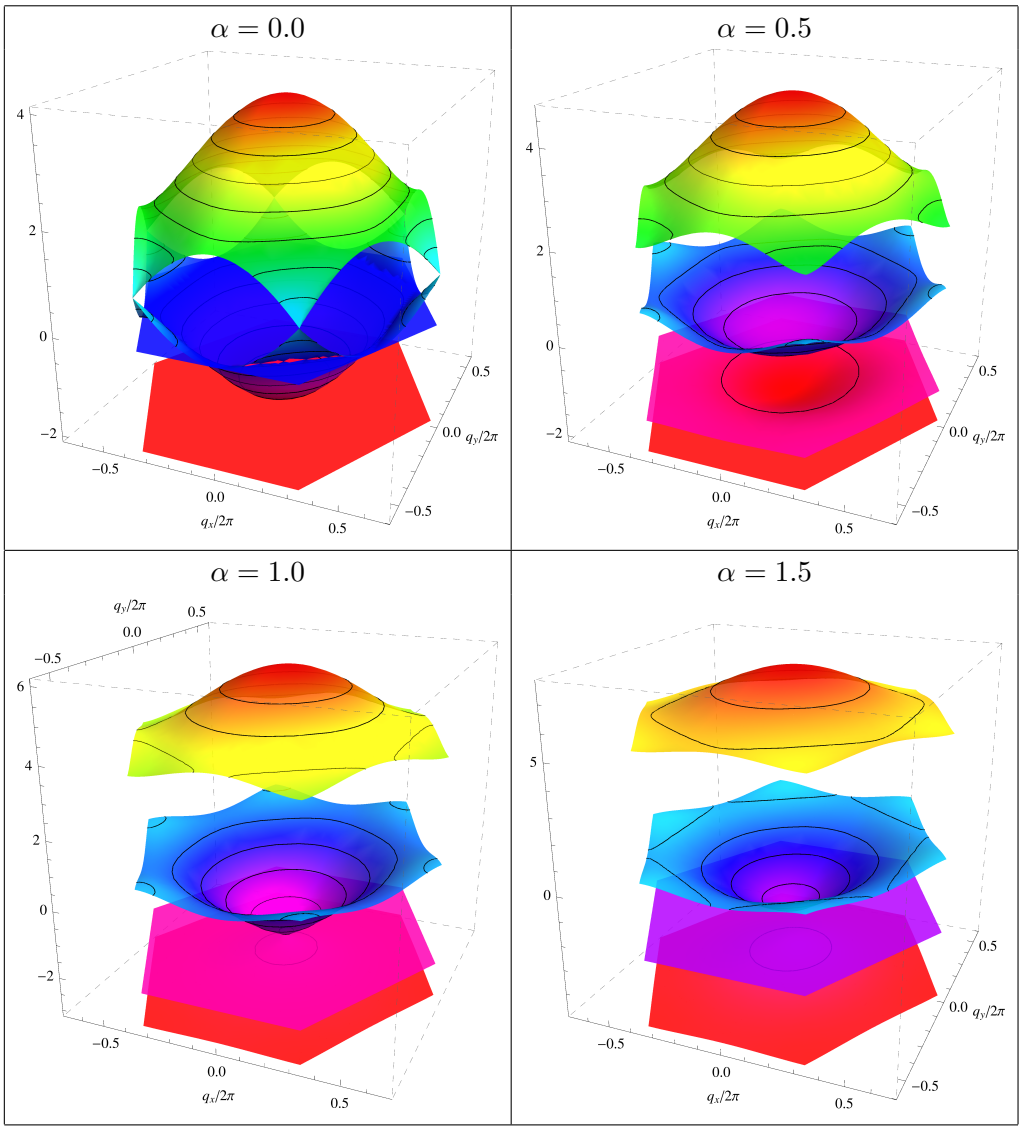


Figure 4.3: Band structure for interaction matrix $A(\boldsymbol{q})$ of the 4-site unit cell.

is dispersive for $\alpha > \frac{1}{\sqrt{2}}$.

4.1.3 Self-consistency conditions

We will use the self-consistency conditions Eq. (4.17) to determine the Lagrange multipliers, which we then use to calculate correlation functions from Eq. (4.16). We need two Lagrange multipliers, one for the kagome sites and another for the apical sites. We argued earlier that the eigenvalues of the SCGA matrix must be positive everywhere for our calculations to make sense, which suggests a natural way to parameterise these Lagrange multipliers.

We define λ and Λ by setting

$$\lambda^{\mu} = \begin{cases} \lambda + 2\beta J_1 S^2 & \text{for } \mu = 1,2,3 \text{ (kagome sites)} \\ \lambda + \beta J_1 S^2 (2+\Lambda) & \text{for } \mu = 4 \text{ (apical site).} \end{cases} \tag{4.22}$$

With these definitions, we can write the SCGA matrix Eq. (4.18) as

$$M(\boldsymbol{q}) = \lambda \mathbb{1} + \beta J_1 S^2 V(\boldsymbol{q}) \,, \tag{4.23}$$

with

$$V(\boldsymbol{q}) \equiv \Lambda \mathbb{1}_A + 2\mathbb{1} + A(\boldsymbol{q}) \,. \tag{4.24}$$

Here $\mathbb{1}$ is the 4×4 identity matrix and $\mathbb{1}_A$ is the 4×4 matrix with one in the bottom right corner and zeroes everywhere else.

The eigenvectors of $M(\boldsymbol{q})$ are the eigenvectors of $V(\boldsymbol{q})$, but the necessity of introducing Λ in addition to λ means that unlike SCGA on the pyrochlore lattice with a single Lagrange multiplier,[62,63] these eigenvectors are different from those of the interaction matrix $A(\boldsymbol{q})$ when $\Lambda \neq 0$. Only the eigenvector $\vec{U}_1(\boldsymbol{q})$ in Eq. (4.21) is common to the matrices and always gives a flat band. The band structure of $A(\boldsymbol{q})$ in Fig. 4.3 thus only approximates the band structure of $M(\boldsymbol{q})$ and $V(\boldsymbol{q})$. We can roughly think of $V(\boldsymbol{q})$ as having bands similar to $A(\boldsymbol{q})$, but with all bands shifted such that the kagome flat band is at zero, and the $\Lambda \mathbb{1}_A$ term produces an additional shift to the band with the largest apical weight.[†]

To solve the self-consistency conditions in Eq. (4.17) for each site μ in the unit cell simultaneously, we write the eigenvectors of $V(\boldsymbol{q})$ as $\{\vec{U}_a(\boldsymbol{q})\}$, with $a \in \{1, \ldots, 4\}$. Since the eigenvectors are normalised, the sum of the weight on kagome sites is related to the weight on the apical site, i.e.,

$$\sum_{\mu \neq 4} \left| [\vec{U}_a(\boldsymbol{q})]_\mu \right|^2 = 1 - \left| [\vec{U}_a(\boldsymbol{q})]_4 \right|^2 .$$

The kagome flat band (labelled $a = 1$) has no weight on the apical sites, so we can rewrite the self-consistency equations as two equations, one for the sum over kagome sites and the

[†]This band is the (dispersive) lowest band of $A(\boldsymbol{q})$ for $\alpha > \frac{1}{\sqrt{2}}$ in Fig. 4.3.

other for the apical site,

$$\begin{cases} 1 = \dfrac{1}{\lambda} + f_K(\alpha, \beta, \lambda, \Lambda) \\ \dfrac{1}{3} = f_A(\alpha, \beta, \lambda, \Lambda) \ . \end{cases} \tag{4.25}$$

The functions

$$\begin{cases} f_K(\alpha, \beta, \lambda, \Lambda) \equiv \dfrac{1}{\Omega_{\mathrm{BZ}}} \displaystyle\int \mathrm{d}^3\boldsymbol{q} \sum_{a\neq 1} \left(\frac{1 - \left|[\vec{U}_a(\boldsymbol{q})]_4\right|^2}{\lambda + \beta J_1 S^2 v_a(\boldsymbol{q})} \right) \\ f_A(\alpha, \beta, \lambda, \Lambda) \equiv \dfrac{1}{\Omega_{\mathrm{BZ}}} \displaystyle\int \mathrm{d}^3\boldsymbol{q} \sum_{a\neq 1} \left(\frac{\left|[\vec{U}_a(\boldsymbol{q})]_4\right|^2}{\lambda + \beta J_1 S^2 v_a(\boldsymbol{q})} \right) \end{cases} \tag{4.26}$$

are sums over the bands $a \neq 1$ and integrated over the BZ. Note that the dependence on α and Λ is implicitly embedded in the eigenvectors $\{\vec{U}_a(\boldsymbol{q})\}$ and eigenvalues $\{v_a(\boldsymbol{q})\}$ of the matrix $V(\boldsymbol{q})$.

With $\beta = 0$, we see that the denominators in Eq. (4.26) are constant for all bands, so $f_K = 2/\lambda$ and $f_A = 1/\lambda$. We see from Eq. (4.25) that $\lambda = 3$ in this limit, for all α, and we can also put $\Lambda = 0$. We proceed numerically for $\beta > 0$, solving Eq. (4.25) simultaneously for λ and Λ. We start with initial guesses for (λ, Λ) and converge to the self-consistent solutions by repeatedly performing bisection alternately on the pair of equations until the desired accuracy is reached. The integrals over the BZ are performed using a discrete mesh of $80 \times 80 \times 80$ points. The numerical solutions are shown in Fig. 4.4, with each data point corresponding to a particular value of β.

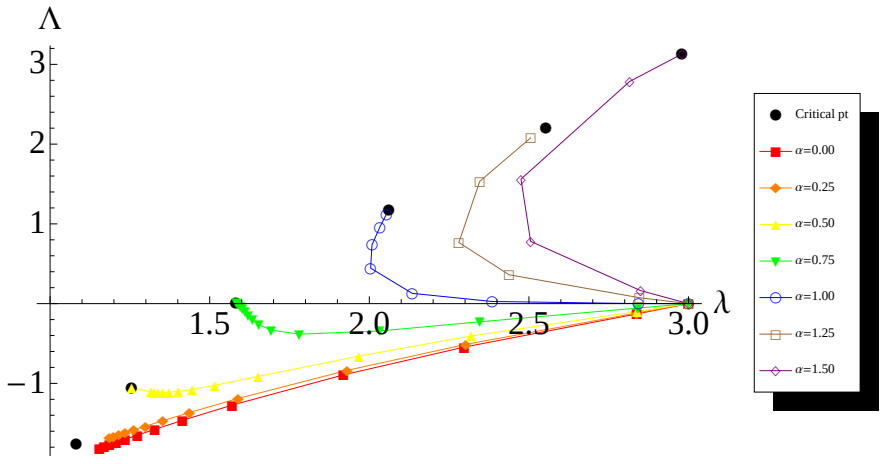


Figure 4.4: Self-consistent values for the Lagrange multipliers (λ, Λ) obtained numerically from Eq. (4.25). The solutions at the critical points are specially indicated for $\alpha > 0$.

4.1.4 Ordering transition

As β increases, the conditions Eq. (4.25) can no longer be satisfied subject to the constraints that the denominators $\lambda + \beta J_1 S^2 v_a(\boldsymbol{q}) > 0$ everywhere. This happens because the lowest band of $V(\boldsymbol{q})$ is *not flat*, but has minima (with negative values) at *discrete points* in the BZ. By increasing β, we find the transition point $\beta_c = \beta_c(\alpha)$ when the denominators approach zero at these minima,

$$\min_{\{a,\boldsymbol{q}\}} [\lambda + \beta_c J_1 S^2 v_a(\boldsymbol{q})] = 0 \, . \tag{4.27}$$

Below the transition temperature, for $\beta > \beta_c$, the value of λ needs to be larger to avoid negative values for $\lambda + \beta J_1 S^2 v_a(\boldsymbol{q})$, but then the integrals f_K and f_A will be too small to satisfy Eq. (4.25). The transition points for various values of α are shown in Fig. 4.5. Note that $\beta_c \to \infty$ for $\alpha = 0$, since in this case the kagome and apical sites decouple and there is a flat band for both sublattices.

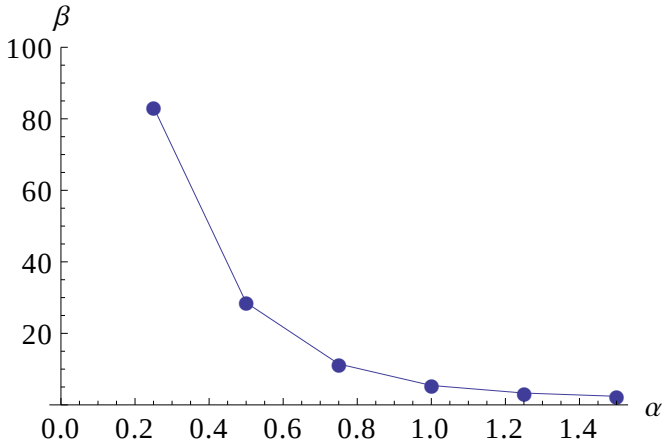


Figure 4.5: Transition points in the SCGA. The values β are measured in units of $(J_1 S^2)^{-1}$.

We argue that this ordering transition is *unphysical* because the frustration is artificially lifted. In general terms, the SCGA simplifies the partition function by changing the integration measure and assigning non-zero probability to unphysical spin configurations, but does this in a way that *does not distort* the band structure of the interactions. For example, the SCGA works well for both the pyrochlore and kagome lattices, with the lowest band remaining flat at all temperatures.[62,65] However, we found that we had to introduce a second Lagrange multiplier Λ in order to satisfy the self-consistency conditions on all sites

in Eq. (4.25). The $\Lambda \mathbb{1}_A$ term in Eq. (4.24) for the matrix $V(\boldsymbol{q})$ shifts the dispersive bands *relative* to the kagome flat band, causing an unphysical distortion to the band structure. As the partition function is a Gaussian integral under the SCGA, there are only quadratic modes, so this ordering transition we find is certainly not related to the order by disorder mechanism.

4.1.5 Static structure factor

Having obtained the Lagrange multipliers numerically (see Fig. 4.4), we can calculate spin correlations to simulate the magnetic structure factor from neutron scattering. The magnetisation of a unit cell is

$$m_{\boldsymbol{q}} = \sum_{\mu} s^{\mu}_{\boldsymbol{q}}$$

and the structure factor is the correlation function

$$S(\boldsymbol{q}) = \langle m_{\boldsymbol{q}} m_{-\boldsymbol{q}} \rangle = \sum_{\mu,\nu} \langle s^{\mu}_{\boldsymbol{q}} s^{\nu}_{-\boldsymbol{q}} \rangle \ , \tag{4.28}$$

which can be calculated using Eq. (4.16).

We compare our results with the $YBaCo_4O_7$ magnetic neutron scattering experiments and Monte Carlo simulations shown in Fig. 2.9. The experiments were performed at $T = 130$ K,[20] with the mean-field antiferromagnetic exchange $J/k_B \sim 35$ K extracted from the paramagnetic susceptibility.[19] Using the average value of $S = 1.625$, we get $\beta J S^2 \sim 1$. To compare our results with neutron scattering data, we also need to correct for the magnetic form factors. Following Manuel et al.,[20] we ignore the fact that the cobalt is mixed-valent and just include the magnetic form factor for Co^{2+} under the dipole approximation for spin-only scattering. Specifically, we multiply $S(\boldsymbol{q})$ by a factor $|f(\boldsymbol{q})|^2$, where

$$f(\boldsymbol{q}) = f(q \equiv |\boldsymbol{q}|) = Ae^{-aq^2} + Be^{-bq^2} + Ce^{-cq^2} + D \ .$$

The tabulated empirical values for Co^{2+} are[66]

$$\begin{cases} A = 0.4332; B = 0.5857; C = -0.0382; D = 0.0179 \\ a = 14.355; b = 4.608; c = 0.134 \end{cases}$$

and we use the hexagonal lattice parameters for $YBaCo_4O_7$ from Valldor and Andersson[17]

$$\begin{cases} a_{hex} = b_{hex} = 6.2982 \text{ Å} \\ c_{hex} = 10.2467 \text{ Å}. \end{cases}$$

The structure factors are calculated using Eq. (4.28) for $\beta J_1 S^2 = 1$, over a range of α. These are shown in Fig. 4.6 as colour plots after including the magnetic form factors. We see that at sufficiently high α, the main features of the magnetic neutron scattering patterns in Fig. 2.9 emerge, showing that the SCGA approach captures the physics of the classical spin liquid phase. We see the scattering weight shifting away from the zone centre and towards the outer edges of the Wigner-Seitz cells surrounding the first Brillouin zone in the $(hk0)$-plane. In the $(0kl)$-plane, we see the appearance of diffuse spots that are broader in the $\boldsymbol{b}^*$ direction than in the $\boldsymbol{c}^*$ direction.

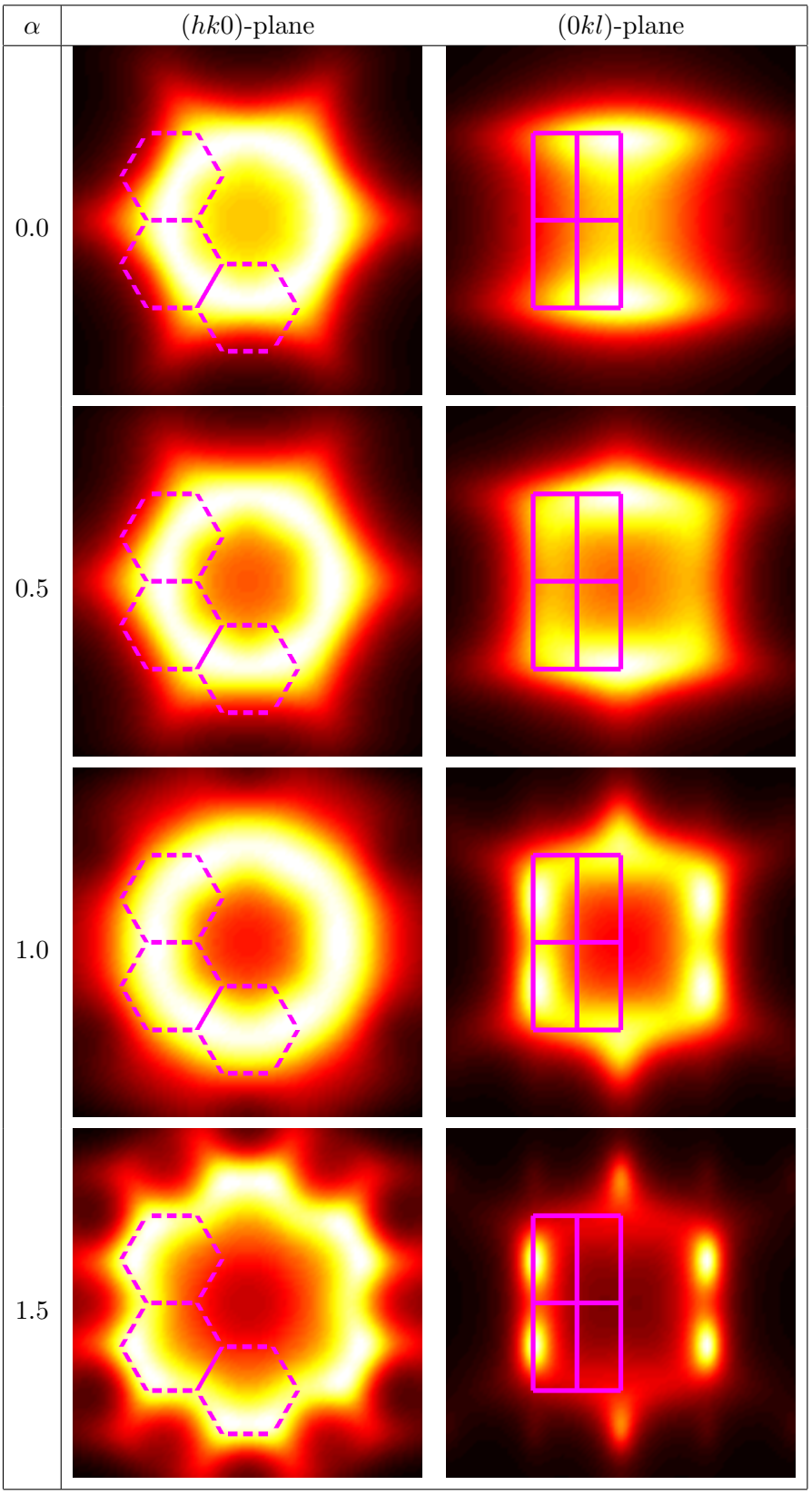


Figure 4.6: Structure factor in $(hk0)$- and $(0kl)$-planes calculated using the SCGA for various values of α, with $\beta J_1 S^2 = 1$. For the $(0kl)$-planes shown in the right column, the k-direction is vertical and the l-direction is horizontal. Dashed lines (left) show the Wigner-Seitz cells in reciprocal space and solid lines (right) show the reciprocal lattice. Plots include the magnetic form factor for Co^{2+} under the dipole approximation for spin-only scattering.

4.2 Effective interactions between kagome layers

In this section, we work out the effective interactions between the kagome spins in adjacent layers after integrating out the connecting spins in the triangular layers. We are able to integrate out all the triangular spins exactly, as each triangular spin can be integrated out independently of the others. Let $\mathbf{\Sigma}$ and $\mathbf{\Sigma'}$ be the sums of the three unit vectors representing classical spins in each of the two kagome triangles (in adjacent layers) that are coupled to a given apical spin, and let $\boldsymbol{\eta}$ be the unit vector for the apical spin. We wish to evaluate the apical spin's contribution to the partition function,

$$\mathcal{Z} = \int \mathrm{d}\boldsymbol{\eta} \, \exp\left[-\beta J_1 S^2 \alpha (\mathbf{\Sigma} + \mathbf{\Sigma'}) \cdot \boldsymbol{\eta}\right] \ .$$

To do so, we choose the zenith direction (z-axis) along the direction of $\mathbf{\Sigma} + \mathbf{\Sigma'}$, and perform the integration over the directions for $\boldsymbol{\eta}$ using spherical angles. We get

$$\mathcal{Z} \sim \frac{\sinh\left(\beta J_1 S^2 \alpha |\mathbf{\Sigma} + \mathbf{\Sigma'}|\right)}{|\mathbf{\Sigma} + \mathbf{\Sigma'}|} \ . \tag{4.29}$$

We can take $\mathcal{H}_{eff} \equiv -\log(\mathcal{Z})/\beta$ as an effective contribution to the Hamiltonian, which has the form

$$\mathcal{H}_{eff} \underset{\beta\to\infty}{\longrightarrow} -J_1 S^2 \alpha |\mathbf{\Sigma} + \mathbf{\Sigma'}| \tag{4.30}$$

at low T (large β). The effective interactions introduced by the apical spins are thus not standard exchange terms, and the natural oversimplification is to model these with ferromagnetic couplings between spins in adjacent kagome layers. In Chapter 6, we shall combine this insight with the SCGA approach to build a stochastic model for the low temperature spin dynamics, applying a technique pioneered by Conlon and Chalker for the pyrochlore lattice.[62]

CHAPTER 5

Spinwave dynamics

> Harmony makes small things grow, lack of it makes great things decay.
>
> — *Sallust*

Ordered magnetic states support spinwave excitations, which are Goldstone modes corresponding to broken spin rotation symmetry. These spinwave or magnon modes are analogous to phonon modes in crystals with ordered atomic positions. Such spinwaves are associated with a dispersion relation $\omega = \omega(\boldsymbol{Q})$, and knowing the dispersion relation can help determine the exchange parameters of the Hamiltonian when fit to data from inelastic magnetic neutron scattering. For frustrated magnets, there are no long-range ordered spin states in the classical spin liquid phase. Because the disordered ground state has no translational symmetry, crystal momentum is not a good quantum number and the excitations are not characterised by a dispersion relation.

Nonetheless, as Walker and Walsdedt realised for spin glasses,[55,56] we can still use linear spinwave theory as a numerical technique to study small-amplitude fluctuations around disordered ground states. In this chapter, we develop this numerical spinwave approach, following Walker and Walsdedt,[56] and apply it to the extended kagome lattice. We critically examine the usefulness of this technique by comparing our results with the experimental data on spin excitations from inelastic magnetic neutron scattering on an oxygen-rich single-crystal of $YBaCo_4O_7$. We are collaborating with R. I. Bewley and T. G. Perring from ISIS on the work in this chapter, and show some of their unpublished experimental data. Encouragingly, we find that the results of linear spinwave theory agree well with the scattering data over a wide range of wavevector and frequency.

5.1 Linear spinwave theory

The basic idea of spinwave theory is to transform spin operators into boson operators, using the Holstein-Primakoff transformation.[67] If we keep only the leading order terms in an $1/S$-expansion, we obtain a bosonic Hamiltonian that is *quadratic* in creation and annihilation operators, and *linear* equations of motion. Diagonalising this Hamiltonian into its normal modes allows us to approximate the low-lying excitations of the system as *independent bosons*. For this picture to be valid, the quantum spin fluctuations have to be small relative to the magnitude of the spin S, so that the classical ground state is a good approximation to the quantum ground state. We discuss this point further in Section 5.1.4 and Section 5.2.2.

5.1.1 Bosonic Hamiltonian

We start with the Hamiltonian for quantum Heisenberg spins,

$$\hat{\mathcal{H}} = \tfrac{1}{2} \sum_{i,j} J_{ij} \hat{\boldsymbol{S}}_i \cdot \hat{\boldsymbol{S}}_j \ . \tag{5.1}$$

At each of the N sites indexed by $i \in \{1, \ldots, N\}$, we introduce local axes as an orthogonal triad of unit vectors $\{\boldsymbol{x}_i, \boldsymbol{y}_i, \boldsymbol{z}_i\}$. We write the quantum spin operator at each site as

$$\begin{aligned} \hat{\boldsymbol{S}}_i &= \hat{S}_i^x \boldsymbol{x}_i + \hat{S}_i^y \boldsymbol{y}_i + \hat{S}_i^z \boldsymbol{z}_i \\ &= \tfrac{1}{\sqrt{2}} \hat{S}_i^- \boldsymbol{p}_i^+ + \tfrac{1}{\sqrt{2}} \hat{S}_i^+ \boldsymbol{p}_i^- + \hat{S}_i^z \boldsymbol{z}_i \ , \end{aligned} \tag{5.2}$$

where we define

$$\begin{cases} \boldsymbol{p}_i^{\pm} = \frac{1}{\sqrt{2}} (\boldsymbol{x}_i \pm i \boldsymbol{y}_i) \\ \hat{S}_i^{\pm} = \hat{S}_i^x \pm i \hat{S}_i^y \end{cases} \tag{5.3}$$

in the usual way. The Holstein-Primakoff transformation to bosonic operators $\{\hat{c}_i, \hat{c}_i^\dagger\}$ is given by

$$\begin{cases} \hat{S}_i^z = S_i - \hat{c}_i^\dagger \hat{c}_i \\ \hat{S}_i^+ = \sqrt{2S_i}\left[\left(1 - \dfrac{\hat{c}_i^\dagger \hat{c}_i}{2S_i}\right)^{1/2} \hat{c}_i\right] \approx \sqrt{2S_i}\,\hat{c}_i \\ \hat{S}_i^- = \sqrt{2S_i}\left[\hat{c}_i^\dagger \left(1 - \dfrac{\hat{c}_i^\dagger \hat{c}_i}{2S_i}\right)^{1/2}\right] \approx \sqrt{2S_i}\,\hat{c}_i^\dagger \ . \end{cases} \tag{5.4}$$

Now put Eq. (5.4) into Eq. (5.2) to get

$$\hat{\boldsymbol{S}}_i = S_i \boldsymbol{z}_i + S_i^{1/2}(\boldsymbol{p}_i^+ \hat{c}_i^\dagger + \boldsymbol{p}_i^- \hat{c}_i) - S_i^0 \boldsymbol{z}_i \hat{c}_i^\dagger \hat{c}_i + O(S_i^{-1/2}) \ , \tag{5.5}$$

and use this in Eq. (5.1) to get the bosonic Hamiltonian

$$\begin{aligned} \hat{\mathcal{H}} = {} & \tfrac{1}{2}\sum_{i,j} J_{ij} S_i S_j (\boldsymbol{z}_i \cdot \boldsymbol{z}_j) \\ & + \tfrac{1}{2}\sum_{i,j} J_{ij}\left[S_i S_j^{1/2} \boldsymbol{z}_i \cdot (\boldsymbol{p}_j^+ \hat{c}_j^\dagger + \boldsymbol{p}_j^- \hat{c}_j) + S_i^{1/2} S_j (\boldsymbol{p}_i^+ \hat{c}_i^\dagger + \boldsymbol{p}_i^- \hat{c}_i) \cdot \boldsymbol{z}_j\right] \\ & + \tfrac{1}{2}\sum_{i,j} J_{ij}\left[S_i^{1/2} S_j^{1/2} (\boldsymbol{p}_i^+ \hat{c}_i^\dagger + \boldsymbol{p}_i^- \hat{c}_i) \cdot (\boldsymbol{p}_j^+ \hat{c}_j^\dagger + \boldsymbol{p}_j^- \hat{c}_j) - S_i (\boldsymbol{z}_i \cdot \boldsymbol{z}_j) \hat{c}_j^\dagger \hat{c}_j - S_j (\boldsymbol{z}_i \cdot \boldsymbol{z}_j) \hat{c}_i^\dagger \hat{c}_i\right] \\ & + O(S^{1/2}) \ . \end{aligned} \tag{5.6}$$

We want to choose our local axes $\{\boldsymbol{z}_i\}$ in such a way that the linear terms in Eq. (5.6) vanish, leaving a quadratic Hamiltonian to leading order. As we shall see, this is accomplished by choosing $\{\boldsymbol{z}_i\}$ in the direction of the spins in a classical ground state.

5.1.2 Classical ground states

The classical spin Hamiltonian is

$$\mathcal{H} = \tfrac{1}{2}\sum_{i,j} J_{ij} \boldsymbol{S}_i \cdot \boldsymbol{S}_j \ , \tag{5.7}$$

where the classical vectors $\{\boldsymbol{S}_i\}$ are constrained to have length S_i. To minimise $\mathcal{H}$, we introduce Lagrange multipliers $\{L_i\}$, and consider instead the extremisation (without constraints) of the function

$$\mathcal{H}' = \tfrac{1}{2}\sum_{i,j} J_{ij} \boldsymbol{S}_i \cdot \boldsymbol{S}_j + \tfrac{1}{2}\sum_i L_i (\boldsymbol{S}_i \cdot \boldsymbol{S}_i - S_i^2) \ .$$

We see that a necessary condition for a local minimum of $\mathcal{H}$ is

$$-\sum_j J_{ij}\boldsymbol{S}_j = L_i\boldsymbol{S}_i \ , \text{ with all } L_i \geq 0 \ , \tag{5.8}$$

so that changing the direction of any spin increases the energy.

A classical ground state will thus satisfy Eq. (5.8). By defining the local axis $\boldsymbol{z}_i$ along the direction of $\boldsymbol{S}_i$ in a classical ground state, we have $-\sum_j J_{ij}S_j\boldsymbol{z}_j \propto \boldsymbol{z}_i$. For such a spin state, the linear terms in Eq. (5.6) vanish as a result, leaving a quadratic Hamiltonian that can be written in matrix form as

$$\hat{\mathcal{H}}_2 = \tfrac{1}{2}\begin{pmatrix} (\underline{\hat{c}}^\dagger)^\top & (\underline{\hat{c}})^\top \end{pmatrix}\begin{pmatrix} P & Q \\ Q^* & P^* \end{pmatrix}\begin{pmatrix} \underline{\hat{c}} \\ \underline{\hat{c}}^\dagger \end{pmatrix} \ , \tag{5.9}$$

where $\underline{\hat{c}}$ and $\underline{\hat{c}}^\dagger$ are the $N \times 1$ column vectors with elements $\{\hat{c}_i\}$ and $\{\hat{c}_i^\dagger\}$ respectively, and the $N \times N$ square matrices P and Q have elements

$$\begin{cases} P_{ij} = J_{ij}\sqrt{S_iS_j}(\boldsymbol{p}_i^+ \cdot \boldsymbol{p}_j^-) + \delta_{ij}L_jS_j \ , \\ Q_{ij} = J_{ij}\sqrt{S_iS_j}(\boldsymbol{p}_i^+ \cdot \boldsymbol{p}_j^+) \ . \end{cases} \tag{5.10}$$

Note that $P = P^\dagger$ is Hermitian and $Q = Q^\top$ is symmetric.

5.1.3 Equations of motion and normal modes

In a classical ground state, the equations of motion Eq. (1.4) for the bosonic operators are

$$\begin{cases} i\hbar\dfrac{d\hat{c}_k}{dt} = [\hat{c}_k, \hat{\mathcal{H}}_2] \\ i\hbar\dfrac{d\hat{c}_k^\dagger}{dt} = [\hat{c}_k^\dagger, \hat{\mathcal{H}}_2] \ . \end{cases}$$

Using the bosonic commutation relations

$$\begin{cases} [\hat{c}_i, \hat{c}_j] = 0 = [\hat{c}_i^\dagger, \hat{c}_j^\dagger] \\ [\hat{c}_i, \hat{c}_j^\dagger] = \delta_{ij} \ , \end{cases}$$

we end up with

$$\begin{cases} \dfrac{d\hat{c}_k}{dt} = \dfrac{-i}{\hbar}\displaystyle\sum_j P_{kj}\hat{c}_j + Q_{kj}\hat{c}_j^\dagger \\ \dfrac{d\hat{c}_k^\dagger}{dt} = \dfrac{i}{\hbar}\displaystyle\sum_j Q_{kj}^*\hat{c}_j + P_{kj}^*\hat{c}_j^\dagger \ . \end{cases}$$

We can write these linear equations in matrix form as

$$\frac{d}{dt}\begin{pmatrix} \hat{\underline{c}} \\ \hat{\underline{c}}^\dagger \end{pmatrix} = i\mathcal{F}\begin{pmatrix} \hat{\underline{c}} \\ \hat{\underline{c}}^\dagger \end{pmatrix} \quad \text{with} \quad \mathcal{F} = \frac{1}{\hbar}\begin{pmatrix} -P & -Q \\ Q^* & P^* \end{pmatrix} . \tag{5.11}$$

To diagonalise the equations of motion, we perform a Bogoliubov transformation so that operators in the new basis also obey the bosonic commutation relations. Writing the transformation as

$$\begin{pmatrix} \hat{\underline{c}} \\ \hat{\underline{c}}^\dagger \end{pmatrix} = \begin{pmatrix} g^* & f \\ f^* & g \end{pmatrix}\begin{pmatrix} \hat{\underline{d}} \\ \hat{\underline{d}}^\dagger \end{pmatrix} , \tag{5.12}$$

requiring that the new operators are also bosonic imposes constraints on the transformation matrices f and g,

$$\begin{cases} g^* f^\top - f g^\dagger = 0 , \\ g^* g^\top - f f^\dagger = \mathbb{1} . \end{cases} \tag{5.13}$$

From Eq. (5.13), the inverse transformation is

$$\begin{pmatrix} g^* & f \\ f^* & g \end{pmatrix}^{-1} = \begin{pmatrix} g^\top & -f^\top \\ -f^\dagger & g^\dagger \end{pmatrix} , \tag{5.14}$$

since we have

$$\begin{pmatrix} g^* & f \\ f^* & g \end{pmatrix}\begin{pmatrix} g^\top & -f^\top \\ -f^\dagger & g^\dagger \end{pmatrix} = \mathbb{1} = \begin{pmatrix} g^\top & -f^\top \\ -f^\dagger & g^\dagger \end{pmatrix}\begin{pmatrix} g^* & f \\ f^* & g \end{pmatrix} . \tag{5.15}$$

Thus the constraints Eq. (5.13) on the transformation matrices are equivalently given by

$$\begin{cases} g^\top f - f^\top g = 0 , \\ g^\dagger g - f^\dagger f = \mathbb{1} . \end{cases} \tag{5.16}$$

The new operators are chosen to diagonalise our Hamiltonian, so that

$$\hat{\mathcal{H}}_2 = \sum_\nu \hbar\omega_\nu \hat{d}_\nu^\dagger \hat{d}_\nu + \text{constant term} \tag{5.17}$$

is a linear combination of the number operators $\hat{n}_\nu \equiv \hat{d}_\nu^\dagger \hat{d}_\nu$. If the ground state is stable, the frequencies $\{\omega_\nu\}$ are all real. This stability is equivalent to having *all non-negative*

eigenvalues of the energy matrix

$$\mathcal{M} = \begin{pmatrix} P & Q \\ Q^* & P^* \end{pmatrix} \tag{5.18}$$

in the quadratic Hamiltonian Eq. (5.9). We examine this point about stability in greater detail in Section 5.2.2.

It is easy to work out the time-evolution of the system with a diagonal Hamiltonian Eq. (5.17). In the Heisenberg picture, the time-evolution of an operator $\hat{A}(t)$ is given by

$$\hat{A}(t) = e^{i\hat{\mathcal{H}}_2 t/\hbar} \hat{A} e^{-i\hat{\mathcal{H}}_2 t/\hbar} ,$$

where $\hat{A}$ is the operator at $t = 0$. For the boson operators, we can expand the exponentials as power series and use the bosonic commutation relations to see that

$$\begin{cases} \hat{d}_\nu(t) = \hat{d}_\nu e^{-i\omega_\nu t} , \\ \hat{d}^\dagger_\nu(t) = \hat{d}^\dagger_\nu e^{+i\omega_\nu t} . \end{cases} \tag{5.19}$$

Letting Ω be the $N \times N$ diagonal matrix with $\{\omega_\nu\}$ along the diagonal, we can express the equations of motion as

$$\frac{d}{dt} \begin{pmatrix} \underline{\hat{d}} \\ \underline{\hat{d}}^\dagger \end{pmatrix} = i \begin{pmatrix} -\Omega & 0 \\ 0 & +\Omega \end{pmatrix} \begin{pmatrix} \underline{\hat{d}} \\ \underline{\hat{d}}^\dagger \end{pmatrix} . \tag{5.20}$$

Comparing Eq. (5.11) and Eq. (5.20), we see that we expect the eigenvalues of the *frequency matrix* $\mathcal{F}$ to come in pairs $\{\pm\omega_\nu\}$, and the diagonalisation procedure can be written as

$$\mathcal{F} = V \begin{pmatrix} -\Omega & 0 \\ 0 & +\Omega \end{pmatrix} V^{-1} . \tag{5.21}$$

The proper normalisation of the eigenvectors is obtained by requiring that

$$V = \begin{pmatrix} g^* & f \\ f^* & g \end{pmatrix} ,$$

with the matrices f and g obeying the constraints Eq. (5.16).

5.1.4 Ground state moments

Quantum fluctuations can destabilise the classical ground state, so it is important to estimate this effect. We calculate deviations from the classical ground state by calculating the average over spins of the expectation value

$$\frac{1}{N}\sum_i \langle \hat{S}_i^z \rangle = \left(\frac{1}{N}\sum_i S_i \right) - \Delta S \ , \tag{5.22}$$

where we see from Eq. (5.4) that

$$\Delta S = \frac{1}{N}\sum_i \langle \hat{c}_i^\dagger \hat{c}_i \rangle \ . \tag{5.23}$$

This quantity determines the fluctuations from the classical ground state, and we want to see how this behaves in the thermodynamic limit.

The thermal expectation value of operators that do not conserve the boson number is zero, since the Hamiltonian Eq. (5.17) is expressed in terms of the number operators $\{\hat{n}_\nu\}$ of the $\{\hat{d}_\nu, \hat{d}_\nu^\dagger\}$ bosons. Using the Bogoliubov transformation Eq. (5.12), we thus find that

$$\Delta S = \frac{1}{N}\sum_{i,\nu} \left(|f_{i\nu}|^2 \langle \hat{d}_\nu \hat{d}_\nu^\dagger \rangle + |g_{i\nu}|^2 \langle \hat{d}_\nu^\dagger \hat{d}_\nu \rangle \right) \ . \tag{5.24}$$

The thermal occupation number for each mode is drawn from the Planck distribution, and we set

$$\begin{cases} \langle \hat{d}_\nu^\dagger \hat{d}_{\nu'} \rangle = \delta_{\nu,\nu'} n(\omega_\nu) \\ \langle \hat{d}_\nu \hat{d}_{\nu'}^\dagger \rangle = \delta_{\nu,\nu'} [1 + n(\omega_\nu)] \ , \end{cases} \tag{5.25}$$

where $n(\omega) = (e^{\hbar\omega/k_B T} - 1)^{-1}$. At zero temperature, we have $n(\omega_\nu) = 0$ for all modes, and Eq. (5.24) becomes

$$\Delta S_{(T=0)} = \frac{1}{N}\sum_{i,\nu} |f_{i\nu}|^2 \ . \tag{5.26}$$

We will estimate this value numerically in Section 5.2.2. If $\Delta S_{(T=0)}$ is comparable to the spin S, then quantum fluctuations destabilise the classical ground state.

5.1.5 Dynamic structure factor

To calculate the dynamic structure factor, we first write the time-dependent spin correlation function in terms of the boson operators, then take the thermal expectation value and

Fourier transform in space and time.

Using Eq. (5.5) for the spin operator and dropping terms of cubic and higher order in the boson operators, we have

$$\begin{aligned}\hat{\boldsymbol{S}}_i(0)\cdot\hat{\boldsymbol{S}}_j(t) = {} & S_iS_j(\boldsymbol{z}_i\cdot\boldsymbol{z}_j)\\ & + S_iS_j^{1/2}\left\{\boldsymbol{z}_i\cdot\left[\boldsymbol{p}_j^+\hat{c}_j^\dagger(t)+\boldsymbol{p}_j^-\hat{c}_j(t)\right]\right\} + S_i^{1/2}S_j\left\{\left[\boldsymbol{p}_i^+\hat{c}_i^\dagger(0)+\boldsymbol{p}_i^-\hat{c}_i(0)\right]\cdot\boldsymbol{z}_j\right\}\\ & + \left[-S_j\hat{c}_i^\dagger(0)\hat{c}_i(0) - S_i\hat{c}_j^\dagger(t)\hat{c}_j(t)\right](\boldsymbol{z}_i\cdot\boldsymbol{z}_j)\\ & + S_i^{1/2}S_j^{1/2}\left\{\left[\boldsymbol{p}_i^+\hat{c}_i^\dagger(0)+\boldsymbol{p}_i^-\hat{c}_i(0)\right]\cdot\left[\boldsymbol{p}_j^+\hat{c}_j^\dagger(t)+\boldsymbol{p}_j^-\hat{c}_j(t)\right]\right\}\\ & + O(S^{1/2})\,. \end{aligned} \tag{5.27}$$

We use the Bogoliubov transformation Eq. (5.12), and only terms that conserve boson number remain in the thermal expectation value. Including the time-evolution from Eq. (5.19) and populating modes using Eq. (5.25), we get

$$\begin{aligned}\langle\hat{\boldsymbol{S}}_i(0)\cdot\hat{\boldsymbol{S}}_j(t)\rangle = \sqrt{S_iS_j}\Bigg\{ & \sum_\nu e^{+i\omega_\nu t}[1+n(\omega_\nu)](f_{i\nu}^*\boldsymbol{p}_i^+ + g_{i\nu}^*\boldsymbol{p}_i^-)\cdot(g_{j\nu}\boldsymbol{p}_j^+ + f_{j\nu}\boldsymbol{p}_j^-)\\ & + \sum_\nu e^{-i\omega_\nu t}[n(\omega_\nu)](g_{i\nu}\boldsymbol{p}_i^+ + f_{i\nu}\boldsymbol{p}_i^-)\cdot(f_{j\nu}^*\boldsymbol{p}_j^+ + g_{j\nu}^*\boldsymbol{p}_j^-)\Bigg\}\\ & + \text{time-independent term} + O(S^0)\,. \end{aligned} \tag{5.28}$$

We define the Fourier transform in time as

$$S(\boldsymbol{r}_{ij},\omega) \equiv \frac{1}{2\pi}\int_{-\infty}^{\infty} dt\, e^{-i\omega t}\langle\hat{\boldsymbol{S}}_i(0)\cdot\hat{\boldsymbol{S}}_j(t)\rangle\,.$$

The time-independent term in $\langle\hat{\boldsymbol{S}}_i(0)\cdot\hat{\boldsymbol{S}}_j(t)\rangle$ will give a term proportional to $\delta(\omega)$, so we have

$$\begin{aligned}S(\boldsymbol{r}_{ij},\omega) = \sqrt{S_iS_j}\Bigg\{ & \sum_\nu \delta(\omega-\omega_\nu)[1+n(\omega_\nu)](f_{i\nu}^*\boldsymbol{p}_i^+ + g_{i\nu}^*\boldsymbol{p}_i^-)\cdot(g_{j\nu}\boldsymbol{p}_j^+ + f_{j\nu}\boldsymbol{p}_j^-)\\ & + \sum_\nu \delta(\omega+\omega_\nu)[n(\omega_\nu)](g_{i\nu}\boldsymbol{p}_i^+ + f_{i\nu}\boldsymbol{p}_i^-)\cdot(f_{j\nu}^*\boldsymbol{p}_j^+ + g_{j\nu}^*\boldsymbol{p}_j^-)\Bigg\}\\ & + \delta(\omega)\text{ term} + O(S^0)\,. \end{aligned} \tag{5.29}$$

In the ground state, all modes are unoccupied, so the terms with $\delta(\omega+\omega_\nu)$ vanish in the $T\to 0$ limit. Thus we identify the $\delta(\omega-\omega_\nu)$ terms, with support on $\omega>0$, as corresponding to processes where the spin system *gains energy* from scattered neutrons. At very low

temperatures, these are the terms that are experimentally relevant.

Now we take the spatial Fourier transform, since

$$S(\boldsymbol{Q},\omega) = \frac{1}{N}\sum_{i,j} e^{-i\boldsymbol{Q}\cdot(\boldsymbol{r}_i-\boldsymbol{r}_j)} S(\boldsymbol{r}_{ij},\omega) \ ,$$

where $\boldsymbol{r}_i$ is the position vector of the spin $\hat{\boldsymbol{S}}_i$. We see that for $\omega > 0$, we have

$$S(\boldsymbol{Q},\omega>0) = \left\{ \sum_{\nu} \delta(\omega-\omega_\nu)[1+n(\omega_\nu)] \left|\boldsymbol{\rho}_\nu(\boldsymbol{Q})\right|^2 \right\} + O(S^0) \ , \tag{5.30}$$

where

$$\boldsymbol{\rho}_\nu(\boldsymbol{Q}) = \frac{1}{\sqrt{N}} \sum_i e^{-i\boldsymbol{Q}\cdot\boldsymbol{r}_i} \sqrt{S_i} (f^*_{i\nu}\boldsymbol{p}_i^+ + g^*_{i\nu}\boldsymbol{p}_i^-) \ . \tag{5.31}$$

The structure factor calculated in this way can be visualised as colour plots, which we will do in Section 5.2. We will compare these plots with the magnetic scattering amplitudes obtained from inelastic neutron scattering in Section 5.3.

5.1.6 Spin autocorrelation function

The dynamic structure factor Eq. (5.30) gives a lot of information about spin excitations in the low temperature regime, and is especially interesting because it provides a detailed description of the system that allows for strong contact with neutron scattering experiments. The spin autocorrelation function is another way to characterise the system dynamics, and is interesting from the theoretical perspective as a measure of how the spin configuration evolves. In Chapter 6 and Chapter 7, we study the spin autocorrelation using other analytical and numerical techniques.

In this subsection, we will work out the spin autocorrelation function from linear spinwave theory. The results of the numerical computation are shown in comparison with molecular dynamics simulations in Section 7.2.1. Because spinwaves describe small-amplitude fluctuations away from a classical ground state, we expect this comparison to work out reasonably well for short times, but not at longer times where the dynamics are likely governed by larger movements between ground states. We have to be in the classical regime to make a reasonable comparison with the molecular dynamics simulations

for classical spins. This means that the spinwave modes are all highly occupied, with

$$\hbar\omega_\nu \ll k_B T \ , \text{ and thus } \ n(\omega_\nu) = \frac{k_B T}{\hbar\omega_\nu} + O(1) \gg 1 \ \text{ for each } \nu \ . \tag{5.32}$$

Note that because the quadratic Hamiltonian Eq. (5.9) is of order $J_1 S$, the classical regime Eq. (5.32) can be compatible, for large spin-length $S \gg 1$, with our interest in the low temperature regime for molecular dynamics, in which $k_B T \ll J_1 S^2$. Within the classical approximation, we thus have

$$\begin{aligned}\langle \boldsymbol{S}_i(0) \cdot \boldsymbol{S}_i(t) \rangle = S_i \frac{k_B T}{\hbar} \sum_\nu \left(|f_{i\nu}|^2 + |g_{i\nu}|^2 \right) \frac{2\cos(\omega_\nu t)}{\omega_\nu} \\ + \text{time-independent term} + O(S_i^0) \ ,\end{aligned} \tag{5.33}$$

from putting Eq. (5.32) into Eq. (5.28) with $j = i$.

As we are dealing with classical spins, we put equal spin $S_i = S \gg 1$ at all sites. The spin autocorrelation function averaged over all N sites is

$$A(t) = \frac{1}{N} \sum_i \langle \boldsymbol{S}_i(0) \cdot \boldsymbol{S}_i(t) \rangle \ .$$

From Eq. (5.33), the time-dependence of $A(t)$ can be written as

$$A(t) = A(0) + S \, \frac{k_B T}{\hbar} \left[G(t) - G(0) \right] \ , \tag{5.34}$$

where

$$G(t) \equiv \frac{1}{N} \sum_i \sum_\nu \left(|f_{i\nu}|^2 + |g_{i\nu}|^2 \right) \frac{2\cos(\omega_\nu t)}{\omega_\nu} \ . \tag{5.35}$$

Thus, linear spinwave theory for classical spins predicts that the decay of the spin autocorrelation Eq. (5.34) is *proportional to the temperature*. Normalising the spin autocorrelation so that it has a starting value of unity, we define

$$\mathcal{A}(t) \equiv \frac{A(t)}{A(0)} \ .$$

In this way, for $S \gg 1$, we have

$$\mathcal{A}(t) = 1 - \frac{k_B T}{J_1 S^2} [\mathcal{G}(t)] \ , \tag{5.36}$$

where the time-dependent decay function is

$$\mathcal{G}(t) \equiv \frac{2}{N} \sum_i \sum_\nu \left(|f_{i\nu}|^2 + |g_{i\nu}|^2 \right) \left(\frac{J_1 S/\hbar}{\omega_\nu} \right) \left[1 - \cos(\omega_\nu t) \right] . \tag{5.37}$$

Note that we can similarly define the average over kagome sites only, or over triangular lattice sites only, by simply taking the sum i in Eq. (5.37) over the desired sites (and dividing by the reduced number of sites instead of by N).

5.2 Spinwave simulations

In this section, we describe the results of spinwave simulations for the extended kagome lattice. To calculate the dynamic structure factor $S(\boldsymbol{Q}, \omega)$ using Eq. (5.30), we make the zero-temperature approximation that all normal modes are unoccupied. Corrections for finite temperature increase the weighting of lower energy modes and do not affect the $\boldsymbol{Q}$-space patterns for each mode.

As discussed in Section 2.1.4, the spin on the kagome and triangular sites could be different. We first present results for equal spin on all sites and only vary the ratio $\alpha = J_2/J_1$ in this section. For the comparison with experimental data in Section 5.3, we also look at the dependence on $\sigma = S_t/S_k$ by varying α and σ inversely while keeping the product $\alpha\sigma$ constant. This additional variable makes qualitative changes to the scattering patterns, which further improves the fit with experiments, as we shall see.

5.2.1 Simulation details

In our simulations, we used a system of 1024 spins in $4 \times 4 \times 8$ unit cells of 8 spins each, with periodic boundary conditions imposed. The full 8-site unit cell in the hexagonal lattice system is the one shown in Fig. 3.2. We chose to simulate more layers to increase resolution in the direction normal to the layers. The results were averaged over five spin configurations each time.

The classical ground states discussed in Section 5.1.2 were obtained numerically, using Metropolis Monte Carlo and repeated alignment of spins with their local field as described in Section 3.1.3, except that this time the triangular lattice spins were not kept fixed and were also similarly moved. If the classical spin configuration is at a true local minimum

of energy, all eigenvalues of the energy matrix $\mathcal{M}$ in Eq. (5.18) should be non-negative. However, we generally find some small negative eigenvalues for the numerical ground states, which we discuss in more detail in Section 5.2.2. It is important to ensure the ground state stability so that the normal mode frequencies are all real. We add a small *shattered field* term to the Hamiltonian by replacing

$$\mathcal{M} \to \mathcal{M} + \epsilon \mathbb{1} \,, \tag{5.38}$$

and find empirically that $\epsilon \lesssim 10^{-5} \cdot J_1 S$ is sufficient to make all frequencies real, assuring us that our numerical spin configurations are reasonably close to a true ground state.

The diagonalisation of the frequency matrix $\mathcal{F}$ in Eq. (5.21) is done numerically using MATLAB. We sort the eigenvalues so that the negative eigenvalues all come first, and construct the diagonal matrix Ω from the absolute values of these N eigenvalues indexed by ν. The eigenvectors are returned as vectors $U_\nu(i)$. For the first N eigenvectors corresponding to these negative eigenvalues, we scale each eigenvector by $1/N_\nu$, where

$$N_\nu = \sqrt{\sum_{i=1}^{N} \left(\left|U_\nu(i)\right|^2 - \left|U_\nu(i+N)\right|^2 \right)} \,.$$

We then use these scaled eigenvectors to construct the $N \times N$ matrices f and g for the Bogoliubov transformation. This procedure ensures that the diagonal elements of $g^\dagger g - f^\dagger f$ satisfy Eq. (5.16). We then check numerically that the other constraints in Eq. (5.16) are satisfied, and that the original matrix can be reconstructed, i.e.,

$$\mathcal{F} = \begin{pmatrix} g^* & f \\ f^* & g \end{pmatrix} \begin{pmatrix} -\Omega & 0 \\ 0 & +\Omega \end{pmatrix} \begin{pmatrix} g^\top & -f^\top \\ -f^\dagger & g^\dagger \end{pmatrix} \,. \tag{5.39}$$

5.2.2 Stability of ground states

In this subsection, we first look at the classical stability of the numerical ground states. We do this by studying the eigenvalues (called *stiffnesses*) of the energy matrix $\mathcal{M}$ in Eq. (5.18), as all stiffnesses must be non-negative for the state to be a local minimum of energy. We describe how we can count the number of zero modes, and numerically verify the formula Eq. (3.9) for the classical ground state dimension from Maxwell counting. We then look at the stability of the classical ground states against quantum fluctuations.

We generate numerical ground states for $L\times L\times M$ unit cells of 8 spins each, with periodic boundary conditions imposed. For each value of $L \in \{2, 3, \ldots, 6\}$, we put $M = 1, 2, \ldots, 6$ and numerically diagonalised the energy matrix $\mathcal{M}$ associated with each state to obtain the stiffnesses. The magnitude of the shattered field required in Eq. (5.38) to ensure classical stability is given by the smallest (most negative) stiffness.

We can count the number of zero modes for a numerical ground state by plotting the absolute values of the stiffnesses on a logarithmic scale to identify the distinguishing sharp jump between zero modes and soft modes. We found that the number of zero modes for all of these systems was given by

$$N_{zero} = 2L^2 + 6M - 3\ . \tag{5.40}$$

For example, we identify exactly 105 zero modes for a 1,728 spins system with $6\times 6\times 6$ unit cells (see Fig. 5.1). These simulations numerically verify the Maxwell counting argument in Section 3.1.2, as we see that $N_{zero} = D_{pbc}$, where D_{pbc} is the ground state dimension Eq. (3.9) obtained from Maxwell counting, for a system with periodic boundary conditions.

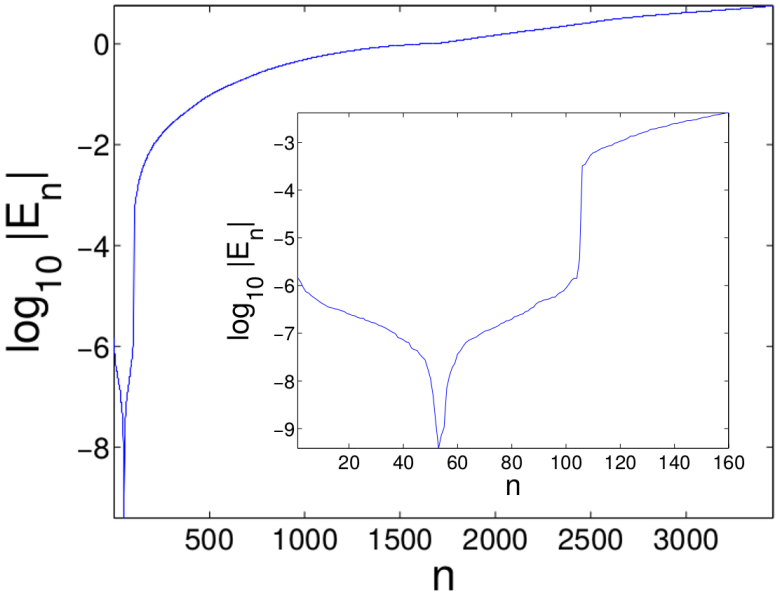


Figure 5.1: Logarithm (base 10) of the absolute values of the eigenvalues E_n (sorted in ascending order) of the energy matrix $\mathcal{M}$ in Eq. (5.18) for a numerical ground state of a system with 1,728 spins ($6\times 6\times 6$ unit cells). We set $\alpha = J_2/J_1 = \frac{1}{2}$. *(Inset):* The same plot for only the lowest 160 eigenvalues, showing the sharp jump in energy after the 105^{th} eigenvalue.

As discussed in Section 5.1.4, we want to see how large the quantum fluctuations are at zero temperature. To do so, we calculate $\Delta S_{(T=0)}$ in Eq. (5.26) for a variety of systems,

with different numbers of spins N in various geometries, to try to extrapolate the limit for large systems. In making this calculation, we exclude the contribution from the N_{zero} zero modes, since they form a vanishing fraction of the total number of modes in the thermodynamic limit. We plot $\Delta S_{(T=0)}$ against $1/N$ in Fig. 5.2. We see that the system will be quantum disordered for $S = \frac{1}{2}$, but the situation is unclear for large S. It is hard to decide this without more analytical understanding, although the results may be compatible with stability of the classical state.

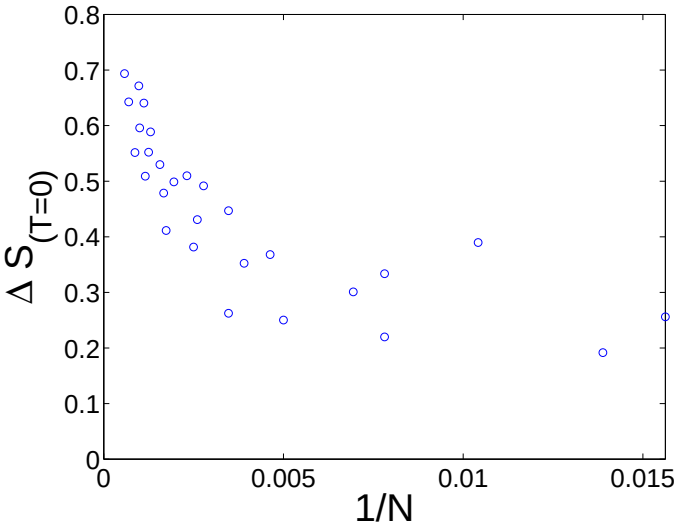


Figure 5.2: Zero temperature quantum fluctuations Eq. (5.26), for numerical ground states ranging in size from $N = 64$ to 1,728 spins. We set $\alpha = J_2/J_1 = \frac{1}{2}$.

5.2.3 Distribution of frequency modes

The distribution of normal mode frequencies from numerical diagonalisation of Eq. (5.21) is shown in Fig. 5.3 for a range of α, with $\sigma = 1$. We notice that for $\alpha < \frac{3}{2}$, the distributions have a peak at zero frequency, which is consistent with the divergent ground state dimension discussed in Section 3.1.2. For smaller α, the frequencies are otherwise quite well distributed up to a cut-off value, whereas for $\alpha \gtrsim 1$, there are significant dips and peaks in the frequency distribution at higher frequencies.

5.2.4 Plots of dynamic structure factor

We show the results of the simulations of $S(\boldsymbol{Q}, \omega)$ using Eq. (5.30). The dynamic structure factor is visualised as colour plots for the $(h0l)$ and $(hk\bar{2})$ reciprocal lattice planes, at

successive energy slices. The slices were produced by distributing the frequencies equally into consecutive ranges. The plots for the $(h0l)$ plane are shown in Fig. 5.4 and the plots for the $(hk\bar{2})$ plane are shown in Fig. 5.5. In our simulations, we fixed $\sigma = 1$ and varied $\alpha \in \{0.50, 0.75, 1.00, 1.25\}$. While there is a vast amount of data encoded in each of these figures, the most important point to note is that the plots change significantly across the rows and columns. This indicates firstly that the scattering patterns at different energies are different, and secondly that changing α changes the patterns as well.

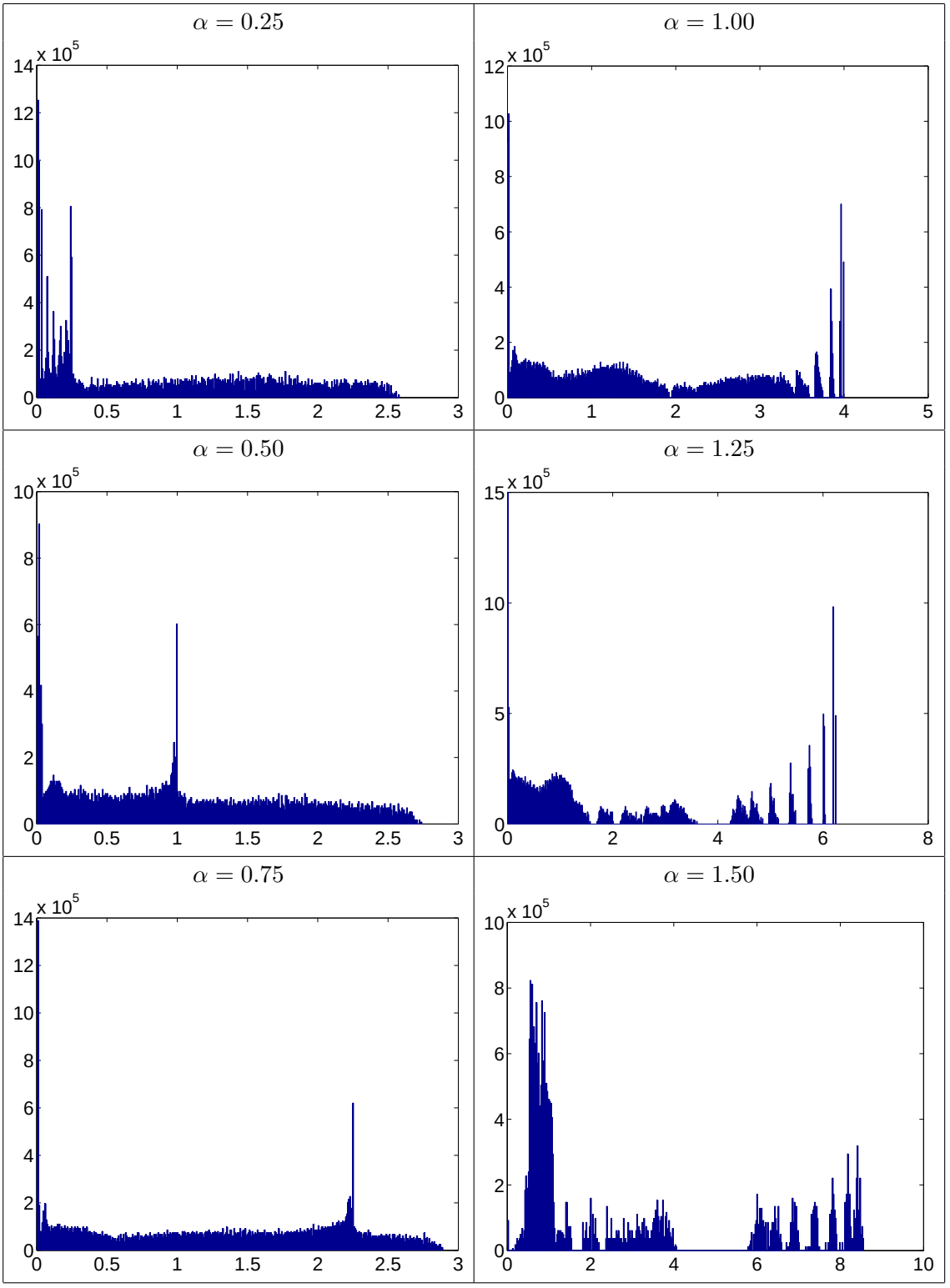


Figure 5.3: Distribution of mode frequencies (measured in units of $J_1 S/\hbar$) from numerical diagonalisation of Eq. (5.21). We put the same spin S at all sites so $\sigma = 1$ and only vary α.

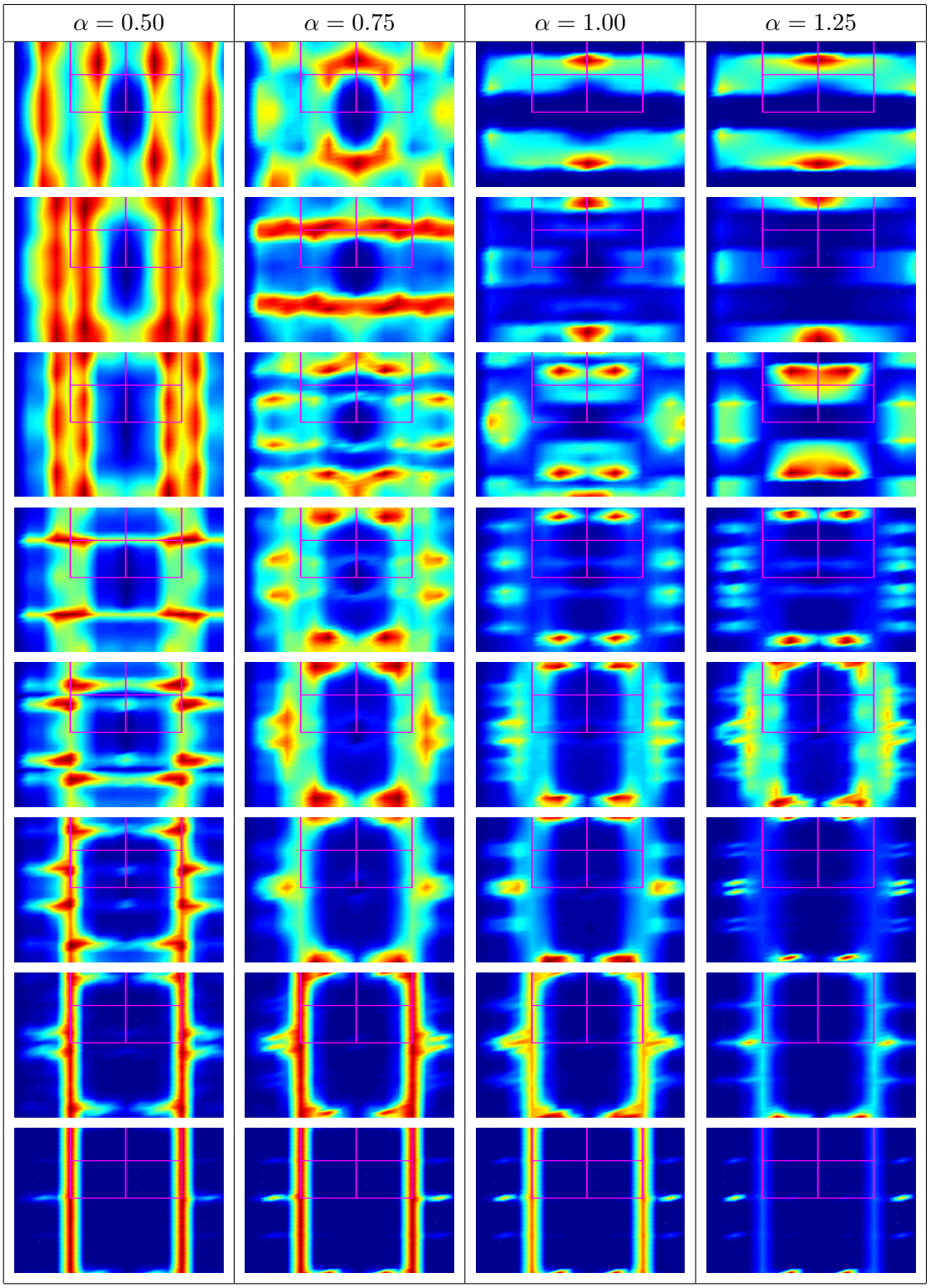


Figure 5.4: Structure factor in $(h0l)$ plane for $\alpha \in \{0.50, 0.75, 1.00, 1.25\}$ with $\sigma = 1$. Lowest energy slices are at the bottom, and highest ones at the top. Solid lines show the reciprocal lattice.

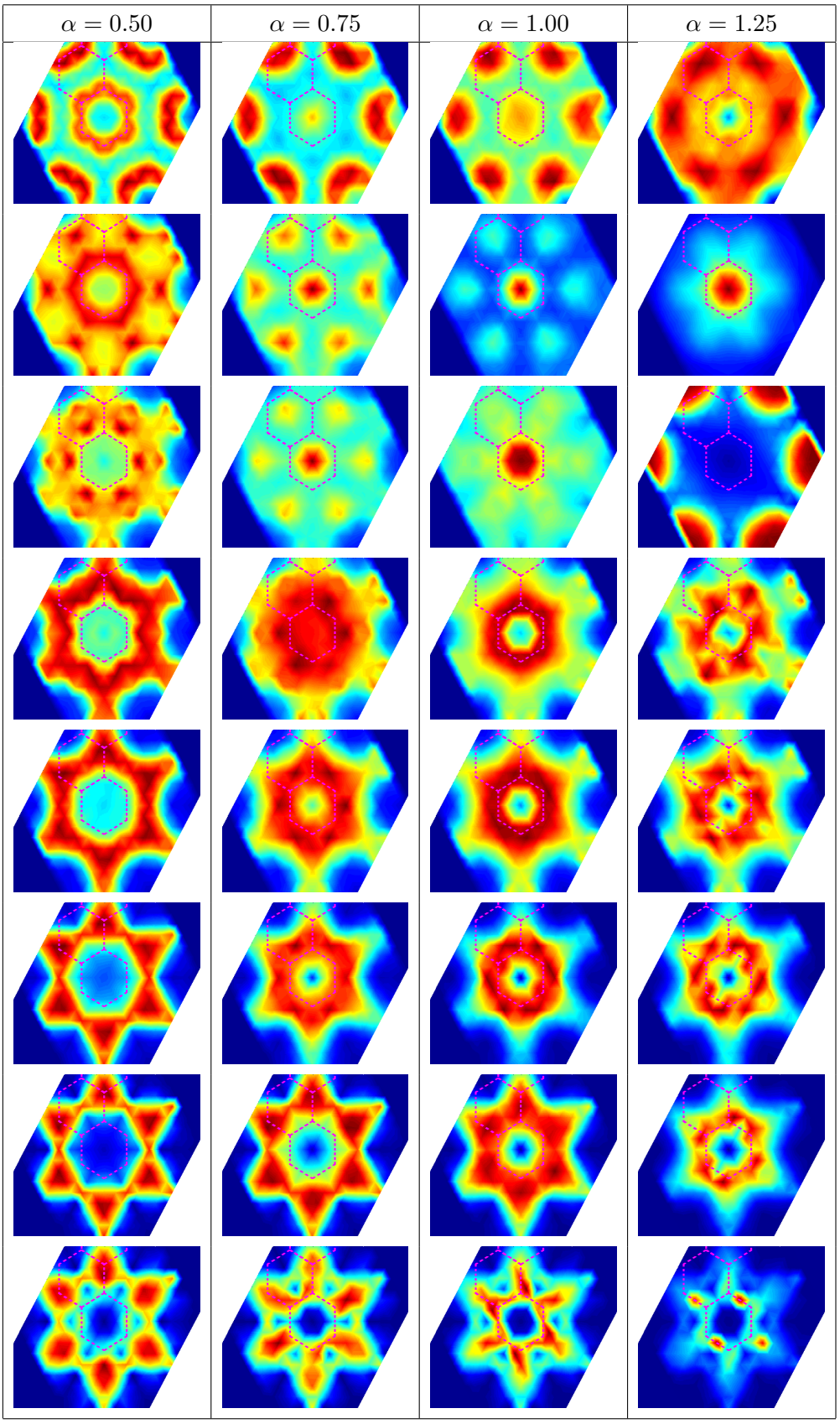


Figure 5.5: Structure factor in $(hk\bar{2})$ plane for $\alpha \in \{0.50, 0.75, 1.00, 1.25\}$ with $\sigma = 1$. Lowest energy slices are at the bottom, and highest ones at the top. Dashed lines show the Wigner-Seitz cells in reciprocal space.

5.3 Comparison with experiments

Comparing our simulation results with the experimental data suggest values for α and σ. With $\sigma = 1$, the value of $\alpha = 1$ seemed to provide the best qualitative visual fit to the neutron scattering patterns. In this section, we attempt to improve the fit by subsequently varying σ.

5.3.1 Varying σ with $\alpha\sigma$ constant

Following from the discussion in Section 2.1.4, if we assume the 3 Co^{2+}:1 Co^{3+} ratio for the oxygen-stoichiometric $YBaCo_4O_7$, and that the Co^{3+} ions ($S = 2$) are all on the triangular lattice sites, leaving only Co^{2+} ions ($S = \frac{3}{2}$) on the kagome sites, we would have $\sigma = \frac{4}{3}$. On the other hand, if the ratio is 2.3 Co^{2+}:1 Co^{3+} for oxygen-rich $YBaCo_4O_{7.1}$, the value of σ could be as low as 0.88. In this section, we simulate the effect of $\sigma = \frac{4}{3}$ and also $\sigma = \frac{3}{4}$ (even though this latter value is probably too low), with $\alpha\sigma = 1$ fixed. The idea is to see how the patterns change, and if a better fit to the experimental data is obtained. Keeping $\alpha\sigma$ constant means that the classical ground state spin configurations are similar.

We plot $S(\boldsymbol{Q}, \omega)$ using Eq. (5.30). Results for the $(h0l)$ plane are shown in Fig. 5.6, and results for the $(hk\bar{2})$ plane are shown in Fig. 5.7. In addition, plots along the $(\frac{1}{2}, 0, l)$, $(\frac{3}{2}, 0, l)$ and $(h, 0, \bar{2})$ lines in reciprocal space, for all energies, are shown in Fig. 5.8. For these latter plots, where intensities at different energies are plotted together, we use a logarithmic scale to accentuate the higher energy features, which are otherwise too weak to discern.

5.3.2 Data from inelastic magnetic neutron scattering

The results from Section 5.3.1 show that even though $\alpha\sigma = 1$ is fixed, changing σ results in some changes to the plots. Our preliminary conclusion based on comparing our spinwave results with experimental data from neutron scattering is that $\sigma > 1$.

We now show the experimental data alongside the simulations for $\alpha = \frac{3}{4}, \sigma = \frac{4}{3}$, this time including a magnetic form factor correction for our simulated results. As in Section 4.1.5, we apply the magnetic form factor in these plots based on Co^{2+} ions only, under the dipole approximation for spin-only scattering. The experimental data provided

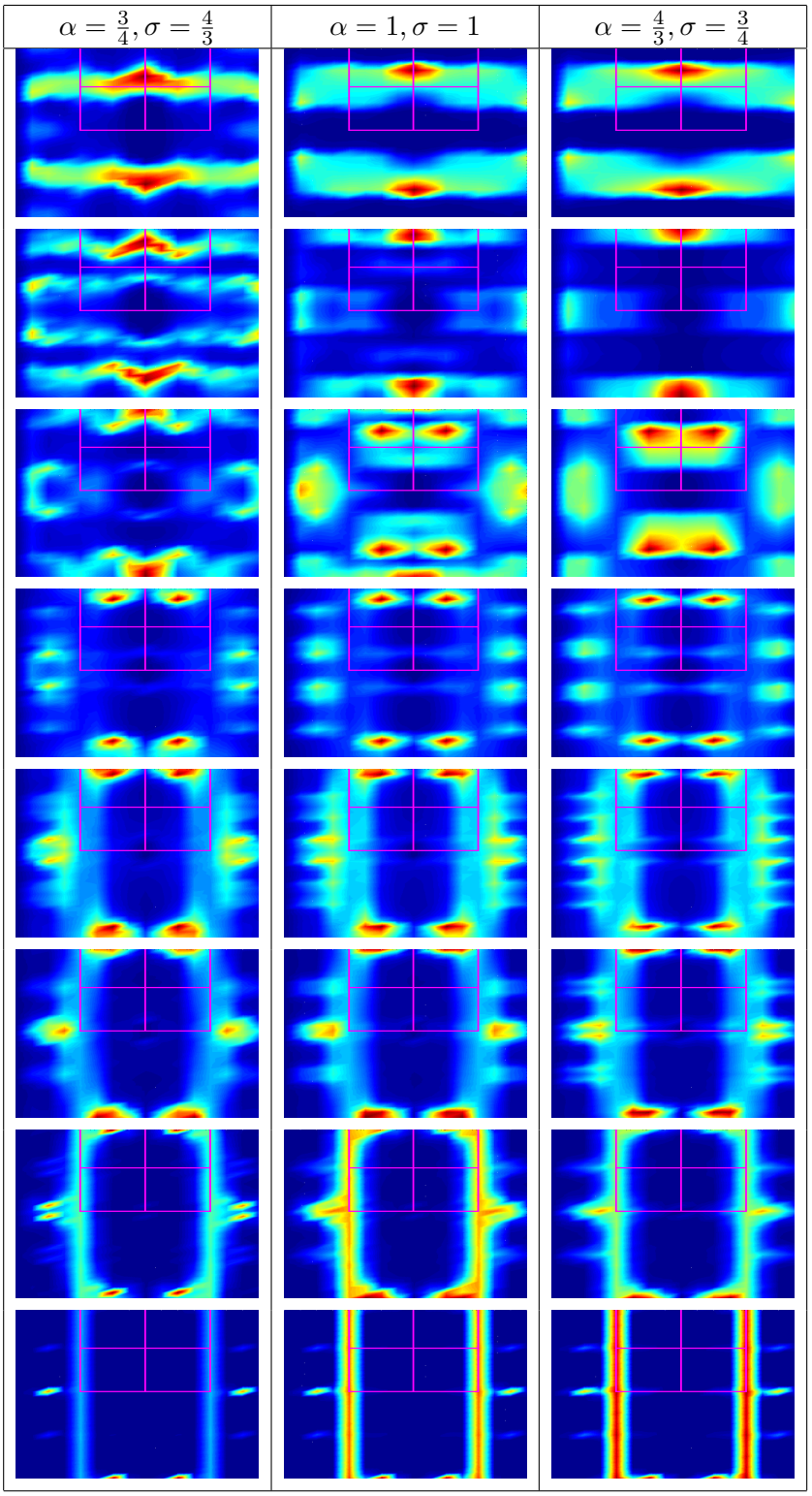


Figure 5.6: Structure factor in $(h0l)$ plane for $\sigma \in \{\frac{4}{3}, 1, \frac{3}{4}\}$ with $\alpha\sigma = 1$. Lowest energy slices are at the bottom, and highest ones at the top. Solid lines show the reciprocal lattice.

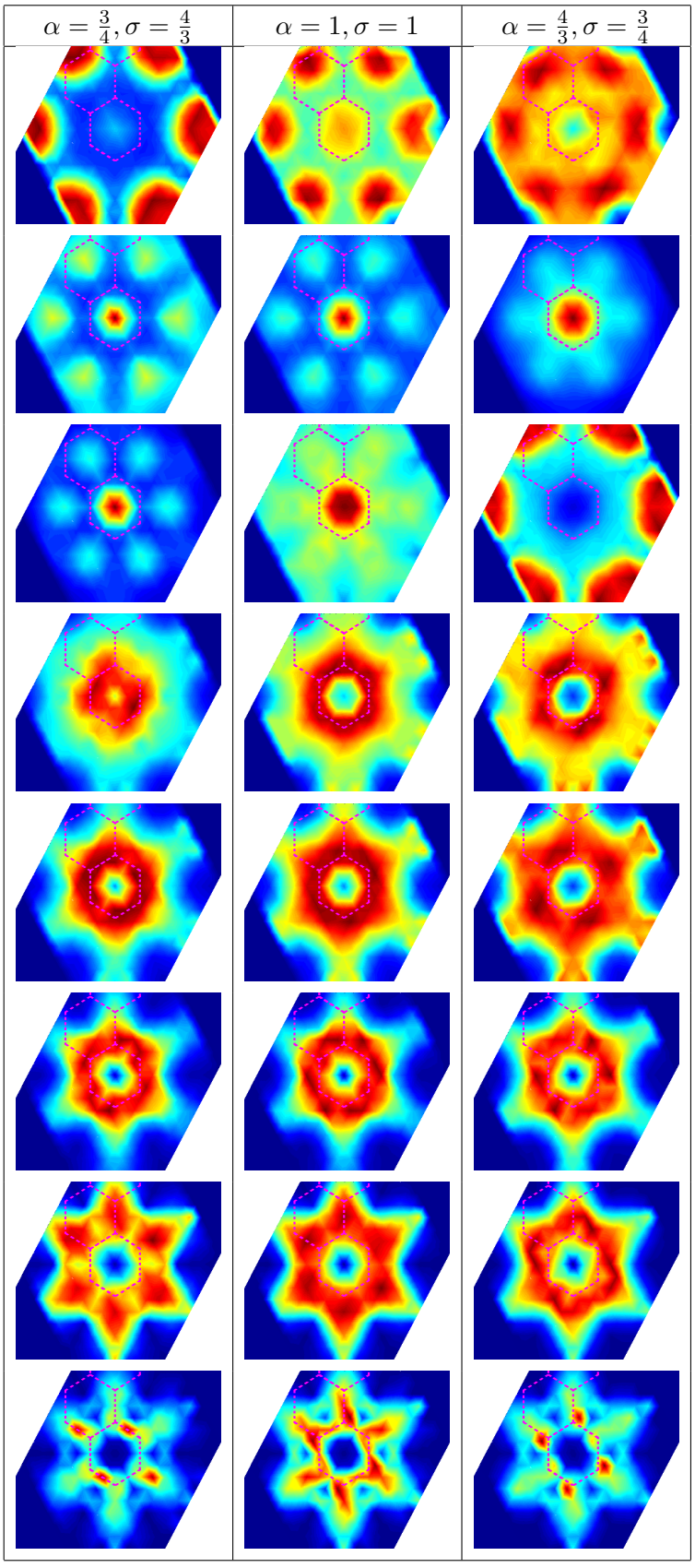


Figure 5.7: Structure factor in $(hk\bar{2})$ plane for $\sigma \in \{\frac{4}{3}, 1, \frac{3}{4}\}$ with $\alpha\sigma = 1$. Lowest energy slices are at the bottom, and highest ones at the top. Dashed lines show the Wigner-Seitz cells in reciprocal space.

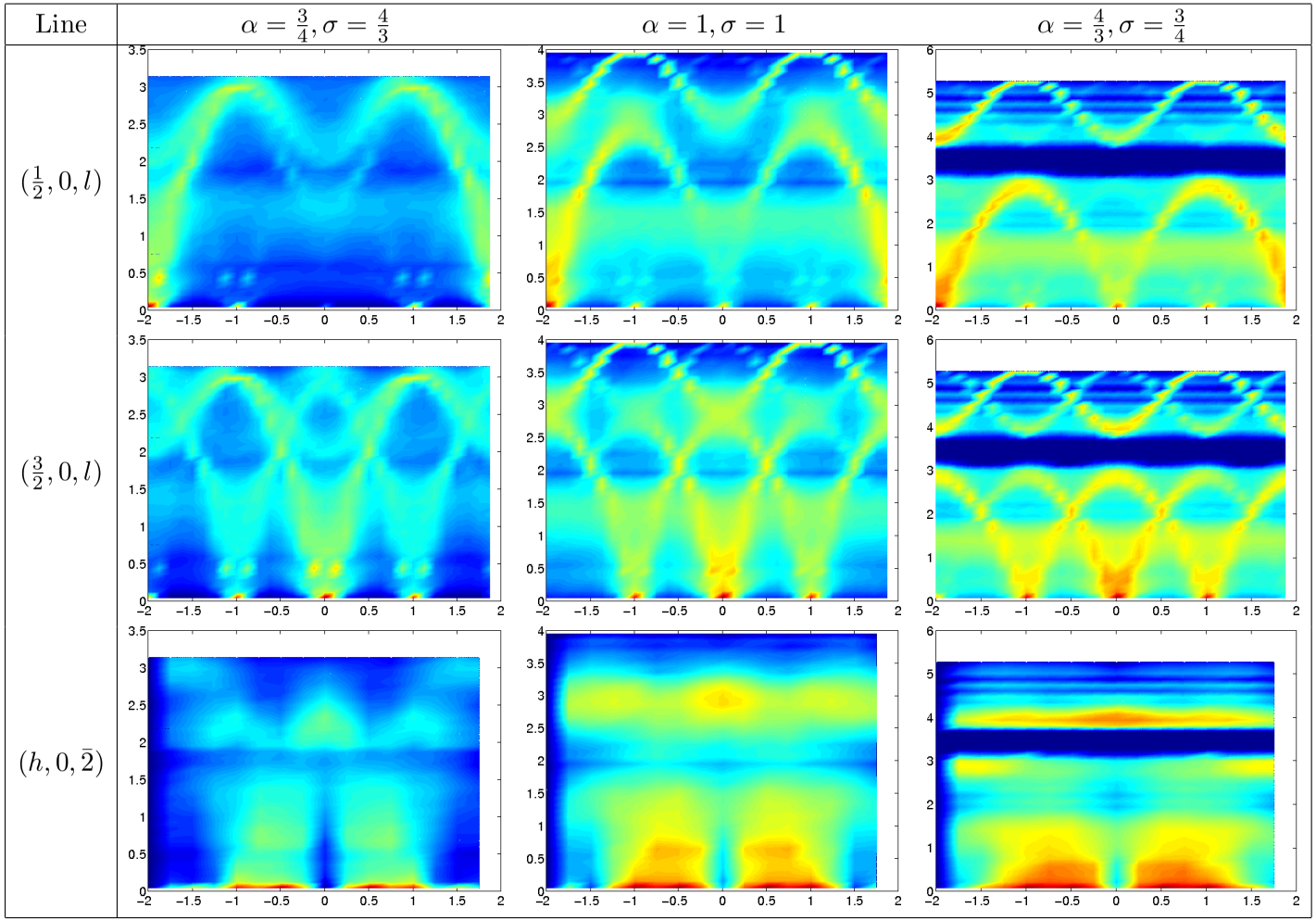


Figure 5.8: Structure factor along $(\frac{1}{2}, 0, l)$, $(\frac{3}{2}, 0, l)$ and $(h, 0, \bar{2})$ for $\sigma \in \{\frac{4}{3}, 1, \frac{3}{4}\}$ with $\alpha\sigma = 1$. The vertical axis gives the frequency in units of $J_1 S_k/\hbar$. Colour plots are produced using a logarithmic scale for the structure factor.

by our collaborators is still unpublished.[68] The plots in the $(h0l)$ plane are shown in Fig. 5.9, while those for the $(hk\bar{2})$ plane are in Fig. 5.10, and the cuts along $(\frac{1}{2}, 0, l)$, $(\frac{3}{2}, 0, l)$ and $(h, 0, \bar{2})$ are all shown in Fig. 5.11. While we are still working out some discrepent features in the patterns, especially along the cuts in Fig. 5.11, the preliminary conclusion is that the experimental data is most consistent with $\alpha\sigma = 1$ and $\sigma > 1$.

As far as we know, there are no published results comparing inelastic magnetic scattering from geometrically frustrated magnets against spinwave calculations. We believe that the reasonably close agreement we find, across a wide range of wavevectors and frequency, using only three fitting parameters (namely J_1, α and σ) is an encouraging indication that our approach is useful and that our Heisenberg Hamiltonian is reasonable.

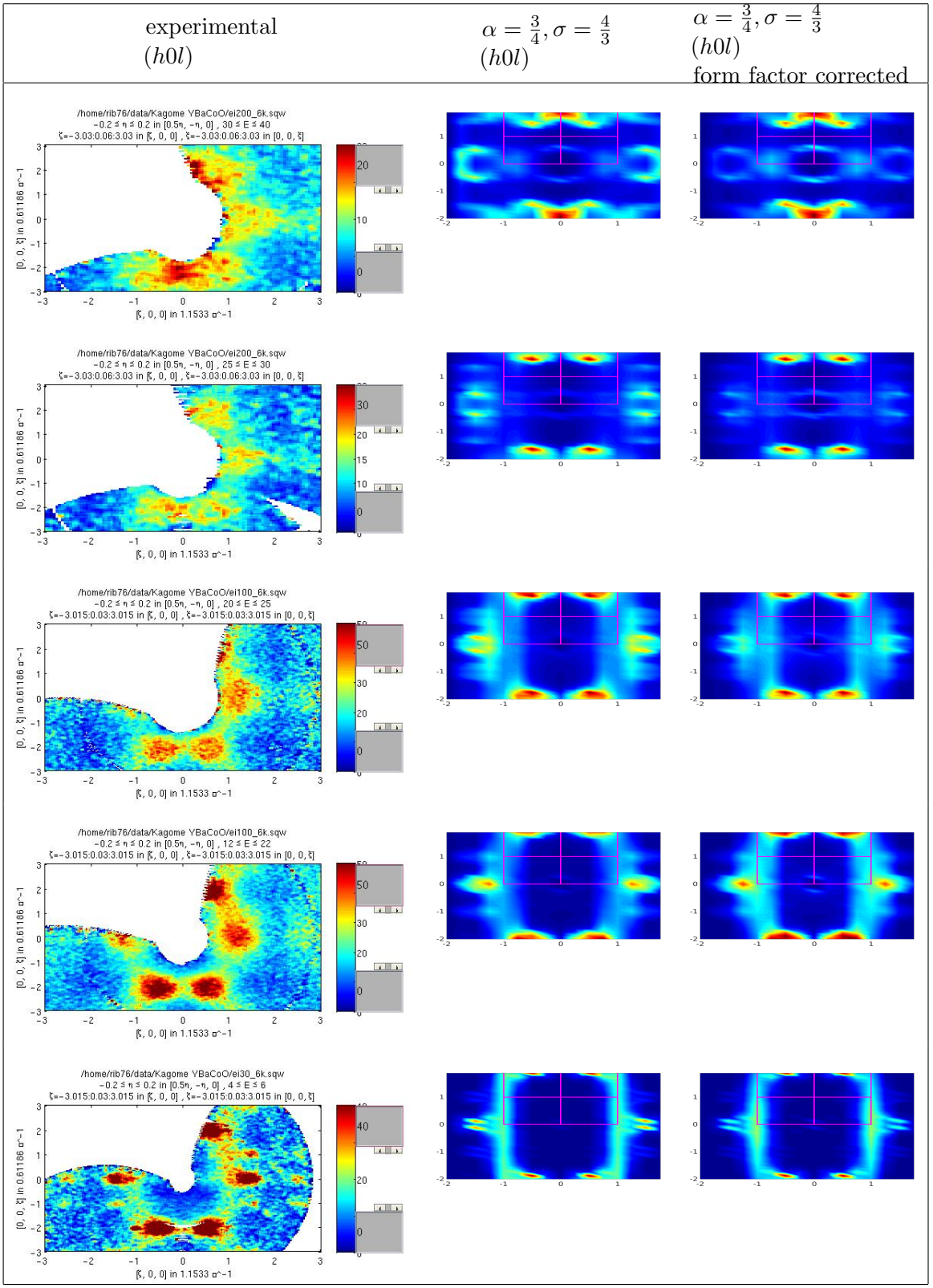


Figure 5.9: Structure factor in $(h0l)$ plane from experiments and for $\alpha = \frac{3}{4}, \sigma = \frac{4}{3}$. Lowest energy slices are at the bottom, and highest ones at the top. The h-direction is horizontal and the l-direction is vertical. Solid lines show the reciprocal lattice.

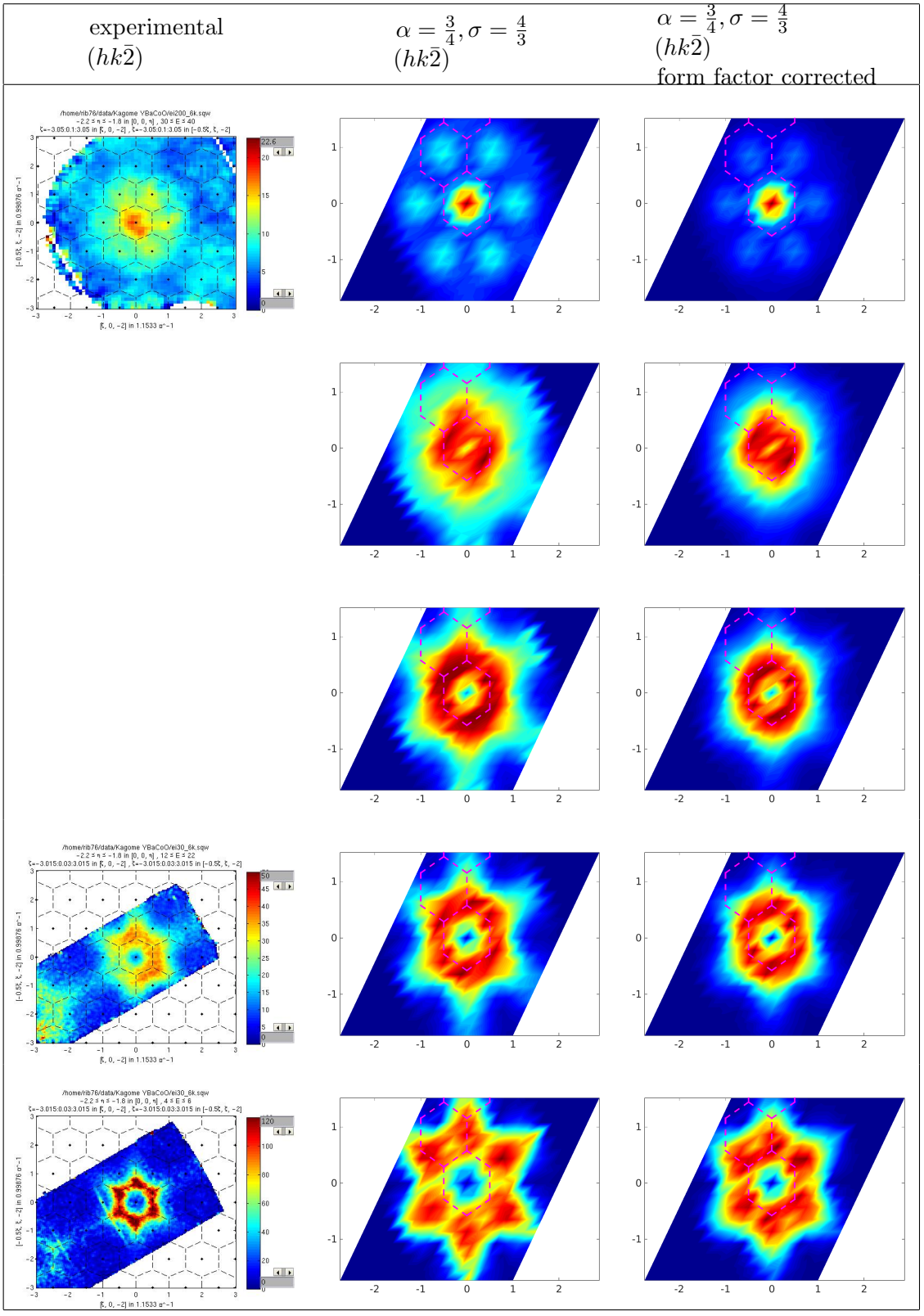


Figure 5.10: Structure factor in $(hk\bar{2})$ plane from experiments and for $\alpha = \frac{3}{4}, \sigma = \frac{4}{3}$. Lowest energy slices are at the bottom, and highest ones at the top. Dashed lines show the Wigner-Seitz cells in reciprocal space.

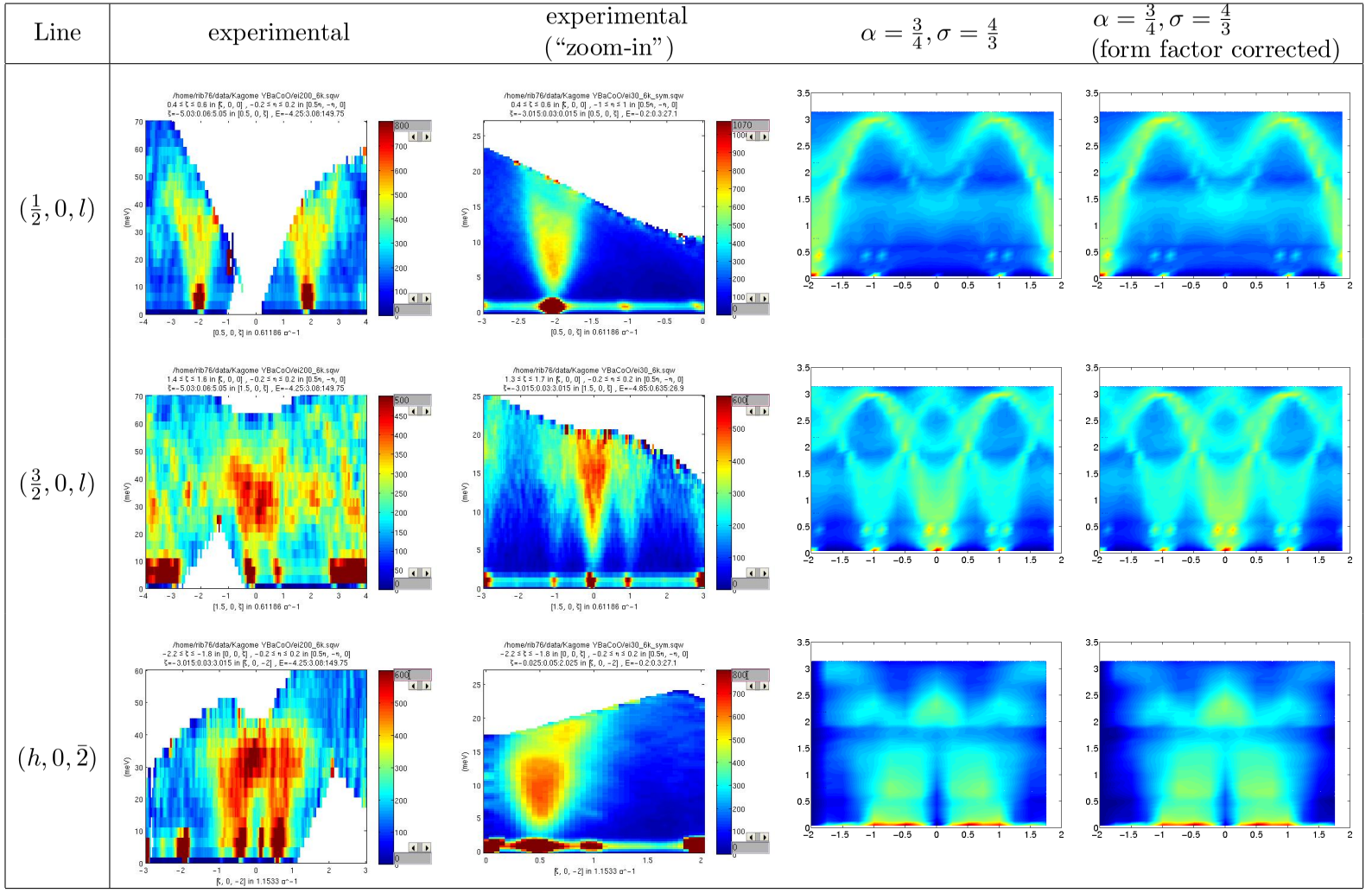


Figure 5.11: Structure factor along $(\frac{1}{2}, 0, l)$, $(\frac{3}{2}, 0, l)$ and $(h, 0, \bar{2})$ from experiments and for $\alpha = \frac{3}{4}, \sigma = \frac{4}{3}$. For spin waves, colour plots are produced using a logarithmic scale for the structure factor, and the vertical axis gives the frequency in units of $J_1 S_k/\hbar$. Experimental colour plots have been calibrated with an *inverse Bose weighting* technique.

CHAPTER 6

Stochastic dynamics

> Creativity is the ability to introduce order into the randomness of nature.
>
> — *Eric Hoffer*

To study the spin dynamics of the pyrochlore lattice, Conlon and Chalker developed the *stochastic SCGA* technique.[62] The idea is to extend the SCGA by introducing noise terms and allowing spin diffusion, allowing us to go beyond studying static spin correlations. While the spins in the classical ground states of the pyrochlore lattice are correlated due to the zero net spin on each tetrahedron, these spin correlations do not develop along definite columns, as they do in the extended kagome lattice. Compared to the pyrochlore lattice, we expect the spin dynamics to be slower for the extended kagome lattice due to the strong interlayer correlations along the columns of triangular lattice spins.

Our goal in this chapter is to use the stochastic SCGA to obtain an analytical prediction for this slower dynamics. While we can perform this extension of the SCGA with two Lagrange multipliers that we developed in Section 4.1, the ordering transition prevents us from deriving results at low temperatures. Motivated by the form of the effective coupling between kagome spins as discussed in Section 4.2, we will instead consider a modified geometry of *stacked kagome layers* that avoids ordering under the SCGA. The SCGA approach for stacked kagome layers is developed in Section 6.1. In Section 6.2, we describe the extension to stochastic SCGA, and work out the predictions for the spin dynamics from this model in Section 6.3.

6.1 SCGA for stacked kagome layers

We saw in Section 4.2 that integrating out the triangular lattice spins gives effective interactions based on the sum of the six kagome spins connected to a triangular lattice

spin. While such interactions are more intricate than classical Heisenberg interactions between pairs of spins, we will attempt to model this physics by considering identically stacked kagome layers with ferromagnetic Heisenberg interactions between spins on adjacent kagome layers. As we shall see in Section 6.1.4, such a simplified geometry allows the system to avoid ordering at finite temperature under the SCGA.

6.1.1 Lattice description

In the stacked system, each spin is coupled to six nearest-neighbour (n.n.) spins: four spins in-plane and one spin each in the adjacent planes above and below. The n.n. Heisenberg interactions within the plane are the usual antiferromagnetic (AFM) J_1, while the inter-plane coupling is ferromagnetic (FM). For this system, we denote the classical Heisenberg exchange interactions in Eq. (1.6) as

$$J_{ij} = \begin{cases} J = J_1 > 0 & \text{n.n. within layer (AFM)} \\ J' \propto -J_2 < 0 & \text{n.n. inter-layer (FM)} \end{cases}$$

and let

$$\alpha' \equiv \frac{-J'}{J} > 0 \,. \tag{6.1}$$

Note that there are only kagome spins in this system as the triangular lattice spins have been integrated out, as described in Section 4.2.

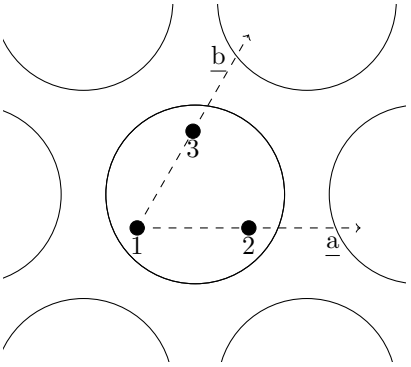


Figure 6.1: 3-site unit cell for SCGA on stacked kagome layers.

Our simplified lattice has a unit cell of three spins, with the usual 3D hexagonal lattice system (see Fig. 6.1). The site numbering convention $\mu \in \{1, 2, 3\}$ shown is similar to what

we have been using. The Hamiltonian is

$$\mathcal{H} = \tfrac{1}{2} J S^2 \sum_{i,j} B_{ij}(\alpha')\, \boldsymbol{n}_i \cdot \boldsymbol{n}_j \ , \tag{6.2}$$

and the *interaction matrix* we use here (to avoid confusion with the notation in Section 4.1) is

$$B_{ij}(\alpha') = B_{ij}^{(1)} - \alpha' B_{ij}^{(2)} \ , \tag{6.3}$$

with $B_{ij}^{(1,2)}$ being the adjacency matrices for sites within and between the stacked layers respectively.

We also use the same conventions for lattice vectors, as defined in Eq. (4.9) and Eq. (4.10). Using the same Fourier transform conventions as in Eq. (4.12), the interaction matrix in the Fourier basis can be written in block-diagonal form as

$$B(\boldsymbol{q}) = K(\boldsymbol{q}) - \alpha' z(\boldsymbol{q})\, \mathbb{1} \ , \tag{6.4}$$

where

$$K(\boldsymbol{q}) = \begin{pmatrix} 0 & u(\boldsymbol{q}) & v(\boldsymbol{q}) \\ u(\boldsymbol{q}) & 0 & w(\boldsymbol{q}) \\ v(\boldsymbol{q}) & w(\boldsymbol{q}) & 0 \end{pmatrix} \tag{6.5}$$

and the $\boldsymbol{q}$-dependent variables are

$$\begin{cases} u(\boldsymbol{q}) = 2\cos(\boldsymbol{q}\cdot\boldsymbol{u}) \\ v(\boldsymbol{q}) = 2\cos(\boldsymbol{q}\cdot\boldsymbol{v}) \\ w(\boldsymbol{q}) = 2\cos(\boldsymbol{q}\cdot\boldsymbol{w}) \\ z(\boldsymbol{q}) = 2\cos\left(\boldsymbol{q}\cdot\boldsymbol{c}\right) \ . \end{cases} \tag{6.6}$$

Notice that $K(\boldsymbol{q}) = K(q_x, q_y)$ depends only on the in-plane wavevector, while $z(\boldsymbol{q}) = z(q_z)$ depends only on the out-of-plane wavevector. The matrix $K(\boldsymbol{q})$ is the kagome adjacency matrix that is relevant to SCGA for the 2D kagome lattice, as discussed by Garanin and Canals.[65]

6.1.2 Band structure

To implement the SCGA, we use a single Lagrange multiplier λ for all sites, which gives the approximate partition function Eq. (4.14) for a single spin component,

$$Z = \int \prod_{\boldsymbol{q},\mu} \mathrm{d}s^{\mu}_{\boldsymbol{q}} \, \exp\left(-\tfrac{1}{2} \sum_{\boldsymbol{q},\mu,\nu} s^{\mu}_{\boldsymbol{q}} \left[M(\boldsymbol{q})\right]^{\mu\nu} s^{\nu}_{-\boldsymbol{q}}\right) ,$$

so that the spin correlations are given by $\langle s^{\mu}_{\boldsymbol{q}} s^{\nu}_{-\boldsymbol{q}} \rangle = \left[M^{-1}(\boldsymbol{q})\right]^{\mu\nu}$ from Eq. (4.15). The *SCGA matrix* in this case is

$$M(\boldsymbol{q}) = \lambda \mathbb{1} + \beta J S^2 V(\boldsymbol{q}) \, , \tag{6.7}$$

with

$$\begin{aligned} V(\boldsymbol{q}) &\equiv \left[2\mathbb{1} + K(\boldsymbol{q})\right] + \alpha' \left[2 - z(\boldsymbol{q})\right] \mathbb{1} \\ &= K(\boldsymbol{q}) + \left[2(1+\alpha') - \alpha' z(\boldsymbol{q})\right] \mathbb{1} \, . \end{aligned} \tag{6.8}$$

The matrix $V(\boldsymbol{q})$ has been defined to give a minimum eigenvalue of zero. This minimum occurs when $q_z = 0$ for all (q_x, q_y).

Because they are related by the addition of copies of the identity, the eigenvectors of $V(\boldsymbol{q})$ and $M(\boldsymbol{q})$ are the eigenvectors of the matrix $K(\boldsymbol{q})$ in Eq. (6.5). We write the eigenvalues and eigenvectors of $K(\boldsymbol{q})$ as $\{K_a(\boldsymbol{q})\}$ and $\{\vec{U}_a(\boldsymbol{q})\}$ respectively, with $a \in \{1, 2, 3\}$. Following Ref. [65] we write

$$\begin{cases} K_1(\boldsymbol{q}) = -2 \\ K_{2,3}(\boldsymbol{q}) = 1 \mp \sqrt{u(\boldsymbol{q})^2 + v(\boldsymbol{q})^2 + w(\boldsymbol{q})^2 - 3} \end{cases} \tag{6.9}$$

and

$$\vec{U}_a(\boldsymbol{q}) = \frac{1}{\sqrt{N_a}} \begin{pmatrix} uw + vK_a \\ uv + wK_a \\ K_a^2 - u^2 \end{pmatrix} , \tag{6.10}$$

where

$$N_a(\boldsymbol{q}) = \left[uw + vK_a\right]^2 + \left[uv + wK_a\right]^2 + \left[K_a^2 - u^2\right]^2 .$$

The eigenvalues $\{K_a(\boldsymbol{q})\}$ in Eq. (6.9) are shown in Fig. 6.2.

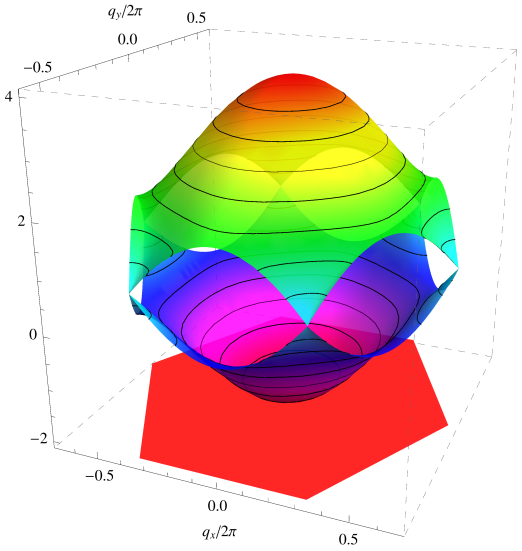


Figure 6.2: Band structure for the eigenvalues Eq. (6.9) of the kagome adjacency matrix $K(\boldsymbol{q})$.

6.1.3 Self-consistency conditions

The self-consistency conditions in Eq. (4.8) for each site index μ can be written as

$$\frac{1}{\Omega_{\mathrm{BZ}}} \int \mathrm{d}^3\boldsymbol{q} \sum_a \frac{\left|[\vec{U}_a(\boldsymbol{q})]_\mu\right|^2}{\lambda + \beta J S^2 v_a(\boldsymbol{q})} = \frac{1}{3} \,,$$

where $\{v_a(\boldsymbol{q})\}$ are the eigenvalues of $V(\boldsymbol{q})$, and $\Omega_{\mathrm{BZ}} = 4\pi^3/\sqrt{3}$ is the volume of the BZ in reciprocal lattice units. We take the sum over sites, and since the eigenvectors are normalised, we have $\sum_\mu \left|[\vec{U}_a(\boldsymbol{q})]_\mu\right|^2 = 1$, so self-consistency requires that

$$\frac{1}{\Omega_{\mathrm{BZ}}} \int \mathrm{d}^3\boldsymbol{q} \sum_a \frac{1}{\lambda + \beta J S^2 v_a(\boldsymbol{q})} = 1 \,. \tag{6.11}$$

Since

$$v_a(\boldsymbol{q}) = [2 + K_a(\boldsymbol{q})] + \alpha' \left[2 - z(\boldsymbol{q})\right] \geq 0 \,, \tag{6.12}$$

we see that we must have $\lambda > 0$ so that the self-consistent integral is well-behaved.

6.1.4 Low-temperature analytic behaviour

For each value of q_z, the eigenvector $\vec{U}_1(\boldsymbol{q})$ for the kagome flat band gives the minimum eigenvalue of $V(\boldsymbol{q})$ for all in-plane wavevectors. Thus, the contribution from

$$v_1(\boldsymbol{q}) = \alpha' \left[2 - z(\boldsymbol{q})\right]$$

dominates the self-consistency integral Eq. (6.11). At low temperatures $\beta JS^2 \gg 1$, we neglect the contributions from the other bands and write

$$\frac{1}{\Omega_{\mathrm{BZ}}} \int \mathrm{d}^3\boldsymbol{q}\, \frac{1}{\lambda + \beta JS^2\alpha'[2 - z(\boldsymbol{q})]} = \frac{1}{2\pi} \int_{-\pi}^{\pi} \frac{dq_z}{\lambda + 2\beta JS^2\alpha'(1 - \cos q_z)} = 1 \,,$$

where we have trivially integrated over q_x and q_y because the denominator is flat in (q_x, q_y). The integral over q_z can be done exactly, yielding

$$\frac{1}{\sqrt{\lambda(\lambda + 4\beta JS^2\alpha')}} = 1 \implies \lambda^2 + 4\beta JS^2\alpha'\lambda - 1 = 0 \,.$$

Since we require $\lambda > 0$, we take the positive root

$$\lambda = \sqrt{1 + (2\beta JS^2\alpha')^2} - 2\beta JS^2\alpha' \,, \tag{6.13}$$

and as we are in the limit where $\beta JS^2 \gg 1$, we have

$$\lambda = \frac{1}{4\beta JS^2\alpha'} + O\left[(\beta JS^2)^{-3}\right] \,. \tag{6.14}$$

We note that λ approaches zero only in the $T \to 0$ limit, suggesting a zero-temperature phase transition, since the eigenvalues of $M^{-1}(\boldsymbol{q})$ diverge. The stacked kagome system *avoids ordering at finite temperature*. Unsurprisingly, in this limit where we have ignored contributions from the dispersive bands of $K(\boldsymbol{q})$, our model behaves like the SCGA for a 1D ferromagnet along the q_z axis.

6.2 Stochastic SCGA

Linear spinwave theory was used in Chapter 5 to describe the spin dynamics on short timescales as harmonic fluctuations around a classical ground state. On longer timescales, the spin configuration itself might drift around the ground state manifold, and we need a different approach. One strategy for studying the dynamics on long timescales is to construct a stochastic model based on spin diffusion and the SCGA, using a technique developed by Conlon and Chalker.[62] The introduction of noise terms mimic interactions with a thermal bath, which simplifies the implementation of exact energy conservation in the spin dynamics.

6.2.1 Spin diffusion

We outline the stochastic SCGA approach following Ref. [62]. Since the Hamiltonian is invariant under global spin rotations, total spin is conserved. We can see this explicitly by writing the classical equations of motion Eq. (1.6) as a continuity equation

$$\frac{d\boldsymbol{S}_i}{dt} + \sum_j \boldsymbol{I}_{ij} = 0 \,, \tag{6.15}$$

where we have defined the *spin current* flowing from site $i \to j$ as

$$\boldsymbol{I}_{ij} \equiv \frac{J_{ij}}{\hbar} \boldsymbol{S}_i \times \boldsymbol{S}_j \,.$$

We make the approximation that each spin component is decoupled, just as in the SCGA, and just consider Eq. (6.15) for a single component

$$\frac{ds_i}{dt} + \sum_j I_{ij} = 0 \,. \tag{6.16}$$

We model the spin current terms in Eq. (6.16) phenomenologically, requiring terms that are local and spin-conserving. The form of the spin current from site $i \to j$ is taken to be

$$I_{ij} = -\Gamma \left(\sum_l \nabla_{ij,l} \frac{\partial E}{\partial s_l} \right) + |J_{ij}| \zeta_{ij} \,, \tag{6.17}$$

where $\Gamma > 0$ is a (free) parameter, the (dimensionless) *scaled lattice gradient operator* in the direction from $i \to j$ is

$$\sum_l \nabla_{ij,l} \equiv \sum_l \frac{|J_{ij}|}{J} (\delta_{jl} - \delta_{il}) \,,$$

and $\zeta_{ij} = -\zeta_{ji}$ is the *bond noise*. The "amount" of spin is like a liquid flowing through the lattice bonds, and the current flow is proportional to the strength of the Heisenberg exchange coupling $|J_{ij}|$. In this model, the two kinds of forces responsible for spin currents are:

1. Energy gradients that cause a spin current in the opposite direction to the gradient. These forces minimise the energy and provide an ordering tendency.
2. Stochastic bond noise that mimics the effect of thermal fluctuations at temperature T, maintaining disorder.

Putting this spin current Eq. (6.17) into Eq. (6.16), the dynamical equations are

$$\frac{ds_i}{dt} - \Gamma \sum_l \Delta_{il} \frac{\partial E}{\partial s_l} = \eta_i(t) \ , \tag{6.18}$$

where the sum of the scaled lattice gradient operator over sites j gives the (dimensionless) *scaled lattice Laplacian operator* at site i,

$$\sum_l \Delta_{il} \equiv \sum_j \left(\sum_l \nabla_{ij,l} \right) \ , \tag{6.19}$$

and the *site noise* is

$$\eta_i(t) \equiv -\sum_j |J_{ij}| \zeta_{ij} \ . \tag{6.20}$$

We use the SCGA so that the energy is quadratic in the spin configuration, and hence the energy gradients $\left\{ \frac{\partial E}{\partial s_l} \right\}$ are linear functions of the spins. The exponent of the Boltzmann weight for each configuration in the SCGA canonical ensemble takes the form

$$-\beta E = -\tfrac{1}{2} \sum_{i,j} s_i M_{ij} s_j \ ,$$

where the real symmetric matrix M is the SCGA matrix Eq. (6.7) in real-space. We have

$$\frac{\partial E}{\partial s_l} = \frac{1}{\beta} \sum_j M_{lj} s_j \ ,$$

which we put into Eq. (6.18) to get

$$\frac{ds_i}{dt} - \frac{\Gamma}{\beta} \sum_{l,j} \Delta_{il} M_{lj} s_j = \eta_i(t) \ . \tag{6.21}$$

To simplify this further, use the explicit expression for Eq. (6.19)

$$\Delta_{ij} = (-4 - 2\alpha')\delta_{ij} + B^{(1)}_{ij} + \alpha' B^{(2)}_{ij} \ ,$$

which has the Fourier transform

$$\Delta(\boldsymbol{q}) = K(\boldsymbol{q}) + [\alpha' z(\boldsymbol{q}) - 4 - 2\alpha'] \mathbb{1} \ . \tag{6.22}$$

We see from Eq. (6.7) and Eq. (6.22) that the matrices M and Δ will be simultaneously diagonalised by the eigenvectors $\{\vec{U}_a(\boldsymbol{q})\}$ of $K(\boldsymbol{q})$. Making the orthogonal transformation to this common basis labelled by wavevector and band index $\{(\boldsymbol{q}, a)\}$, we transform Eq. (6.21)

into the *ordinary stochastic differential equations*

$$\frac{d\tilde{s}^a_{\boldsymbol{q}}}{dt} + \gamma^a_{\boldsymbol{q}}\tilde{s}^a_{\boldsymbol{q}} = \tilde{\eta}^a_{\boldsymbol{q}}(t) \ , \tag{6.23}$$

where

$$\begin{aligned}\gamma^a_{\boldsymbol{q}} &= -\frac{\Gamma}{\beta}[K_a(\boldsymbol{q}) + \alpha' z(\boldsymbol{q}) - 4 - 2\alpha'][\lambda + \beta J S^2 v_a(\boldsymbol{q})] \\ &= \frac{\Gamma}{\beta}\left\{[4 - K_a(\boldsymbol{q})] + \alpha'[2 - z(\boldsymbol{q})]\right\}[\lambda + \beta J S^2 v_a(\boldsymbol{q})] \geq 0 \ .\end{aligned} \tag{6.24}$$

6.2.2 General solution

The general solution to Eq. (6.23) has contributions from the homogeneous (noise-free) and inhomogeneous parts, and is described in books such as the one by Risken.[69] The homogeneous solution is

$$G^a_{\boldsymbol{q}}(t) = \exp(-\gamma^a_{\boldsymbol{q}} t) \tag{6.25}$$

and the general solution is

$$\tilde{s}^a_{\boldsymbol{q}}(t) = G^a_{\boldsymbol{q}}(t)\tilde{s}^a_{\boldsymbol{q}}(0) + \int_0^t dt' \, G^a_{\boldsymbol{q}}(t - t')\tilde{\eta}^a_{\boldsymbol{q}}(t') \ . \tag{6.26}$$

The value of $\gamma^a_{\boldsymbol{q}}$ in Eq. (6.24) gives the *band-dependent relaxation rate*, and at long times, small values of $\gamma^a_{\boldsymbol{q}}$ dominate the physics.

6.2.3 Noise correlators

To complete the discussion on the stochastic SCGA, we need to check that the noise terms we introduced give a *constant* expectation value for the static spin correlators $\langle \tilde{s}^a_{-\boldsymbol{q}}(t)\tilde{s}^a_{\boldsymbol{q}}(t)\rangle$ at all times t.

We assume that the noise is uncorrelated in time, so that the ensemble averages give

$$\begin{cases} \langle \tilde{\eta}^a_{\boldsymbol{q}}(t)\rangle = 0 \\ \langle \tilde{\eta}^a_{-\boldsymbol{q}}(t)\tilde{\eta}^a_{\boldsymbol{q}}(t')\rangle = \mathcal{N}^a_{\boldsymbol{q}} \, \delta(t - t') \ , \end{cases} \tag{6.27}$$

where $\mathcal{N}^a_{\boldsymbol{q}}$ is to be determined. Using Eq. (6.26), we have

$$\begin{aligned}\langle \tilde{s}^a_{-\boldsymbol{q}}(t)\tilde{s}^a_{\boldsymbol{q}}(t)\rangle &= e^{-2\gamma^a_{\boldsymbol{q}}t}\langle \tilde{s}^a_{-\boldsymbol{q}}(0)\tilde{s}^a_{\boldsymbol{q}}(0)\rangle + \mathcal{N}^a_{\boldsymbol{q}}\, e^{-2\gamma^a_{\boldsymbol{q}}t}\int_0^t \mathrm{d}t'\, e^{2\gamma^a_{\boldsymbol{q}}t'} \\ &= e^{-2\gamma^a_{\boldsymbol{q}}t}\left[\langle \tilde{s}^a_{-\boldsymbol{q}}(0)\tilde{s}^a_{\boldsymbol{q}}(0)\rangle + \frac{\mathcal{N}^a_{\boldsymbol{q}}}{2\gamma^a_{\boldsymbol{q}}}\left(e^{2\gamma^a_{\boldsymbol{q}}t}-1\right)\right] .\end{aligned}$$

We see that we require

$$\mathcal{N}^a_{\boldsymbol{q}} = 2\gamma^a_{\boldsymbol{q}}\langle \tilde{s}^a_{-\boldsymbol{q}}(0)\tilde{s}^a_{\boldsymbol{q}}(0)\rangle \tag{6.28}$$

so that $\langle \tilde{s}^a_{-\boldsymbol{q}}\tilde{s}^a_{\boldsymbol{q}}\rangle$ is constant in time. From the SCGA, we have

$$\langle \tilde{s}^a_{-\boldsymbol{q}}\tilde{s}^a_{\boldsymbol{q}}\rangle = \frac{1}{\lambda + \beta J S^2 v_a(\boldsymbol{q})} ,$$

so the noise correlator Eq. (6.27) in this basis is

$$\langle \tilde{\eta}^a_{-\boldsymbol{q}}(t)\tilde{\eta}^a_{\boldsymbol{q}}(t')\rangle = \frac{2\gamma^a_{\boldsymbol{q}}}{\lambda + \beta J S^2 v_a(\boldsymbol{q})}\delta(t-t') .$$

Going back to real-space, we see by reference to Eq. (6.24) that the noise correlators must be given by the scaled lattice Laplacian, i.e.,

$$\langle \eta_i(t)\eta_j(t')\rangle = -2\frac{\Gamma}{\beta}\Delta_{ij}\delta(t-t') . \tag{6.29}$$

6.3 Spin autocorrelation function

We consider the spin autocorrelation function

$$\begin{aligned}A(t) &\equiv \frac{1}{N}\sum_i \langle s_i(0)s_i(t)\rangle \\ &\underset{N\to\infty}{=} \tfrac{1}{3}\sum_a \frac{1}{\Omega_{\mathrm{BZ}}}\int \mathrm{d}^3\boldsymbol{q}\, \langle \tilde{s}^a_{-\boldsymbol{q}}(0)\tilde{s}^a_{\boldsymbol{q}}(t)\rangle \end{aligned}\tag{6.30}$$

to study how the spin configuration changes with time. Since we have

$$\begin{aligned}\langle \tilde{s}^a_{-\boldsymbol{q}}(0)\tilde{s}^a_{\boldsymbol{q}}(t)\rangle &= \langle \tilde{s}^a_{-\boldsymbol{q}}(0)\tilde{s}^a_{\boldsymbol{q}}(0)\rangle \exp(-\gamma^a_{\boldsymbol{q}}t) \\ &= \frac{1}{\lambda + \beta J S^2 v_a(\boldsymbol{q})}\exp(-\gamma^a_{\boldsymbol{q}}t) ,\end{aligned}$$

the significant contributions at longer times come from modes with the slowest relaxation rates. From Eq. (6.24), the relaxation rate $\gamma^a_{\boldsymbol{q}}$ vanishes when

$$(4-K_a) + \alpha'(2-z) = 0 , \tag{6.31}$$

or when

$$\lambda + \beta J S^2 v_a = 0 \, . \tag{6.32}$$

For the first case, this happens only for the highest band $a = 3$ at the single point $\boldsymbol{q} = 0$. For the second case, this happens for the kagome flat band $a = 1$ with $q_z = 0$ and all values of (q_x, q_y), as well as for the band $a = 2$ at the single point $\boldsymbol{q} = 0$.

As the spin autocorrelation Eq. (6.30) is integrated over wavevectors, the leading contribution at long times comes from the kagome flat band $a = 1$, for small q_z and all values of (q_x, q_y). In the limit of $\beta J S^2 \gg 1$, we found in Eq. (6.14) that

$$\lambda = \frac{1}{4\beta J S^2 \alpha'} \, ,$$

so putting this into Eq. (6.24), for $a = 1$, we get

$$\gamma^1_{\boldsymbol{q}} = \frac{\Gamma}{\beta}[6 + \alpha'(2 - z)] \left[\frac{1}{4\beta J S^2 \alpha'} + \beta J S^2 \alpha'(2 - z) \right] \, .$$

We use the small q_z approximation that

$$2 - z = q_z^2 \, ,$$

and extend the domain of q_z integration to the entire real line, since the exponential factor suppresses contributions from large $|q_z|$. The leading behaviour of the spin autocorrelation Eq. (6.30), dropping all constant numerical pre-factors, is

$$\begin{aligned} A(t) &\sim \int_{-\infty}^{+\infty} \frac{\mathrm{d}q_z}{\frac{1}{4\beta J S^2 \alpha'} + \beta J S^2 \alpha' q_z^2} \exp\left[-\frac{t\Gamma}{\beta}(6 + \alpha' q_z^2) \left(\frac{1}{4\beta J S^2 \alpha'} + \beta J S^2 \alpha' q_z^2 \right) \right] \\ &\sim \exp\left(-\frac{3t\Gamma}{2\beta^2 J S^2 \alpha'} \right) \int_{-\infty}^{+\infty} \frac{\mathrm{d}q_z}{1 + C_1 q_z^2} \exp\left(-C_2 q_z^2 \right) \, , \end{aligned} \tag{6.33}$$

where we have kept only leading-order terms for $1/\beta J S^2 \ll 1$ and $|q_z| \ll 1$, and defined the coefficients

$$\begin{cases} C_1 = \left(2\beta J S^2 \alpha' \right)^2 \\ C_2 = \frac{t\Gamma}{\beta} \left(6\beta J S^2 \alpha' + \frac{1}{4\beta J S^2} \right) \, . \end{cases} \tag{6.34}$$

We evaluate the integral exactly, using Mathematica, and find

$$\int_{-\infty}^{+\infty} \frac{\mathrm{d}q_z}{1 + C_1 q_z^2} \exp\left(-C_2 q_z^2 \right) = \frac{\pi}{\sqrt{C_1}} \exp\left(C_2 / C_1 \right) \operatorname{erfc}\left(\sqrt{C_2 / C_1} \right) \, ,$$

where

$$\mathrm{erfc}(z) \equiv \frac{2}{\sqrt{\pi}} \int_z^\infty \exp\left(-x^2\right)\, \mathrm{d}x$$

is the *complementary error function*. From Eq. (6.34) we have that

$$C_2/C_1 = \frac{t\Gamma}{\beta}\left(\frac{3}{2\beta JS^2\alpha'} + \frac{1}{(\beta JS^2)^3(4\alpha')^2}\right) ,$$

so the spin autocorrelation goes as

$$A(t) \sim \exp\left(\frac{t\Gamma}{\beta(\beta JS^2)^3(4\alpha')^2}\right) \mathrm{erfc}\left(\sqrt{\frac{3t\Gamma}{2\beta^2 JS^2\alpha'}}\right) . \tag{6.35}$$

The complementary error function can be approximated[70] as

$$\mathrm{erfc}(z) \approx \tfrac{1}{6}\exp\left(-z^2\right) + \tfrac{1}{2}\exp\left(-\tfrac{4}{3}z^2\right) ,$$

and so for $1/\beta JS^2 \ll 1$ we can safely drop the β^{-4} term in the exponential function in Eq. (6.35). The leading behaviour of $A(t)$, at large t (and low temperature), is

$$A(t) \sim \mathrm{erfc}\left(\sqrt{\frac{3\Gamma}{2JS^2\alpha'}\frac{t}{\beta^2}}\right) . \tag{6.36}$$

The stochastic SCGA thus predicts the collapse of the autocorrelation function for different temperatures according to a t/β^2 rescaling of time. In contrast, there is a t/β rescaling for the pyrochlore lattice.[13,14] There is a more drastic slowing down of the dynamics of the stacked kagome system at low temperatures, due to the strong interlayer correlations.

CHAPTER 7

Molecular dynamics

> Computers make it easier to do a lot of things, but most of the things they make it easier to do don't need to be done.
>
> — *Andy Rooney*

Molecular dynamics (MD) refers to the numerical integration of equations of motion. In this chapter, we use MD to calculate the spin autocorrelation as a function of time for the classical nearest-neighbour Heisenberg antiferromagnet on the extended kagome lattice. This technique has also been applied to the kagome[71–73] and pyrochlore[13,14,62] lattices. For the pyrochlore lattice, Moessner and Chalker argued based on spin diffusion that the spin autocorrelation goes as

$$\langle \boldsymbol{S}(0) \cdot \boldsymbol{S}(t) \rangle = \exp(-\Gamma t) \ , \tag{7.1}$$

where $\Gamma = ck_BT/\hbar$ and c is a dimensionless constant of order unity. This gives a relaxation time for the autocorrelation $\tau = \Gamma^{-1} \sim T^{-1}$, which was confirmed by MD simulations.[13,14] Using the stochastic SCGA, Conlon and Chalker showed that the T^{-1} relaxation time was due to the dynamics from the flat bands of the pyrochlore adjacency matrix.[62] Robert et al. also found the same T^{-1} relaxation time for the spin autocorrelation on the kagome lattice, using a combined Monte Carlo and MD technique. They found that the order by disorder transition to coplanar spin states did not affect the autocorrelation relaxation time.[72] A more recent paper by Taillefumier et al. also finds the T^{-1} relaxation time for the kagome lattice in the classical spin liquid regime, but anisotropic dynamics below the order by disorder transition, with different temperature dependence of the relaxation time for in-plane and out-of-plane fluctuations.[73]

The plan for this chapter is as follows. In Section 7.1, we provide a detailed description of our MD simulations. Our results are then presented in Section 7.2, where we compare MD with predictions from linear spinwave theory and stochastic SCGA, as well as with the published results for the pyrochlore and kagome lattices.

7.1 MD simulations

Our algorithm follows the one described by Moessner and Chalker for the pyrochlore lattice.[13,14] There are two main steps in this algorithm for classical spins. First, generation of thermal spin configurations $\{\boldsymbol{S}_i\}$ via simulated annealing. Second, numerical integration of the classical equations of motion

$$\frac{d\boldsymbol{S}_i}{dt} = \boldsymbol{S}_i \times \boldsymbol{H}_i \ , \ \text{with} \ \ \boldsymbol{H}_i \equiv -\sum_j \frac{J_{ij}}{\hbar}\boldsymbol{S}_j \tag{7.2}$$

for each initial spin configuration. The results for the spin autocorrelation function are then averaged over choices of initial spin configurations to improve statistics. The spin autocorrelation function

$$A^{\mu}(t) \equiv \langle \boldsymbol{S}^{\mu}(0) \cdot \boldsymbol{S}^{\mu}(t) \rangle \tag{7.3}$$

is averaged over equivalent sites in all unit cells, where $\mu \in \{1, \ldots, 8\}$ indexes the sites in the unit cell. We will take further averages over all kagome lattice sites (A_k) and over all triangular lattice sites (A_t), as well as the average over all spins in the system (A_a).

7.1.1 Simulation details

We simulate systems of $N = 8L^2M$ spins, where the unit cell has 8 spins (as in Fig. 3.2) and we have $L \times L \times M$ unit cells in the hexagonal lattice system with periodic boundary conditions. We assume the same spin length on the kagome and triangular lattice sites. Also, we work with the classical equations of motion, valid for spin $S \gg 1$. The classical spin configurations are specified by the unit vectors $\{\boldsymbol{n}_i\}$.

The simulated annealing step uses Metropolis Monte Carlo moves for classical Heisenberg spins. Our cooling schedule involves progressively lowering the temperature by a factor of $1/e$ each time, and scaling the step-size of each Metropolis move by $\sqrt{T}$ so that the acceptance ratio stays close to 50%. Each spin is flipped on the order of 10^3 to 10^4 times at each temperature step. The Hamiltonian we use for Monte Carlo is

$$\mathcal{H} = \tfrac{1}{2}\sum_{i,j}(J_{ij}S^2)\boldsymbol{n}_i \cdot \boldsymbol{n}_j + K(J_1S^2)|\boldsymbol{M}_{tot}|^2 \ , \tag{7.4}$$

which has an added term with $K > 0$ to suppress the total magnetisation. In Section 7.1.2,

we discuss the use of such a term to reduce the precessional effect caused by the total magnetisation $\boldsymbol{M}_{tot} \equiv \sum_i \boldsymbol{n}_i$.

We numerically integrate Eq. (7.2) for each initial spin configuration using a fourth order Runge-Kutta algorithm with adaptive stepsize control of the error (Dormand-Prince method), which is implemented in MATLAB as `ode45`. The integration time t is measured in units of $(J_1 S/\hbar)^{-1}$. We limit the number of integration time-points to control the demands on computing time and memory.

The computational time required for the simulated annealing step scales linearly with system size. We are able to obtain reasonably fast runtimes using MATLAB on an Apple MacPro desktop. For a system of 8,000 spins ($10 \times 10 \times 10$ unit cells), the simulation for a single spin configuration is completed within 38 hours (37 hours for Monte Carlo, 1 hour for molecular dynamics).

As Eq. (7.2) conserves total energy and total spin, these two quantities provide a check on the accuracy of the numerical integration. Moessner and Chalker[14] report relative errors to within 10^{-8}, while Conlon and Chalker[62] report relative errors to within 10^{-6}. For our current MD implementation in MATLAB, we are limited to a maximum integration time on the order of $10^4 \cdot (J_1 S/\hbar)^{-1}$, due to the upward creep of the system energy by about 0.5%.

7.1.2 Precession about the total magnetisation

In small systems, we find an oscillatory contribution to the spin autocorrelation function, with a frequency that varies with the initial configuration. We attribute this behaviour to precession of the spin configuration about the total magnetisation, which we explain in this subsection. Since such oscillations obscure other features in the long-time behaviour, and the effect is anyway suppressed in large systems (since the magnetisation *per spin* falls with increasing system size even though the total magnetisation grows), we introduce an additional term in the Monte Carlo Hamiltonian Eq. (7.4) to suppress the total magnetisation, which reduces the influence of this oscillatory effect.

We can do a simple estimate of the oscillation frequency due to the total magnetisation.

For $J_1 = J_2$, the total magnetisation results in a static local field of magnitude

$$M_{avg} = \frac{6}{N}|\boldsymbol{M}_{tot}| \tag{7.5}$$

at each site, since each site has six nearest neighbours and the total magnetisation is distributed across all N sites on average. From Eq. (7.2), the angular frequency due to precession about this static field is $f = M_{avg}$, which decays with increasing system size for disordered spin configurations. For a system of 1,960 spins ($7 \times 7 \times 5$ unit cells), the observed oscillation frequencies agree roughly with this estimate, being about 30–40% higher than expected from precession about M_{avg} in Eq. (7.5). In Fig. 7.1, we show simulations of the spin autocorrelation for $K = 0$ in Eq. (7.4), i.e., without an additional term to suppress the total magnetisation. For these simulations, we set $\alpha = J_2/J_1 = 1$ and $k_B T/J_1 S^2 = 10^{-3}$, and the runs are labelled by the value of $|\boldsymbol{M}_{tot}|$.

To determine an appropriate coefficient K in Eq. (7.4) for suppressing the total magnetisation, we ran a series of similar simulations with $K \in \{1, 10\}$. The autocorrelation is averaged over four runs, for each value of K (see Fig. 7.2). As the curves for $K = 1$ and $K = 10$ are not too different, the results we show subsequently are based on putting $K = 1$ in the Monte Carlo Hamiltonian Eq. (7.4). Furthermore, the values of $|\boldsymbol{M}_{tot}|$ for runs with $K = 1$ (see Fig. 7.3) give estimated oscillation periods using Eq. (7.5) that are several times longer than the integration time shown, so we can neglect the residual precessional effects.

7.1.3 System size effects

We can be confident that our results are applicable in the thermodynamic limit if there is convergence for a wide range of system sizes. In Fig. 7.4, we show the results of our MD simulations for different system sizes, each averaged over two runs. There is good qualitative agreement between the results for the 8,000 spin and 4,096 spin systems (for about half the integration time), and a clear difference with the 1,960 spin system.

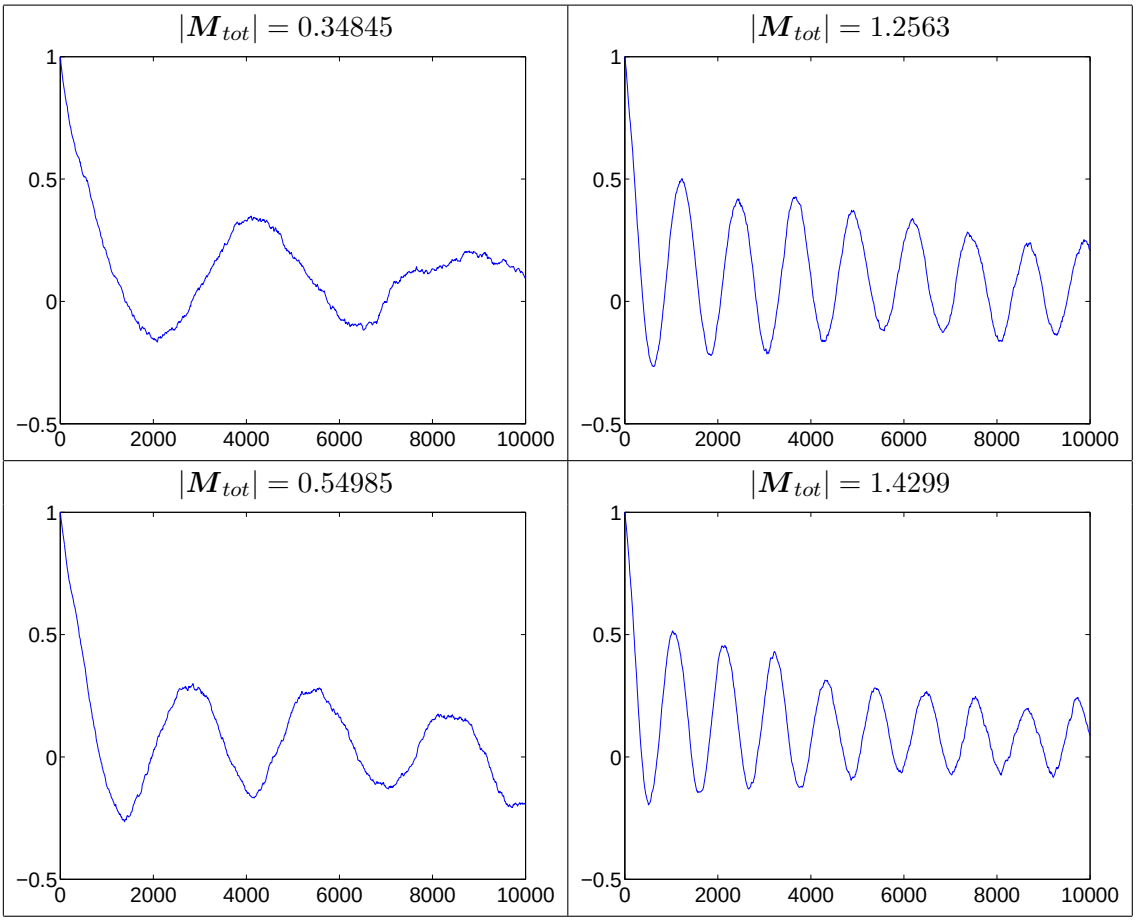


Figure 7.1: Spin autocorrelation $A_a(t)$ averaged over all sites, as a function of integration time that is in units of $(J_1 S/\hbar)^{-1}$. Results are shown for each of four independent simulated annealing runs with $K = 0$ in Eq. (7.4). There are 1,960 spins ($7 \times 7 \times 5$ unit cells), with $\alpha = J_2/J_1 = 1$ and $k_B T/J_1 S^2 = 10^{-3}$.

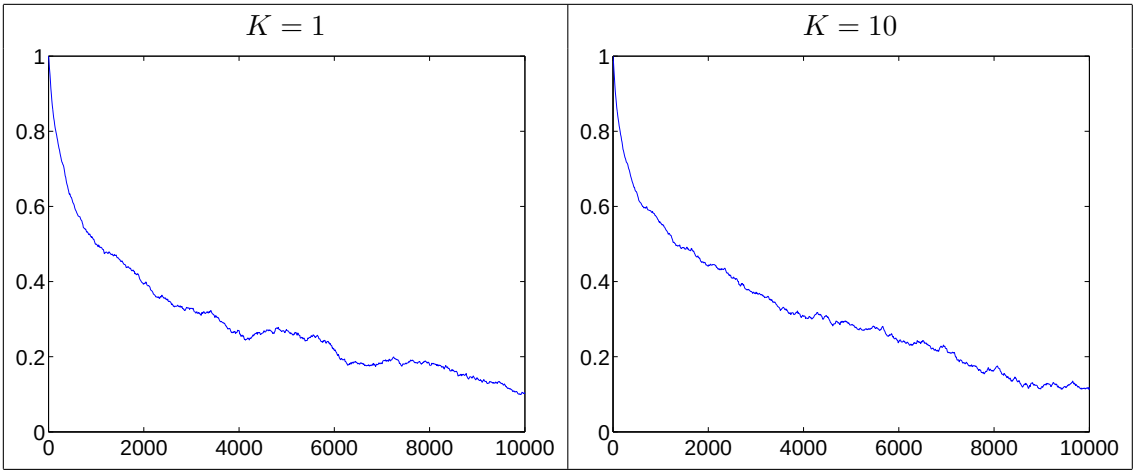


Figure 7.2: Spin autocorrelation $A_a(t)$ averaged over all sites, as a function of integration time that is in units of $(J_1 S/\hbar)^{-1}$. Results are shown for the average of four independent simulated annealing runs with $K \in \{1, 10\}$ in Eq. (7.4). There are 1,960 spins ($7 \times 7 \times 5$ unit cells), with $\alpha = J_2/J_1 = 1$ and $k_B T/J_1 S^2 = 10^{-3}$.

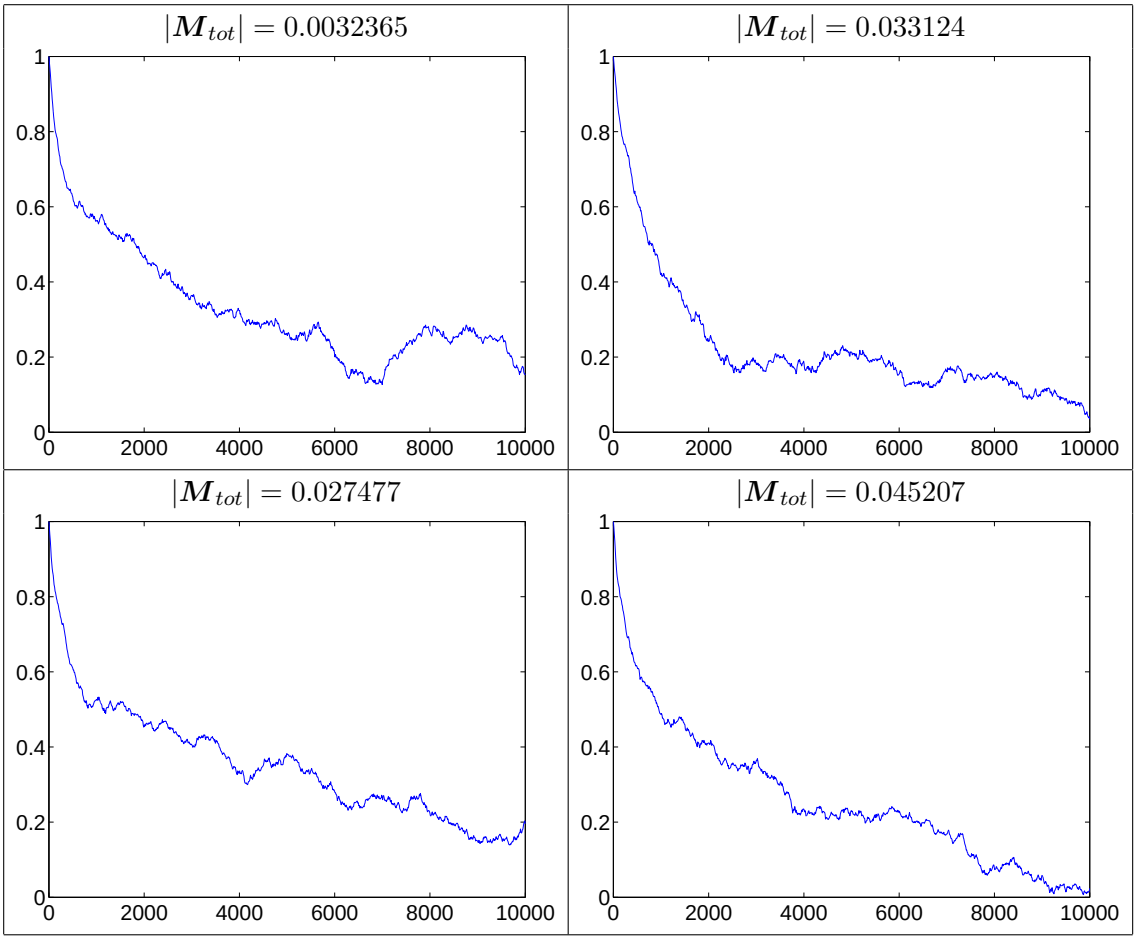


Figure 7.3: Spin autocorrelation $A_a(t)$ averaged over all sites, as a function of integration time that is in units of $(J_1 S/\hbar)^{-1}$. Results are shown for each of four independent simulated annealing runs with $K = 1$ in Eq. (7.4). There are 1,960 spins ($7 \times 7 \times 5$ unit cells), with $\alpha = J_2/J_1 = 1$ and $k_B T/J_1 S^2 = 10^{-3}$.

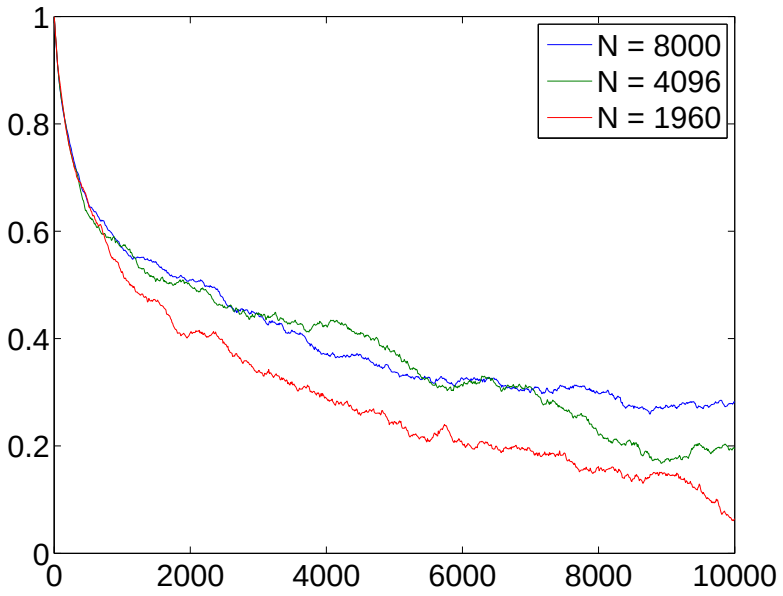


Figure 7.4: Spin autocorrelation $A_a(t)$ averaged over all sites, as a function of integration time that is in units of $(J_1 S/\hbar)^{-1}$. Results are shown for the average of two independent simulated annealing runs, for system sizes ranging from 1,960 spins ($7\times7\times5$ unit cells) to 4,096 spins ($8\times8\times8$ unit cells) to 8,000 spins ($10\times10\times10$ unit cells). We set $K=1$ in Eq. (7.4), with $\alpha = J_2/J_1 = 1$ and $k_B T/J_1 S^2 = 10^{-3}$.

7.2 Results for spin autocorrelation

As we shall see in this section, the most puzzling aspect of our results for the spin autocorrelation on the extended kagome lattice is that the dynamics of the kagome layer spins shows the *same temperature scaling* of the relaxation time as for the pyrochlore lattice. In Section 7.2.1, we compare the results of MD simulations with linear spinwave theory. In Section 7.2.2, we look at the behaviour on longer timescales to discuss our expectation of slow dynamics due to the strong interlayer correlation.

7.2.1 Comparison with linear spinwave theory

Using linear spinwave theory, we obtained Eq. (5.36) for the spin autocorrelation function. In this spinwave (SW) approximation, the decay of the spin autocorrelation is proportional to the temperature. Comparing the spin autocorrelation at short times obtained from SW and MD provides a powerful cross-check of both techniques, especially since there are no fitting parameters. The same thermal spin configuration obtained from simulated annealing is used as the initial configuration for both the MD numerical integration and the repeated alignment of spins with their local field (as described in Section 5.2.1) to get

a numerical SW ground state.

In Fig. 7.5, the SW and MD results for the spin autocorrelation are plotted together. We see that the agreement in the initial slopes is extremely good, giving a strong indication of the reliability of both techniques, at least at short times. As expected, the differences between the curves (note the differences in the vertical scales) are smaller for lower temperatures, as the dynamics become slower. We also notice that the *kagome spins relax faster* than the triangular lattice spins under both SW and MD, which is an interesting finding that we will discuss further in Section 7.2.2.

7.2.2 Dynamics on long timescales

The strong interlayer correlation for the extended kagome lattice leads us to expect slower dynamics than for the pyrochlore lattice. We saw in Chapter 6 that the stochastic SCGA for stacked kagome layers supported this expectation of slower dynamics, with a T^{-2} scaling of the relaxation time with temperature. However, our MD simulations surprisingly show that the relaxation of the kagome layer spins has the relatively fast T^{-1} scaling with temperature that is seen for both the pyrochlore and kagome lattices. As we see in Fig. 7.6, the triangular lattice spins relax more slowly than the kagome lattice spins. In this subsection, we will focus on our results for the relaxation of the kagome layer spins. We discuss possible explanation for the observed fast dynamics of kagome spins.

To study the relaxation of the kagome layer spins, we ran MD simulations at different temperatures for $\alpha = J_2/J_1 = \frac{1}{2}$, as the spins are less collinear for smaller α. For this particular value of α, the sum rule Eq. (2.12) assures us also that the classical ground states have zero net magnetisation in each unit cell, further reducing the precessional effects discussed in Section 7.1.2. The T^{-1} scaling of the relaxation time for the kagome layer spins is clearly observed in Fig. 7.7, very closely matching the similar behaviour of the pyrochlore lattice reported by Moessner and Chalker (shown in Fig. 7.8).

Maxwell counting for the pyrochlore lattice gives an extensive ground state dimension.[53] For the extended kagome lattice, the ground state dimension is divergent but sub-extensive, as we saw in Section 3.1.2. We can imagine two possible explanations for our finding that the kagome layer spins in the extended kagome lattice relax as quickly as the spins in the pyrochlore lattice. One is that for the finite-size systems with periodic boundary conditions

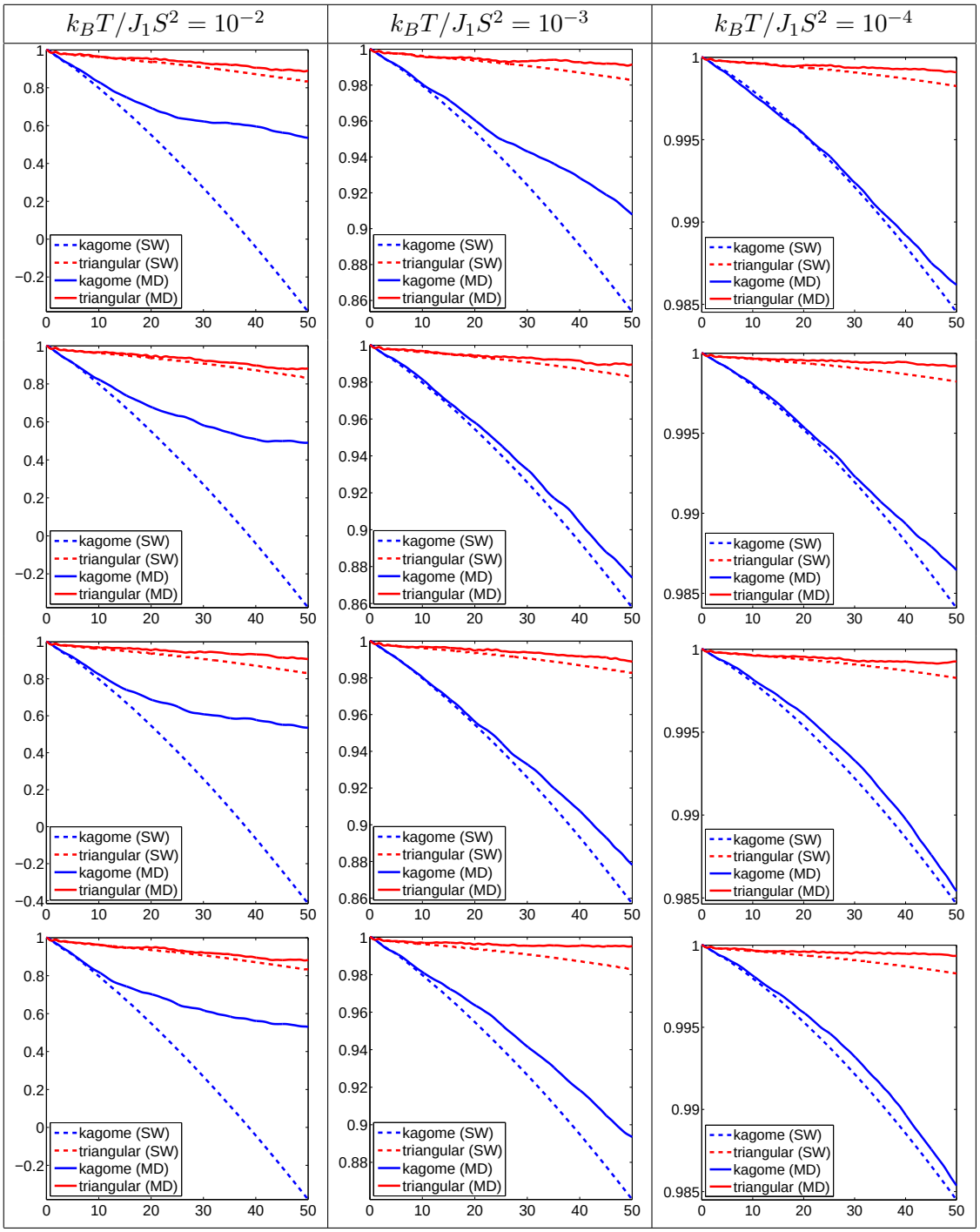


Figure 7.5: Spin autocorrelation $A_k(t)$ and $A_t(t)$ averaged over kagome and triangular lattice sites respectively, as a function of integration time that is in units of $(J_1 S/\hbar)^{-1}$. The spinwave (SW) and molecular dynamics (MD) simulations are described in the text (Section 7.2.1). Results are shown for four independent simulated annealing runs at each temperature T, for a system of 1,960 spins ($7 \times 7 \times 5$ unit cells) for the left and middle column, and a different system geometry of $6 \times 6 \times 6$ unit cells (1,728 spins) for the right column. We set $K = 1$ in Eq. (7.4), with $\alpha = J_2/J_1 = 1$.

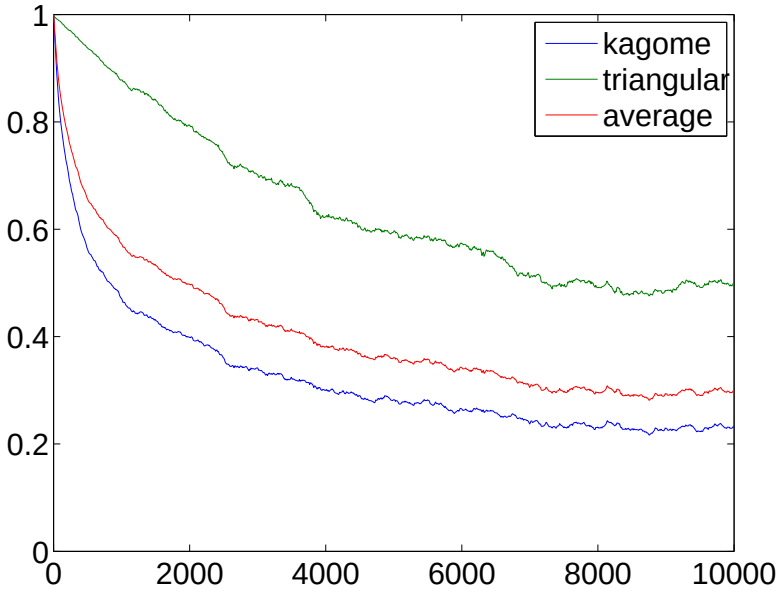


Figure 7.6: Spin autocorrelation function on long timescales, averaged over all sites, and separately over the kagome and triangular lattice sites. $\{A_a(t), A_k(t), A_t(t)\}$ are plotted as a function of integration time, which is in units of $(J_1 S/\hbar)^{-1}$. Results are shown for the average of three independent simulated annealing runs, for a system of 8,000 spins ($10 \times 10 \times 10$ unit cells). We set $K = 1$ in Eq. (7.4), with $\alpha = J_2/J_1 = 1$ and $k_B T/J_1 S^2 = 10^{-3}$.

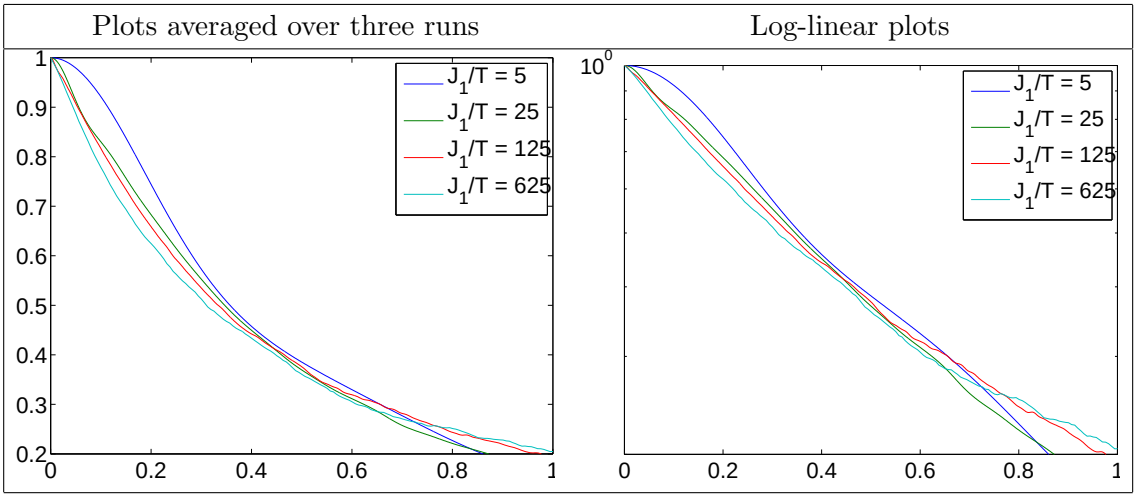


Figure 7.7: Spin autocorrelation $A_k(t)$ averaged over kagome layer sites, as a function of rescaled integration time Tt, measured in units of $\hbar S/k_B$. Results are shown for the average of three independent simulated annealing runs, for a system of 8,000 spins ($10 \times 10 \times 10$ unit cells). We set $K = 1$ in Eq. (7.4), with $\alpha = J_2/J_1 = \frac{1}{2}$ and $J_1 S^2/k_B T \in \{5, 25, 125, 625\}$.

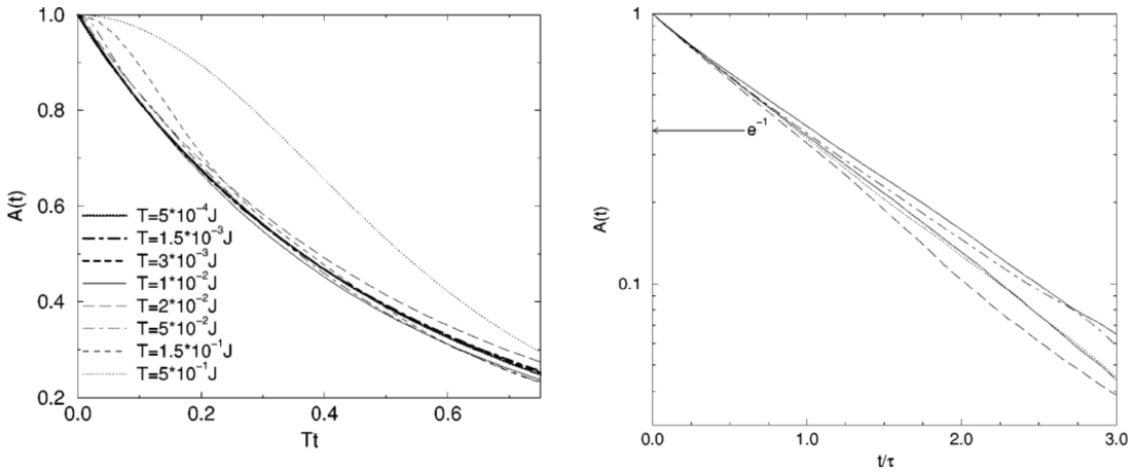


Figure 7.8: Spin autocorrelation for the pyrochlore lattice, as a function of rescaled integration time Tt. The right figure shows the decay of the autocorrelation function on a logarithmic scale for different runs at the same temperature, with time measured relative to the decay time-constant τ. Taken from Ref. [14].

that we simulate, the correction Eq. (3.9) to the ground state dimension is significant, such that the number of zero modes per spin is not too different from the pyrochlore case. The other is that the energy barriers between different kagome spin configurations, keeping the triangular layer spins fixed, are small enough that the spins can cross them even at the low temperatures studied. In the former scenario, we expect the dynamics of the kagome layer spins to slow down in the thermodynamic limit, as the number of zero modes per spin goes to zero. We do not expect such a slowing down with larger system sizes in the latter scenario.

It will take more work to distinguish between these possibilities. One useful indication concerning the excitation of very soft modes at low temperatures for the latter scenario is the density of states at low energy. The spectrum of stiffnesses for numerical ground states discussed in Section 5.2.2 essentially gives the integrated density of states (see Fig. 7.9).

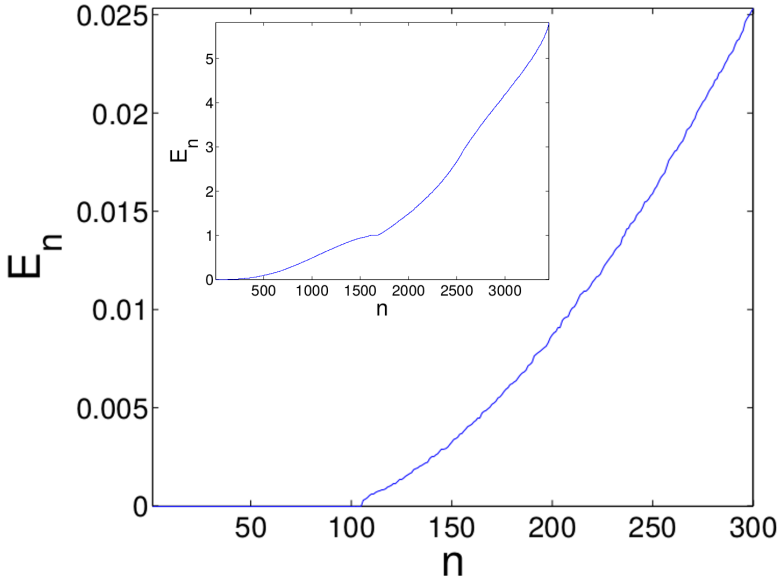


Figure 7.9: Integrated density of states from the smaller eigenvalues E_n (sorted in ascending order) of the energy matrix $\mathcal{M}$ in Eq. (5.18) for a numerical ground state of a system with 1,728 spins ($6 \times 6 \times 6$ unit cells). We set $\alpha = J_2/J_1 = \frac{1}{2}$. *(Inset):* The same plot for all 3,456 eigenvalues.

CHAPTER 8

Concluding remarks

> What can a pencil do for all of us? Amazing things. It can write transcendent poetry, uplifting music, or life-changing equations; it can sketch the future, give life to untold beauty, and communicate the full force of our love and aspirations.
>
> — *Adam Braun*

Our work has focused on the nearest-neighbour Heisenberg antiferromagnet on the extended kagome lattice, which appears to be a reasonable theoretical model for magnetism in some '114' cobaltites and ferrites. One motivation to study this particular system is the availability of single-crystal inelastic neutron scattering data. The techniques we use for characterising the spin excitations might also be useful for studying other geometrically frustrated magnets. There is also strong interest in the *novel geometry* of the extended kagome lattice, which, for classical spins, imposes strong interlayer correlations between the triangular lattice spins at low temperatures, without similar in-plane correlations. Studying the implications of this behaviour by contrast with classical spins on other lattices, such as the pyrochlore and kagome, will further our understanding of classical frustrated magnets. Correspondingly, parts of the work are experimentally focused, while other parts are of a more theoretical nature. In this concluding chapter, we summarise our present understanding of the static and dynamic properties of the spin system before sketching out interesting directions for future work.

8.1 Summary of main findings

The experimentally focused part of our work aims at calculating static and dynamic structure factors that can be compared against scattering experiments. This work is composed of two strands. First, we treated spin correlations in Section 4.1 using the self-consistent Gaussian approximation (SCGA), and found that the calculated static

structure factor provides a reasonable match with experimental data from elastic neutron scattering. This approach was originally planned as the starting point for studying the low temperature dynamics, but was found unsuitable due to the unphysical phase transition predicted. Second, we used linear spinwave theory to calculate the dynamic structure factor in Chapter 5, which we compared against unpublished data from inelastic neutron scattering. The similarities between the experimental and numerical data, over a wide range of wavevector and frequency, indicate that the Heisenberg model is a good starting point for describing the magnetic system.

On the more theoretical side, we have put most of our efforts into studying the classical ground states and classical spin dynamics of the system. The flux picture in Section 3.1.1 represents our attempt to find a description of classical ground states that allows us to deduce non-trivial properties of ground states. Using this description of a single layer, we show that the sum of triangular lattice spins within a given area is bounded by the perimeter of that area. Numerically, we also established in Section 3.1.5 that in the numerical ground states we generate, neither the kagome nor the triangular lattice spins are coplanar. We also find that unlike the triangular lattice spins that are strongly correlated between layers, the kagome lattice spins quickly decorrelate in the interlayer direction.

We also studied the dimension and connectedness of the classical ground state manifold. The ground state dimension was estimated based on the Maxwell counting argument presented in Section 3.1.2, which predicts a divergent but sub-extensive number of continuous degrees of freedom in the ground state manifold. We verified the accuracy of this counting argument in Section 5.2.2 by counting the number of zero modes for the energy matrix of numerical ground states. We are much less conclusive on the question of whether the ground state manifold is connected. We attempted to shed some light on the possibilities by using simulations of small spin clusters in Section 3.1.3 to look for additional constraints on the triangular lattice spin configurations that might indicate possible energy barriers. We also sketch out a possible topological argument for disconnectedness in Section 3.1.4, but are unable to show that more than one topological sector lies within the ground state manifold. The plausible but unproven picture is of a disconnected ground state manifold, especially if the interlayer coupling J_2 between kagome and triangular lattice spins is large compared to the in-plane coupling J_1 between kagome spins.

We expect the spin dynamics of the system to display a drastic slowing down at low temperatures due to the strong interlayer correlations. The theoretical approach we used to model the spin dynamics was the stochastic SCGA developed recently for the pyrochlore lattice. As the SCGA for the extended kagome lattice predicts an ordering transition, we considered instead a geometry of stacked kagome layers interacting antiferromagnetically within layers and ferromagnetically between layers. Use of this alternative geometry to approximate the extended kagome lattice was motivated by the form of the effective interaction between kagome spins obtained after integrating out the triangular lattice spins exactly, as we discussed in Section 4.2. In Chapter 6, we showed that the stochastic SCGA for the stacked kagome layers gives a relaxation rate for the spin autocorrelation that scales with temperature as $\Gamma \sim T^2$, which is much slower than the $\Gamma \sim T$ scaling for the pyrochlore lattice.

In Chapter 7, we tested our ideas about the spin dynamics using molecular dynamics (MD) simulations. We compared these simulations with results from linear spinwave theory that we developed for the detailed comparison with inelastic scattering, and found excellent agreement at short times. We found numerically from both techniques that the kagome spins in the lattice relax faster than the triangular lattice spins. Surprisingly, the MD results showed that the relaxation of the kagome lattice spins was essentially the same as for the pyrochlore lattice, and more work needs to be done to decide why this happens.

8.2 Directions for future work

We have some clear and promising directions for future work. These can be organised into four major threads, as we will outline below.

For the comparison between linear spinwave theory and inelastic neutron scattering, in collaboration with T. G. Perring and R. I. Bewley, we intend to do a comprehensive test of the goodness of fit over the whole sampled four-dimensional volume of wavevector and frequency. This will help determine the optimal parameters for our spin model and highlight where the largest discrepencies appear.

For the classical ground state manifold, we want to push harder on whether this manifold is provably disconnected, for at least one example in some parameter regime. We might be

able to do this by first integrating out the kagome lattice spins to get ferromagnetic chains of triangular lattice spins, with some effective interchain coupling. We can then take the zero-temperature limit, where this effective coupling should remain finite. The form of this coupling should then guide us on the issue of ground state connectedness.

For the predicted slow spin dynamics at low temperatures, there are two things we want to try. First, we want to improve the statistics for the current MD simulations and better characterise the relaxation of the triangular lattice spins, and compare this against the stochastic SCGA prediction. Second, we want to see if the results of MD simulations for the stacked kagome layers matches with the prediction under the stochastic SCGA. It might be that the stacked kagome geometry is quite different from the extended kagome geometry, where the columns of triangular lattice spins in the latter act as "pivots" for the low energy movement of kagome spins, while there are only stiff chains of spins in the stacked kagome system.

For the finding that the kagome lattice spins relax with the same T^{-1} temperature scaling of the relaxation time as the pyrochlore lattice, we want to check the robustness of this behaviour in the thermodynamic limit by studying larger systems with fewer zero modes per spin. If this behaviour is robust, it indicates that the energy barriers between kagome spin configurations are so low that they can be crossed while keeping the triangular lattice spins fixed.

Bibliography

[1] W. Krauth, *Statistical Mechanics: Algorithms and Computations* (Oxford University Press, Oxford, 2006). [pp. 3, 39]

[2] R. B. Laughlin, *Nobel Lecture: Fractional quantization*, Rev. Mod. Phys. **71**, 863 (1999). [p. 3]

[3] C. Castelnovo, R. Moessner, and S. L. Sondhi, *Magnetic monopoles in spin ice*, Nature **451**, 42 (2008). [p. 3]

[4] N. D. Mermin, *The topological theory of defects in ordered media*, Rev. Mod. Phys. **51**, 591 (1979). [pp. 5, 46]

[5] H. E. Stanley, *Spherical model as the limit of infinite spin dimensionality*, Phys. Rev. **176**, 718 (1968). [pp. 7, 52]

[6] N. Ashcroft and N. Mermin, *Solid State Physics* (Brooks/Cole, Cengage Learning, 1976). [p. 7]

[7] L. Balents, *Spin liquids in frustrated magnets*, Nature **464**, 199 (2010). [p. 10]

[8] S. V. Isakov, K. Gregor, R. Moessner, and S. L. Sondhi, *Dipolar spin correlations in classical pyrochlore magnets*, Phys. Rev. Lett. **93**, 167204 (2004). [pp. 10, 52]

[9] P. W. Anderson, *The resonating valence bond state in* La_2CuO_4 *and superconductivity*, Science **235**, 1196 (1987). [p. 10]

[10] J. T. Chalker, in *Introduction to Frustrated Magnetism*, Vol. 164 of *Springer Series in Solid-State Sciences*, edited by C. Lacroix, P. Mendels, and F. Mila (Springer-Verlag, Berlin Heidelberg, 2011), Chap. 1. [pp. 11, 13, 14]

[11] A. P. Ramirez, *Strongly geometrically frustrated magnets*, Annual Review of Materials Science **24**, 453 (1994). [p. 12]

[12] Villain, J., Bidaux, R., Carton, J.-P., and Conte, R., *Order as an effect of disorder*, J. Phys. France **41**, 1263 (1980). [p. 12]

[13] R. Moessner and J. T. Chalker, *Properties of a classical spin liquid: the Heisenberg pyrochlore antiferromagnet*, Phys. Rev. Lett. **80**, 2929 (1998). [pp. 12, 14, 37, 104, 105, 106]

[14] R. Moessner and J. T. Chalker, *Low-temperature properties of classical geometrically frustrated antiferromagnets*, Phys. Rev. B **58**, 12049 (1998). [pp. 12, 14, 15, 37, 104, 105, 106, 107, 115]

[15] J. T. Chalker, P. C. W. Holdsworth, and E. F. Shender, *Hidden order in a frustrated system: Properties of the Heisenberg Kagomé antiferromagnet*, Phys. Rev. Lett. **68**, 855 (1992). [pp. 14, 37]

[16] I. Ritchey, P. Chandra, and P. Coleman, *Spin folding in the two-dimensional Heisenberg kagomé antiferromagnet*, Phys. Rev. B **47**, 15342 (1993). [pp. 14, 37]

[17] M. Valldor and M. Andersson, *The structure of the new compound* $YBaCo_4O_7$ *with a magnetic feature*, Solid State Sciences **4**, 923 (2002). [pp. 15, 17, 23, 63]

[18] L. Pauling, H. P. Klug, and A. N. Winchell, *The crystal structure of swedenborgite*, American Mineralogist **20**, 429 (1935). [p. 17]

[19] L. C. Chapon, P. G. Radaelli, H. Zheng, and J. F. Mitchell, *Competing magnetic interactions in the extended Kagomé system* $YBaCo_4O_7$, Phys. Rev. B **74**, 172401 (2006). [pp. 17, 18, 21, 22, 62]

[20] P. Manuel, L. C. Chapon, P. G. Radaelli, H. Zheng, and J. F. Mitchell, *Magnetic correlations in the extended kagome* $YBaCo_4O_7$ *probed by single-crystal neutron scattering*, Phys. Rev. Lett. **103**, 037202 (2009). [pp. 17, 18, 20, 24, 26, 29, 30, 46, 62]

[21] S. Avci, O. Chmaissem, H. Zheng, A. Huq, P. Manuel, and J. F. Mitchell, *Oxygen stoichiometry in the geometrically frustrated kagomé system* $YBaCo_4O_{7+\delta}$*: impact on phase behavior and magnetism*, Chemistry of Materials **25**, 4188 (2013). [pp. 18, 21]

[22] M. Valldor, *Syntheses and structures of compounds with* $YBaCo_4O_7$*-type structure*, Solid State Sciences **6**, 251 (2004). [pp. 18, 23]

[23] M. Soda, Y. Yasui, T. Moyoshi, M. Sato, N. Igawa, and K. Kakurai, *Magnetic structure of* $YBaCo_4O_7$ *with kagome and triangular lattices*, Journal of the Physical Society of Japan **75**, 054707 (2006). [p. 18]

[24] A. Huq *et al.*, *Structural and magnetic properties of the Kagomé antiferromagnet* $YbBaCo_4O_7$, Journal of Solid State Chemistry **179**, 1136 (2006). [pp. 20, 23]

[25] W. Schweika, M. Valldor, and P. Lemmens, *Approaching the ground state of the kagomé antiferromagnet*, Phys. Rev. Lett. **98**, 067201 (2007). [p. 30]

[26] D. D. Khalyavin, L. C. Chapon, P. G. Radaelli, H. Zheng, and J. F. Mitchell, *Structural behavior of the kagome antiferromagnet* $TmBaCo_4O_7$*: Neutron diffraction study and group-theoretical consideration*, Phys. Rev. B **80**, 144107 (2009). [p. 20]

[27] D. D. Khalyavin *et al.*, *Spin-ordering and magnetoelastic coupling in the extended kagome system* $YBaCo_4O_7$, Phys. Rev. B **83**, 094412 (2011). [pp. 21, 22, 26]

[28] J. R. Stewart, G. Ehlers, H. Mutka, P. Fouquet, C. Payen, and R. Lortz, *Spin dynamics, short-range order, and spin freezing in* $Y_{0.5}Ca_{0.5}BaCo_4O_7$, Phys. Rev. B **83**, 024405 (2011). [pp. 30, 31]

[29] S. Avci *et al.*, *Kinetic control of structural and magnetic states in* $LuBaCo_4O_7$, Phys. Rev. B **85**, 094414 (2012).

[30] M. J. R. Hoch *et al.*, *Evidence for an internal-field-induced spin-flop configuration in the extended kagome* $YBaCo_4O_7$, Phys. Rev. B **87**, 064419 (2013).

[31] G. Bychkov *et al.*, *Primary crystallization fields, growth features and properties of rare earth and barium-based cobaltates*, Journal of Crystal Growth **275**, e813 (2005), proceedings of the 14th International Conference on Crystal Growth and the 12th International Conference on Vapor Growth and Epitaxy.

[32] A. N. Bludov *et al.*, *A magnetic-field-induced irreversible transition in geometrically frustrated antiferromagnetic* $TbBaCo_4O_7$ *with kagome and triangular lattices*, Low Temperature Physics **35**, 971 (2009).

[33] R. Szymczak, A. N. Bludov, S. L. Gnatchenko, S. N. Barilo, A. Jezierski, and H. Szymczak, *Field-induced magnetic order in frustrated* $TbBaCo_4O_7$ *single crystals*, Acta Physica Polonica A **118**, 299 (2010), 14th National School on Superconductivity and Inhomogeneous Condensed Systems, Ostrow, Poland, Oct 13–17, 2009. [p. 18]

[34] M. Valldor, *Remnant magnetization above room temperature in the semiconductor* $Y_{0.5}Ca_{0.5}BaCo_4O_7$, Solid State Sciences **8**, 1272 (2006). [p. 18]

[35] V. Pralong, V. Caignaert, A. Maignan, and B. Raveau, *Structure and magnetic properties of* $LnBaFe_4O_7$ *oxides: Ln size effect*, J. Mater. Chem. **19**, 8335 (2009). [p. 19]

[36] V. Caignaert *et al.*, *A new mixed-valence ferrite with a cubic structure,* $YBaFe_4O_7$*: spin-glass-like behavior*, Chemistry of Materials **21**, 1116 (2009). [p. 19]

[37] M. Valldor, Y. Sanders, and W. Schweika, *High spin frustration in Co based Swedenborgites*, Journal of Physics: Conference Series **145**, 012076 (2009). [p. 19]

[38] M. Valldor, R. P. Hermann, J. Wuttke, M. Zamponi, and W. Schweika, *Spin correlations in the extended kagome system $YBaCo_3FeO_7$*, Phys. Rev. B **84**, 224426 (2011). [pp. 19, 24, 30, 31]

[39] N. Hollmann *et al.*, *Electronic and magnetic properties of the kagome systems $YBaCo_4O_7$ and $YBaCo_3MO_7$ ($M = Al,\ Fe$)*, Phys. Rev. B **80**, 085111 (2009). [pp. 19, 21, 25]

[40] D. D. Khalyavin, P. Manuel, and L. C. Chapon, *Possible chiral spin-liquid phase in noncentrosymmetric $RBaCo_4O_7$*, Phys. Rev. B **85**, 220401 (2012). [p. 19]

[41] B. Raveau, V. Caignaert, V. Pralong, D. Pelloquin, and A. Maignan, *A Series of Novel Mixed Valent Ferrimagnetic Oxides with a T_C up to 270 K: $Ca_{1-x}Y_xBaFe_4O_7$*, Chemistry of Materials **20**, 6295 (2008). [p. 20]

[42] T. Sarkar, V. Duffort, V. Pralong, V. Caignaert, and B. Raveau, *Oxygen hyperstoichiometric hexagonal ferrite $CaBaFe_4O_{7+\delta}$ ($\delta \approx 0.14$): Coexistence of ferrimagnetism and spin glass behavior*, Phys. Rev. B **83**, 094409 (2011). [p. 20]

[43] V. Caignaert, V. Pralong, A. Maignan, and B. Raveau, *Orthorhombic kagome cobaltite $CaBaCo_4O_7$: A new ferrimagnet with a T_C of 70 K*, Solid State Communications **149**, 453 (2009). [p. 20]

[44] V. Caignaert, V. Pralong, V. Hardy, C. Ritter, and B. Raveau, *Magnetic structure of $CaBaCo_4O_7$: Lifting of geometrical frustration towards ferrimagnetism*, Phys. Rev. B **81**, 094417 (2010). [p. 20]

[45] M.-H. Whangbo, H.-J. Koo, and D. Dai, *Spin exchange interactions and magnetic structures of extended magnetic solids with localized spins: theoretical descriptions on formal, quantitative and qualitative levels*, Journal of Solid State Chemistry **176**, 417 (2003), special issue on The Impact of Theoretical Methods on Solid-State Chemistry. [p. 20]

[46] M.-H. Whangbo, D. Dai, and H.-J. Koo, *Spin dimer, electronic band structure and classical spin analyses of spin exchange interactions and ordered magnetic structures of magnetic solids*, Solid State Sciences **7**, 827 (2005), selected articles from the 4th International Conference on Inorganic Materials Antwerp, Belgium 19-21 September 2004. [p. 20]

[47] D. D. Khalyavin, P. Manuel, J. F. Mitchell, and L. C. Chapon, *Spin correlations in the geometrically frustrated $RBaCo_4O_7$ antiferromagnets: Mean-field approach and Monte Carlo simulations*, Phys. Rev. B **82**, 094401 (2010). [pp. 20, 21, 24, 26, 28, 29]

[48] O. Parkkima, H. Yamauchi, and M. Karppinen, *Oxygen Storage Capacity and Phase Stability of Variously Substituted $YBaCo_4O_{7+\delta}$*, Chemistry of Materials **25**, 599 (2013). [p. 21]

[49] S. Yuan *et al.*, *Spin ordering and dynamics in the frustrated antiferromagnet* $YBaCo_4O_{7.1}$, Phys. Rev. B **89**, 094416 (2014). [p. 23]

[50] S. Buhrandt and L. Fritz, *Spin-liquid phase and order-by-disorder of classical Heisenberg spins on the swedenborgite lattice*, ArXiv e-prints (2014). [pp. 24, 34, 47, 49, 50]

[51] T.-H. Han *et al.*, *Fractionalized excitations in the spin-liquid state of a kagome-lattice antiferromagnet*, Nature **492**, 406 (2012). [p. 33]

[52] K. Tomiyasu *et al.*, *Emergence of Highly Degenerate Excited States in the Frustrated Magnet* $MgCr_2O_4$, Phys. Rev. Lett. **110**, 077205 (2013). [p. 33]

[53] J. N. Reimers, A. J. Berlinsky, and A.-C. Shi, *Mean-field approach to magnetic ordering in highly frustrated pyrochlores*, Phys. Rev. B **43**, 865 (1991). [pp. 36, 112]

[54] J. C. Maxwell, *L. On the calculation of the equilibrium and stiffness of frames*, Philosophical Magazine Series 4 **27**, 294 (1864). [p. 36]

[55] L. R. Walker and R. E. Walstedt, *Computer Model of Metallic Spin-Glasses*, Phys. Rev. Lett. **38**, 514 (1977). [pp. 39, 67]

[56] L. R. Walker and R. E. Walstedt, *Computer model of metallic spin-glasses*, Phys. Rev. B **22**, 3816 (1980). [pp. 39, 67]

[57] H. Kawamura and S. Miyashita, *Phase Transition of the Two-Dimensional Heisenberg Antiferromagnet on the Triangular Lattice*, Journal of the Physical Society of Japan **53**, 9 (1984). [p. 46]

[58] H. Kawamura and S. Miyashita, *Phase Transition of the Two-Dimensional Heisenberg Antiferromagnet on the Triangular Lattice*, Journal of the Physical Society of Japan **53**, 4138 (1984). [p. 46]

[59] D. A. Garanin, *Self-consistent Gaussian approximation for classical spin systems: Thermodynamics*, Phys. Rev. B **53**, 11593 (1996). [p. 51]

[60] T. H. Berlin and M. Kac, *The Spherical Model of a Ferromagnet*, Phys. Rev. **86**, 821 (1952). [p. 52]

[61] B. Canals and D. A. Garanin, *Spin-liquid phase in the pyrochlore anti-ferromagnet*, Canadian Journal of Physics **79**, 1323 (2001). [p. 52]

[62] P. H. Conlon and J. T. Chalker, *Spin Dynamics in Pyrochlore Heisenberg Antiferromagnets*, Phys. Rev. Lett. **102**, 237206 (2009). [pp. 59, 61, 65, 93, 98, 99, 105, 107]

[63] P. H. Conlon and J. T. Chalker, *Absent pinch points and emergent clusters: Further neighbor interactions in the pyrochlore Heisenberg antiferromagnet*, Phys. Rev. B **81**, 224413 (2010). [pp. 52, 59]

[64] J. Zinn-Justin, *Path Integrals in Quantum Mechanics*, *Oxford Graduate Texts* (Oxford University Press, Oxford, 2010). [p. 52]

[65] D. A. Garanin and B. Canals, *Classical spin liquid: Exact solution for the infinite-component antiferromagnetic model on the kagomé lattice*, Phys. Rev. B **59**, 443 (1999). [pp. 61, 95, 96]

[66] P. J. Brown, in *International Tables for Crystallography*, edited by E. Prince (John Wiley & Sons, Ltd., USA, 2006), Vol. C, Mathematical, physical and chemical tables, Chap. 4.4.5, pp. 454–461. [p. 62]

[67] T. Holstein and H. Primakoff, *Field Dependence of the Intrinsic Domain Magnetization of a Ferromagnet*, Phys. Rev. **58**, 1098 (1940). [p. 68]

[68] R. I. Bewley and T. G. Perring, private communication. [p. 89]

[69] H. Risken, *The Fokker-Planck Equation: Methods of Solution and Applications*, Vol. 18 of *Springer Series in Synergetics* (Springer-Verlag, Berlin Heidelberg, 1996). [p. 101]

[70] M. Chiani, D. Dardari, and M. K. Simon, *New exponential bounds and approximations for the computation of error probability in fading channels*, Wireless Communications, IEEE Transactions on **2**, 840 (2003). [p. 104]

[71] A. Keren, *Dynamical simulation of spins on kagomé and square lattices*, Phys. Rev. Lett. **72**, 3254 (1994). [p. 105]

[72] J. Robert, B. Canals, V. Simonet, and R. Ballou, *Propagation and Ghosts in the Classical Kagome Antiferromagnet*, Phys. Rev. Lett. **101**, 117207 (2008). [p. 105]

[73] M. Taillefumier, J. Robert, C. L. Henley, R. Moessner, and B. Canals, *Semi-classical spin dynamics of the antiferromagnetic Heisenberg model on the kagome lattice*, ArXiv e-prints (2014). [p. 105]